Acoustic wave absorption and mitigation by porous metamaterial structures

DISSERTATION
zur Erlangung des Grades eines Doktors
der Ingenieurwissenschaften

vorgelegt von
M.Sc. Qi-hang Liu

eingereicht bei der Naturwissenschaftlich-Technischen Fakultät
der Universität Siegen
Siegen 2024

Betreuer und erster Gutachter

Prof. Dr.-Ing. habil. Dr. h.c. mult. Chuanzeng Zhang

Universität Siegen

Zweiter Gutachter

Prof. Dr.-Ing. Peter Schmidt

Universität Siegen

Tag der mündlichen Prüfung

06. Februar 2024

Abstract

Efficient noise control is an important and crucial issue in a wide range of engineering applications. Porous materials with dispersed micro-pores are commonly used due to their high capacity to absorb acoustic wave energy and mitigate undesirable noises. This thesis aims to improve the low-frequency sound absorption performance in a broad frequency range. For this purpose, two porous metamaterial (PM) structures are proposed, namely, the slit-perforated multi-layered porous metamaterial (SMPM) structure and the novel multiscale porous metamaterial (MPM) structure. The SMPM structure consists of periodic porous matrix layers and second-type porous layers with periodically distributed slits, while the novel MPM structure consists of a porous matrix with periodically distributed meso-pores, in which a second porous layer is introduced as an interlayer between the matrix and the meso-pores. Theoretical models based on the homogenization schemes and semi-phenomenological approaches to describe the macroscopic dynamic properties of the porous materials are adopted, while numerical methods based on the transfer matrix method (TMM) and the finite element method (FEM) are applied to compute the acoustic wave absorption and mitigation characteristics of the proposed PM structures in both room-temperature and high-temperature environments. In particular, the band structures or dispersion curves especially the frequency bandgaps, and the acoustic wave absorption coefficients are analyzed and discussed in details.

The research findings and the knowledge gained in this thesis may provide a deep insight into the acoustic wave absorption and mitigation characteristics and the corresponding physical mechanisms in porous metamaterial structures, which are highly valuable for the design, optimization, realization and application of novel porous metamaterial structures.

Kurzfassung

Effiziente Lärmdämmung ist eine wichtige und entscheidende Angelegenheit in einer Vielzahl von Ingenieuranwendungen. Poröse Materialien mit verteilten Mikroporen werden aufgrund ihrer hohen Kapazität zur Absorption von Schallwellenenergie und zur Minderung unerwünschter Geräusche häufig eingesetzt. Diese Dissertation zielt darauf ab, die Schallabsorptionsleistung bei niedrigen Frequenzen in einem breiten Frequenzbereich zu verbessern. Zu diesem Zweck werden zwei poröse Metamaterialstrukturen (PM-Strukturen) vorgeschlagen, nämlich die geschlitzt-perforierte mehrschichtige poröse Metamaterialstruktur (SMPM-Struktur) und die neuartige mehrskalige poröse Metamaterialstruktur (MPM-Struktur). Die SMPM-Struktur besteht aus periodischen porösen Matrixschichten und porösen Schichten des zweiten Typs mit periodisch verteilten Schlitzen, während die neuartige MPM-Struktur aus einer porösen Matrix mit periodisch verteilten Mesoporen besteht, in die eine zweite poröse Schicht als Zwischenschicht zwischen der Matrix und den Mesoporen eingeführt wird. Theoretische Modelle, die auf den Homogenisierungsschemata und semi-phenomenologischen Ansätzen zur Beschreibung der makroskopischen dynamischen Eigenschaften der porösen Materialien basieren, werden verwendet, während numerische Methoden auf Basis der Transfer-Matrix-Methode (TMM) und der Finite-Elemente-Methode (FEM) angewendet werden, um die akustischen Wellenabsorptions- und Dämpfungseigenschaften der vorgeschlagenen PM-Strukturen sowohl bei Raumtemperatur als auch bei Hochtemperaturumgebungen zu berechnen. Insbesondere werden die Bandstrukturen oder Dispersionskurven, insbesondere die Frequenzbandlücken, sowie die Absorptionskoeffizienten für akustische Wellen im Detail analysiert und diskutiert.

Die Forschungsergebnisse und das in dieser Dissertation gewonnene Wissen können einen tiefen Einblick in die akustischen Wellenabsorptions- und Dämpfungseigenschaften sowie die entsprechenden physikalischen Mechanismen in porösen Metamaterialstrukturen bieten, was äußerst wertvoll für die Gestaltung, Optimierung, Realisierung und Anwendung neuartiger poröser Metamaterialstrukturen ist.

Acknowledgments

This thesis was completed in the course of my research activity as a research assistant and PhD candidate from 2019 to 2023 at the Chair of Structural Mechanics, Department of Civil Engineering, School of Science and Technology, University of Siegen, Germany.

I would like to express my deepest gratitude to my advisor and first appraiser, Prof. Dr.-Ing. habil. Dr. h.c. mult. Chuanzeng Zhang for his unwavering support and insightful guidance throughout my doctoral journey. His dedication to fostering my academic and personal development has been truly invaluable. I am profoundly thankful for his continuous assistance and advice over the past years.

I extend my sincere appreciation to Prof. Dr.-Ing. Peter Schmidt, the second appraiser of my thesis, for taking the time to carefully read and review my thesis in details. I ’m also thankful to Prof. Dr.-Ing. Torsten Leutbecher and Prof. Dr. rer. nat. habil. Xin Jiang as Doctoral Commission members for their time and expertise invested in this process.

I truly appreciate the help of Dr. Zhengyang Li and Dr. Xuewei Liu for the useful and meaningful suggestions and discussions regarding my research work in the past four years. I want to express my sincere thanks to the colleagues in my group for their kind help, care and support: Prof. Leilei Cao, Prof. Yan Gu, Dr. Yuyang Chai, Dr.-Ing. Benjamin Ankay, Dr. -Ing. Marius Mellmann, Dr.-Ing. Elias Perras, Zhenyuan Lv, Ben Wang, Cancan Liu and Peijun Zhang. I would also like to thank Meike Stricker, the secretary of my advisor, she has always been so helpful with dealing my documents. It was a bit pity that we had much less time to meet in person because of the Corona-pandemic, but I cherish and enjoy every moment when we could get together.

Finally, I would like to sincerely thank my family and my boyfriend Dr. Zhihao Qian for their love and support. Life has been completely different during the past four years due to the Corona-pandemic, and it was not easy to keep the normal pace. Thanks to their accompany and care so that I could overcome even the toughest days when I suffered from anxiety and great pressure. It is because of their support and encouragement that I have been able to successfully complete my doctoral studies.

Contents

List of abbreviations

Abbreviation	Explanation
DP	Double porosity
FEM	Finite element method
HM	Homogenization method
HPC	High permeability contrast
IBZ	Irreducible Brillouin zone
LPC	Low permeability contrast
MPP	Micro-perforated panel
MPM	Multiscale porous metamaterial
PC	Permeability contrast
PCM	Porous composite metamaterial
PM	Porous metamaterial
SMF	Sintered metallic fibre
SMPM	Slit-perforated multi-layered porous metamaterial
SPM	Slit-perforated porous metamaterial
TMM	Transfer matrix method
UC	Unit-cell

List of symbols

Latin symbols	Explanation
a	Lattice constant
a_1, a_2	Thickness of the constituents of the SPM and the PCM structure
c	Acoustic wave velocity
c_0	Acoustic wave velocity in air
$\tilde{c}_{eq}$	Equivalent acoustic wave velocity in porous materials
C_p	Specific heat capacity of air
d_i	Thickness of each porous material layer
f	Frequency
h	Thickness
j	Imaginary unit
J_i	The i-th order Bessel function of the first kind
$\mathbf{k}$	Wave vector
k, k_i	Wave number
K	Bulk modulus
$\tilde{K}_{eq}$	Equivalent dynamic bulk modulus of porous materials
l_1, l_2	Width of the porous materials of the SMPM structure
l_p	Lattice constant of the unit-cell of the novel MPM structure

l_s	Lattice constant of the unit-cell of SMPM
p	Acoustic pressure
p_{inc}, p_{ref}, p_{tr}	Incident, reflected and transmitted acoustic pressure
P_0	Ambient acoustic pressure
Pr	Prandtl number
r	Material composition ratio
$\mathbf{r}$	Position vector
r_1	Outer radius of the porous layer
r_2	Radius of the equivalent unit-cell
R	Reflection coefficient
R_p	Radius of the meso-pore
t	Temperature
T	Transmission coefficient
$\mathbf{t}_i$, $\mathbf{T}_i$, $\mathbf{T}_n$	Transfer matrix
TL	Transmission loss
$\mathbf{u}$	Displacement vector
w	Slit width
Z_0, Z_c	Characteristic impedance of air and the structure
Z_s	Surface impedance

Greek symbols	Explanation
α	Sound absorption coefficient
α_∞	Tortuosity factor
β	Hydraulic radius
γ	Specific heat ratio of air
κ	Heat conductivity of air
ϕ	Porosity
η	Dynamic viscosity of air
θ	Incidence angle
ϑ	Dilatation
ρ	Mass density
$\tilde{\rho}_{eq}$	Equivalent dynamic mass density of porous materials
σ	Static air-flow resistivity
ω	Angular frequency
ψ	Phase angle
Λ	Viscous characteristic length
Λ'	Thermal characteristic length

List of figures

Chapter 4

Chapter 5

List of tables

1. Introduction

1.1 Background and state of the art

Noise control is of utmost significance in diverse engineering disciplines, including building construction, mechanical engineering, aerospace and marine engineering, etc. [1-4] since the noises are generally bothersome and undesirable, which can also pose potential health risks to human [5,6]. Hence, it is crucial and imperative to utilize sound-absorbing materials or structures to effectively mitigate or isolate the bothersome noises. Commercially available sound-absorbing materials can generally be classified into two categories: resonant sound-absorbing materials and porous sound-absorbing materials [7]. Considering that this thesis primarily focuses on the acoustic characteristics of porous materials, a concise and compact overview on resonant sound-absorbing materials and structures is provided, while a more comprehensive review on porous materials will be presented as follows.

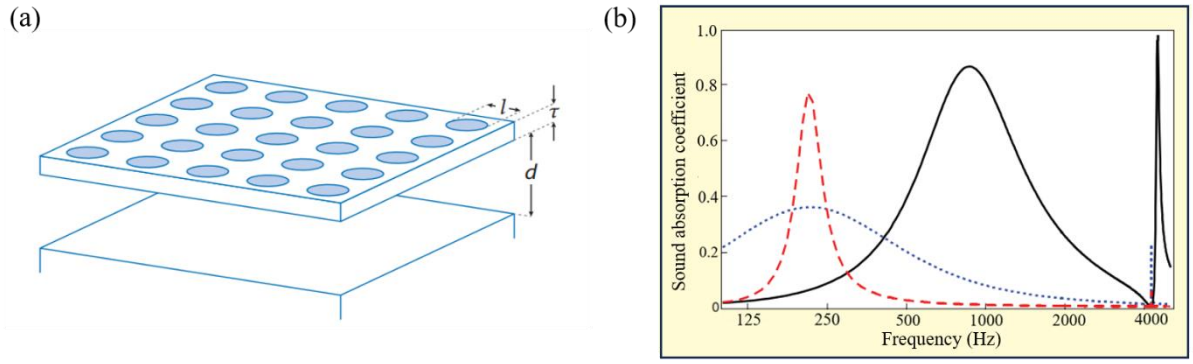

Fig. 1.1: (a) Schematic illustration for a micro-perforated panel (MPP). To facilitate visualization, the dimensions of the holes are greatly exaggerated. (b) Calculated example of the sound absorption characteristics of a MPP [8]. Solid line: $l = 0.4\text{mm}$, $\tau = 0.4\text{mm}$ Dotted line: $l = 0.4\text{mm}$, $\tau = 10\text{mm}$ Dashed line: $l = 4\text{mm}$, $\tau = 10\text{mm}$. Other parameter: Perforation ratio 1.0%, defined by the total area of the circular holes divided by the total area of the plate and $d = 0.05\text{m}$ [9,10].

Resonant sound-absorbing materials mainly involve Helmholtz resonators [11,12] and perforated panels, etc. [8,9,13]. The Helmholtz resonator is comprised of a cavity connected to a neck or tube, and operate by the principle of the internal resonance effect. When exposed to external acoustic waves at its resonant frequency, it vibrates and converts sound energy into heat which reduces the noise. Owing to this sound absorption mechanism, they often suffer from the disadvantage of effective sound absorption in specific frequency ranges which highly dependents on the geometrical details of the neck and the volume of the cavity [14,15]. The perforated panel is comprised of a thin and rigid (usually metallic) plate with straight holes or slots as perforations and is usually positioned away from a solid back as shown in Fig. 1.1(a).

A perforated panel can effectively act as an array of numerous individual Helmholtz resonators. Each resonator comprises a neck formed by the perforated panel and a shared air volume encompassing the total enclosed airspace between the panel and its back. As acoustic or sound waves penetrate the perforated panel, the friction between the moving air molecules and the internal surfaces of the perforations dissipates acoustic energy as heat [9]. The cross-sectional size of the pores in many conventional perforated panels typically falls within the millimeter range, while in 1970s, Maa discovered that by reducing the diameter of the perforations and appropriately increasing the density of the perforations, a high sound absorption across a wide frequency range could be achieved [16,17]. This led to the development of micro-perforated panels (MPP) with submillimeter pores [18-25]. However, reducing the size of the perforations beyond a certain threshold does not result in a wider absorption bandwidth and the primary practical challenge lies in manufacturing a thin panel with hundreds of submillimeter perforations per square centimeter [9]. In practice, the perforated panels have been often used as facings for porous materials to improve the low-frequency sound absorption [10,26].

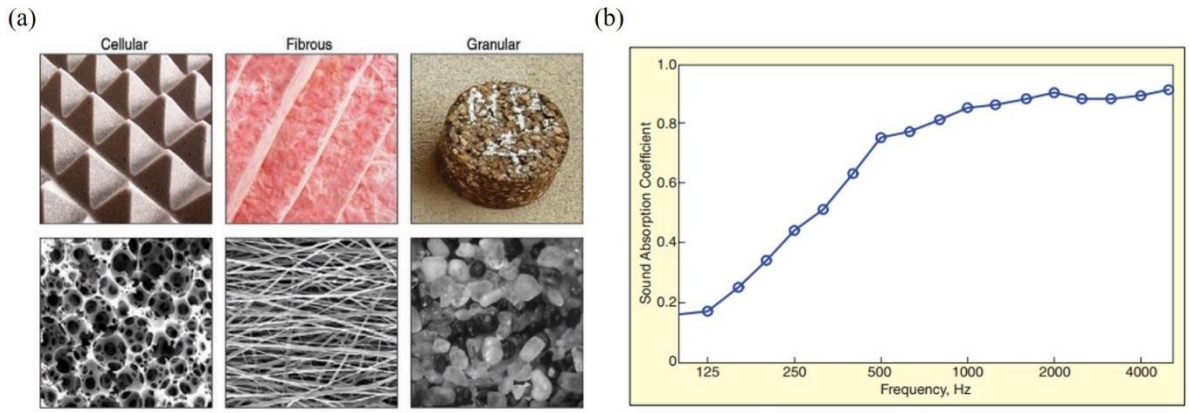

Fig. 1.2: (a) The three main types of the porous materials and their microscopic structures. (b) Measured sound absorption coefficient of a porous material made of hemp fibres [9].

Porous materials are a special kind of materials with a large number of interconnected micro-pores such as channels, cracks or cavities, and based on their microscopic configurations they can be generally classified into three types: cellular, fibrous and granular, and their typical microscopic structures are shown in Fig. 1.2(a) [9]. Open-celled polyurethane and foam materials serve as representative examples of cellular porous materials, while fibrous porous materials consist of a series of tunnel-like openings created through interstices in the material fibres. Typical examples of fibrous materials include those made of natural or synthetic fibres, such as glass and mineral fibres. Regarding granular porous materials, they are composed of relatively rigid macroscopic bodies whose dimensions exceed those of the internal voids by many orders of magnitude, which are often referred to as agglomerates [9]. Granular sound-absorbing materials involve some kinds of asphalt, porous concrete, granular clays, sands, gravel, and soils [9].

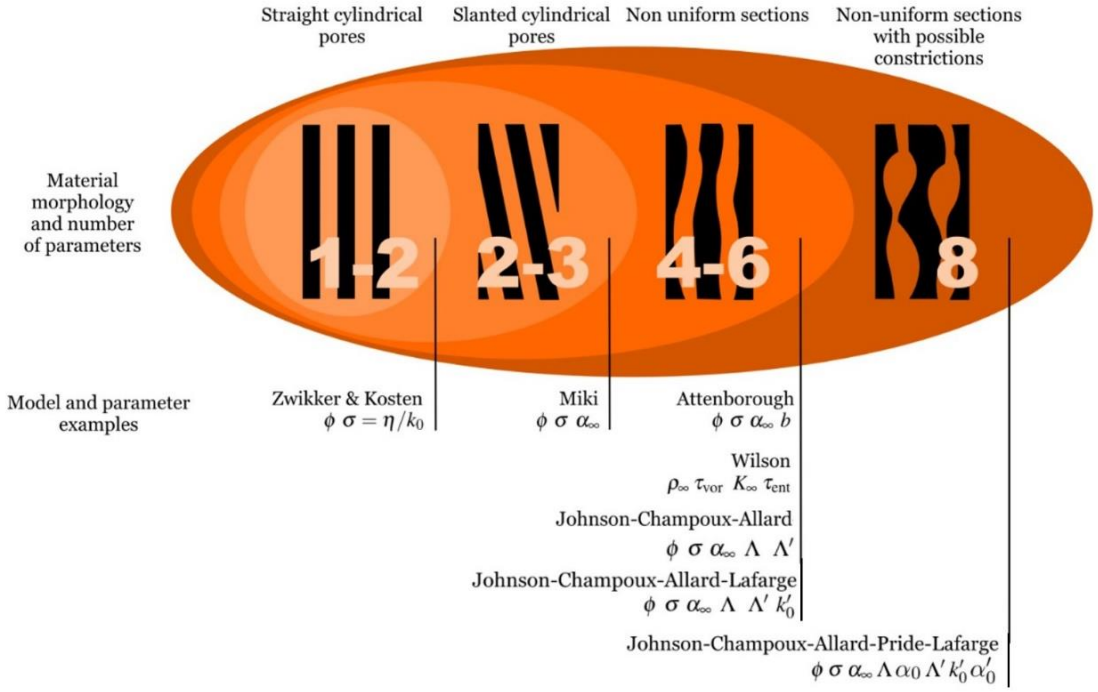

Fig. 1.3: Comparison of the sound propagation models in porous materials with rigid skeleton in terms of the number of parameters needed [7].

When a porous material is subjected to incident acoustic or sound waves, the scattered micro-pores inside can facilitate the penetration of the acoustic or sound waves into the porous material and the sound energy is primarily dissipated through viscous and thermal effects. The air molecules at the surface of the material and within its pores are forced to vibrate, and the friction of the air molecules on the pore walls will result in the conversion of the sound energy to heat. Meanwhile, the viscous energy dissipation is caused by the viscosity of the airflow within the materials, which also leads to the generation of heat [27]. Furthermore, the internal scattering and reflections of waves at the interfaces between the pores and pore walls, the material damping, and the resonance vibration of the pore walls can also contribute to the attenuation of sound energy [7]. As a result, porous materials are usually endowed with a broad frequency band for sound absorption [28-30] and therefore are widely used. In order to characterize the acoustic or sound energy absorption characteristics of such materials, various models have been established over the past few decades as shown in Fig. 1.3. In 1949, Zwikker and Kosten initially introduced analytical models for porous materials featuring very simple pore morphologies, such as slit-like or parallel cylindrical pores [31]. Subsequently, with the assumption of rigid and motionless skeletons, purely empirical models [32,33] were developed to describe the complex wave number and characteristic impedance employing power-law functions, which are dependent on the static airflow resistivity. In order to take more complicated pore morphologies inside the porous materials into account, more parameters were introduced in semi-phenomenological models

[34-37] such as the five-parameter Johnson-Champoux-Allard (JCA) model, and the eight-parameter Johnson-Champoux-Allard-Pride-Lafarge (JCAPL) model. The analytical models and the JCA model are applied extensively in this thesis, thus, they will be discussed in details in the next chapter for a deeper understanding.

However, the conventional porous materials have rather limited applications as they typically exhibit a satisfactory sound absorption performance only in the middle to high frequency range [28,38], which can be exemplified by a porous material made of the hemp fibres as shown in Fig. 1.2. In order to improve their low-frequency sound absorption capability, in the past few decades, the structural design of different porous materials was taken into consideration, and the concept of double porosity (DP) materials having two interconnected pores with significantly different characteristic sizes were put forward and investigated. A typical DP material is composed of periodically distributed rectangular or cylindrical macro-pores in a micro-porous medium, and Olny et al. [39-41] conducted a thorough study on the sound absorption properties of such DP materials as shown in Fig. 1.4 based on the homogenization method [42,43]. Compared with the single porosity materials, the low-frequency sound absorption coefficient of the DP materials exhibits a significant improvement [41,44]. Subsequently, an alternative form of the DP materials incorporating periodically arranged slits was suggested and demonstrated to exhibit favourable sound absorption characteristics. [45-47]. In addition to the DP materials, several structures combining porous materials with Helmholtz resonators were also proposed and investigated, which can enhance the low-frequency sound absorption performance [48-51]. For the purpose of broadening the sound absorption band at low frequencies, Lagarrigue et al. [52] introduced periodic slotted cylindrical resonant inclusions into the porous matrix and further suggested the utilization of the meta-porous materials consisting of complex unit-cells (UCs) incorporating two-dimensional (2D) resonant inclusions [53]. Furthermore, Long et al. [54] proposed a novel approach by integrating two split-rings into a local resonator, which was subsequently incorporated into a porous material to form a critically coupled sub-wavelength resonant system for the further enhancement of the sound absorption ability at low frequencies. Moreover, Yang et al. [55,56] implemented a direct insertion of the rigid partitions into the porous medium to generate local resonators for achieving a broadband sound absorption capability. Later, Kim and Park [57] designed a double resonant porous structure comprising a helical-shaped hollow slit absorber connected to a perforated membrane with an air cavity, aiming to enhance the low-frequency sound absorption performance. Additionally, porous composite structures [58-68] containing rigid or porous inclusions were also studied and demonstrated to exhibit a smoother and more regular sound absorption curve across a broad frequency range as exemplified in Fig. 1.5. In more recent years, Liu et al. [69] proposed a kind of gradually perforated porous material structure backed by a Helmholtz resonant cavity which shows a high potential with a commendable sound absorption performance.

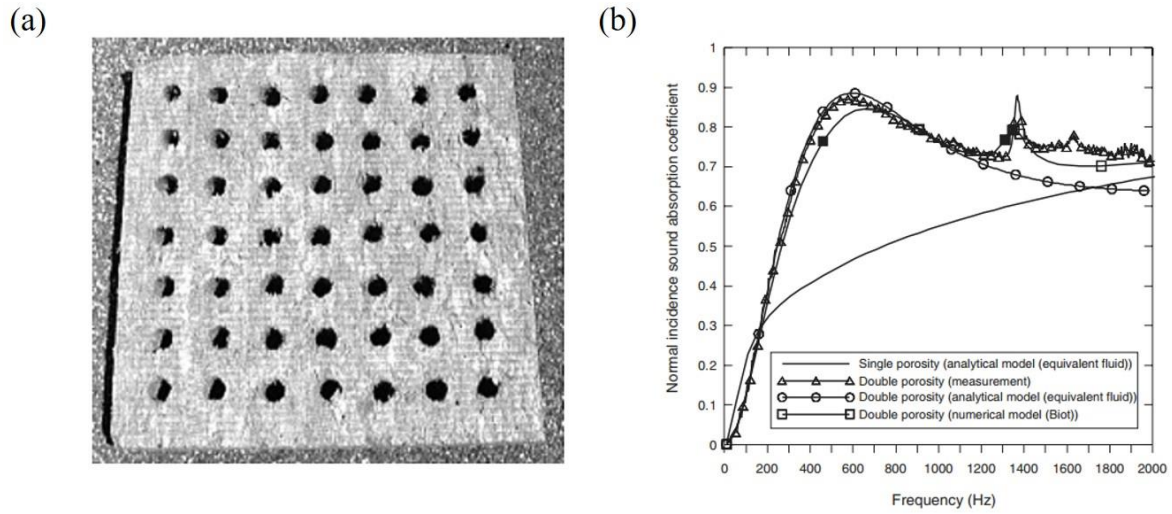

Fig. 1.4: (a) Example of a DP material: perforated rockwool. (b) Comparison of the normal incidence absorption coefficients by the analytical fluid equivalent model, numerical Biot model and measurement for a 5.75 cm thick rockwool, respectively [41].

In more recent years, the concept of metamaterials has been introduced for controlling acoustic waves, resulting in the rapid development of acoustic metamaterials. These artificial materials or structures, either periodic or non-periodic, offer novel approaches to manipulate acoustic waves. Acoustic metamaterials with a certain kind of periodicity but without local resonance mechanisms are also frequently referred to as phononic crystals in literature. If we simply classify acoustic metamaterials or phononic crystals based on their periodicity, they can be categorized into one-dimensional (1D), two-dimensional (2D), and three-dimensional (3D) ones as shown in Fig. 1.6 [70]. By designing and engineering acoustic metamaterials with more complex properties, unprecedented functionalities such as a negative refraction index can be obtained [71-74]. In this thesis, the concept of acoustic metamaterials will be utilized for improving the sound absorption and mitigation properties of porous materials. The acoustic metamaterials can be very simple in structure such as the meta-surfaces [75-78], meta-membranes [79-82] or meta-panels [83,84], though more complicated structures such as honeycomb [67,85-87] or labyrinthine [88-90] structures were also investigated and demonstrated to exhibit improved sound absorption abilities. Besides, alternative unique acoustic metamaterial structures [91-96] such as origami structures [97] have been also suggested and explored. One of the extraordinary acoustic wave propagation phenomena in acoustic metamaterials is the existence of the so-called frequency bandgaps, which designate such frequency ranges in which the acoustic waves cannot propagate [98-103]. The introduction of periodically distributed macro-perforations to a 2D structure is a very simple method to generate frequency bandgaps, and Liu et al. [104,105] further investigated the influences of the pore shapes on the band structures or dispersion curves of acoustic waves. Wang et al. [106,107] found that large bandgaps can be generated by cross-like holes. In addition

to acoustic metamaterials composed of conventional elastic materials that can generate bandgaps, those composed of viscoelastic materials can also induce bandgaps [108-112]. In this case, the structure incorporates a material damping mechanism [113,114], and the complex band structure or dispersion relation can be used to describe the acoustic wave propagation characteristics [115,116] including the behavior of the evanescent acoustic waves [117-119].

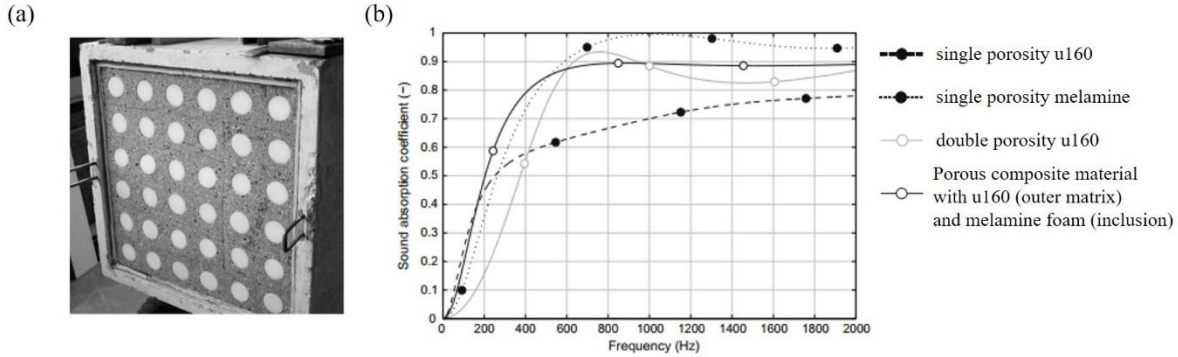

Fig. 1.5: (a) A 90mm thick porous composite sample made of u160 (outer matrix) and melamine foam (inclusion). (b) A 80 mm thick layer: Theoretical comparison of the sound absorption coefficients [59].

The above-mentioned research works were all based on the room temperature assumption. However, the noise reduction or sound absorption in high-temperature environments is also of vital importance, such as for the combustion chambers of gas turbines [120]. In 1976, Christie [121] first estimated the static airflow resistivity of porous materials at high temperatures through experiments, which was later verified by sun et al. [122] and Williams et al. [123], who investigated the impact of the high temperature on the acoustic parameters of the fibrous metallic materials by applying the principles of thermodynamics and the heat transfer theory considering the temperature-dependent material properties. Though many investigations [124-128] on the sound absorption performance of the fibrous metallic materials at high temperature were also carried out in more recent years, nevertheless, further enhancement is still needed in general.

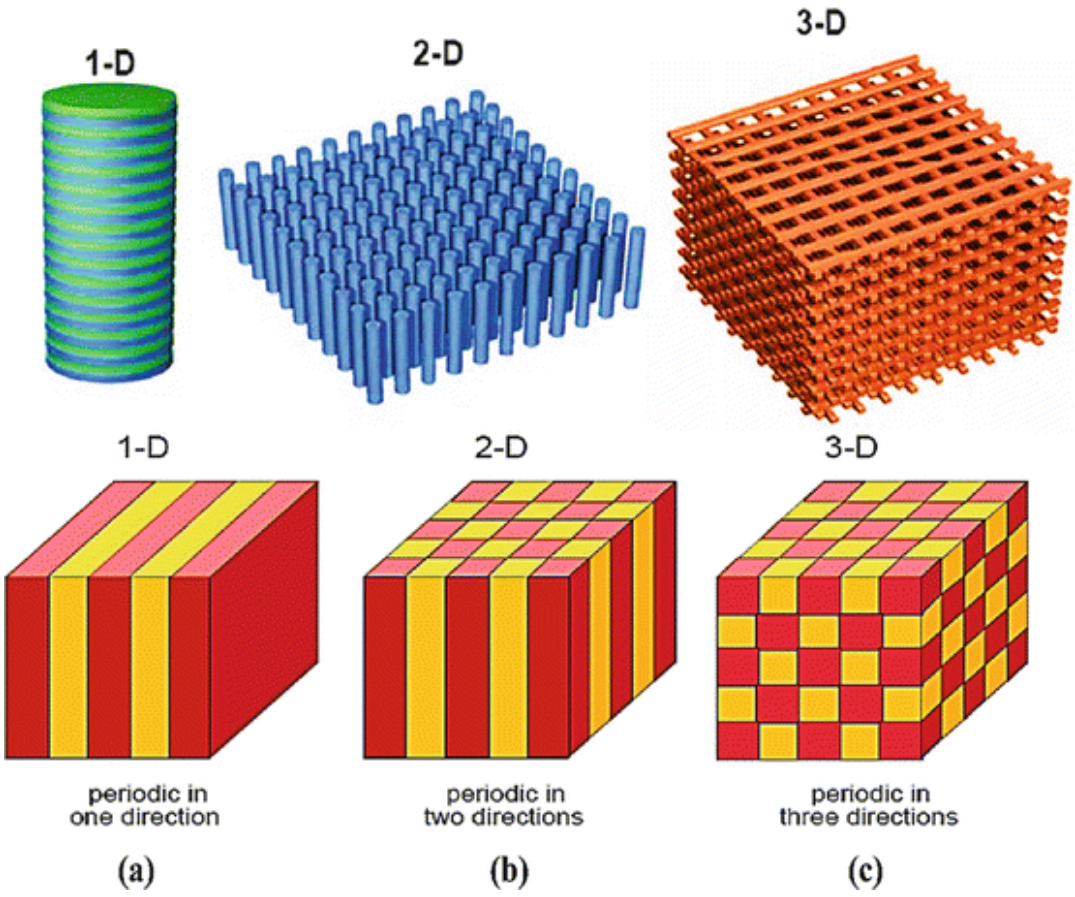

Fig. 1.6: Schematic illustrations of the metamaterials based on periodicity. (a) 1D, (b) 2D, (c) 3D [70].

1.2 Motivation and objectives of the thesis

Based on the above reviews on the relevant references and the state of the art, it is evident that the investigations of porous materials and acoustic metamaterial structures for acoustic wave absorption and mitigation have received significant attention, and extensive research works have been conducted. Nevertheless, there are still many open questions and problems which need further investigations. For instance, most previous research works were focused on the propagation of acoustic waves and the computation of band structures in acoustic metamaterial structures with macroscopic perforations. However, the propagation of acoustic waves and the calculation of band structures in porous metamaterials (PMs) are rarely taken into consideration. In particular, it should be noted that the presence of the microscopic pores in porous materials may lead to significant changes in the macroscopic material properties, which should be taken into account in the band structure analysis. Besides, from the perspective of the sound absorption, the Helmholtz resonators generally have good absorption properties in the low-to-mid frequency range, and they are frequently restricted to a very narrow frequency range for the sound absorption. In contrast, porous materials typically exhibit a wide

frequency range for the sound absorption in the middle-to-high frequency range but the low-frequency sound absorption performance is usually poor. Even though a better low-frequency sound absorption performance is feasible with the introduction of acoustic metamaterials, generally it is challenging to achieve simultaneous low-frequency and broadband sound absorption with a simple metamaterial structure. Moreover, further research is still needed to investigate the sound absorption performance of different porous materials and structures under high-temperature conditions.

Motivated by the aforementioned advantages and disadvantages of various sound-absorbing materials and structures as well as the research areas that require further investigations, the first objective of this thesis is to investigate the propagation of acoustic waves along the periodicity direction of the PMs, and establish adequate theoretical models and computational methods for calculating the band structures or dispersion curves and the wave transmission spectra. The band structures and the transmission spectra should be examined, and the formation of the bandgaps in different 1D PM structures should be studied in details to gain a deep understanding on the physical mechanisms for the acoustic wave absorption and mitigation characteristics. The pressure distribution inside the PM structures should also be explored to reveal the physical mechanisms. In addition, the effects of the geometrical and material parameters as well as the material combinations should be also be analyzed in details.

The second objective of this thesis is to design novel PM structures that exhibit improved sound absorption characteristics particularly at low frequencies, while still maintaining an overall effective sound absorption performance in a wide frequency range. To gain a deeper understanding of the sound absorption or sound energy dissipation process, the sound absorption mechanisms within the PM structures should be investigated. Besides, the effects of the geometrical and material parameters as well as the material/perforation combinations of the proposed acoustic metamaterial structures on the sound absorption and mitigation characteristics should be analyzed in order to provide a basis for their design and optimization to further enhance their sound absorption and mitigation performance. A thorough study of the sound absorption and mitigation characteristics for normally and as obliquely incident acoustic waves should also be addressed.

The third objective of the present thesis is devoted to the high-temperature effects on the sound absorption and mitigation characteristics of the proposed PM structures, which are also of great importance for practical engineering applications. In particular, the frequency spectra of the acoustic wave absorption characteristics of the proposed PM structures under high-temperature conditions will be evaluated and discussed.

In brief, this thesis endeavours to provide valuable insights into the acoustic wave propagation phenomena in PMs and structures, and to promote their advancements and applications for the novel acoustic wave control, absorption and mitigation as well as isolation technologies.

1.3 Structure of the thesis

The present thesis consists of 7 chapters as briefly described in the following.

In this chapter (Chapter 1), some literature and state-of-the-art reviews on the research works concerning porous materials and PM structures for the acoustic wave absorption are described, and the objectives of this thesis are illustrated.

In Chapter 2, some theoretical fundamentals which are essential and necessary to this thesis are presented. In particular, the theoretical models for acoustic wave propagation in porous materials and metamaterials are described in details. The governing equations are given, and different theoretical models for describing the material properties for porous materials are demonstrated.

In Chapter 3, some computational methods including the FEM and the TMM for calculating the sound absorption coefficients for porous materials and the band structures as well as the transmission spectra or frequency response for metamaterials are presented. Their accuracy for calculating the sound absorption coefficients by the FEM and TMM is validated by comparison with the experimental results, while their correctness for computing the band structures and the transmission spectra by the FEM and TMM are verified reciprocally.

In Chapter 4, the band structures of different 1D PM structures are studied, including the slit-perforated porous metamaterial (SPM), the porous composite metamaterial (PCM) and the slit-perforated multi-layered porous metamaterial (SMPM) structures. The band structures and the transmission spectra are calculated, and the bandgaps generated by different material arrangements are analyzed. Besides, the influence of the material and geometrical parameters are investigated.

In Chapter 5, the slit-perforated multi-layered porous metamaterial (SMPM) structure, which shows an outstanding acoustic wave absorption performance in the case of the acoustic waves incident perpendicularly to the periodicity direction of the structure, is investigated in details. Two homogenization methods are applied for the establishment of the theoretical model, which are compared with the numerical model and fairly good agreements are achieved. Not only the results for normally incident waves but also those for obliquely incident waves are presented, and the acoustic wave energy absorption mechanism inside the structure is explored. The effects of the geometrical parameters and the material composition ratio are also studied. Furthermore, the acoustic wave absorption performance at high temperatures is also demonstrated.

In Chapter 6, the novel multiscale porous metamaterial (MPM) structure is proposed and studied. Two kinds of the meso-pore distributions with the square and the hexagonal lattices are considered. The sound absorption coefficients for the normal acoustic wave incidence with two different material arrangements are calculated, which show a significant improvement compared with the DP materials.

The pressure distribution and the time-averaged power dissipation density are presented in order to explore the absorption mechanisms of the acoustic wave energy. Besides, the parametrical analysis is carried out to reveal the effects of the meso-pore size, the material composition ratio and the thickness of the structure. Subsequently, the sound absorption coefficients for obliquely incident acoustic waves are analysed, and the high temperature effects are explored.

In Chapter 7, the main research contributions of this thesis are summarized, and an outlook on future research works is also given.

Finally, a reference list is provided at the end of the thesis.

2. Theoretical fundamentals

In this chapter, some theoretical fundamentals regarding the acoustic waves, which are essential to this thesis, are presented in details. Firstly, the acoustic wave equations are derived. Then, the theoretical models for describing the acoustic wave propagation in porous materials are introduced. Moreover, the acoustic wave propagation problem in periodic metamaterials is described.

2.1 Governing equations of the acoustic waves

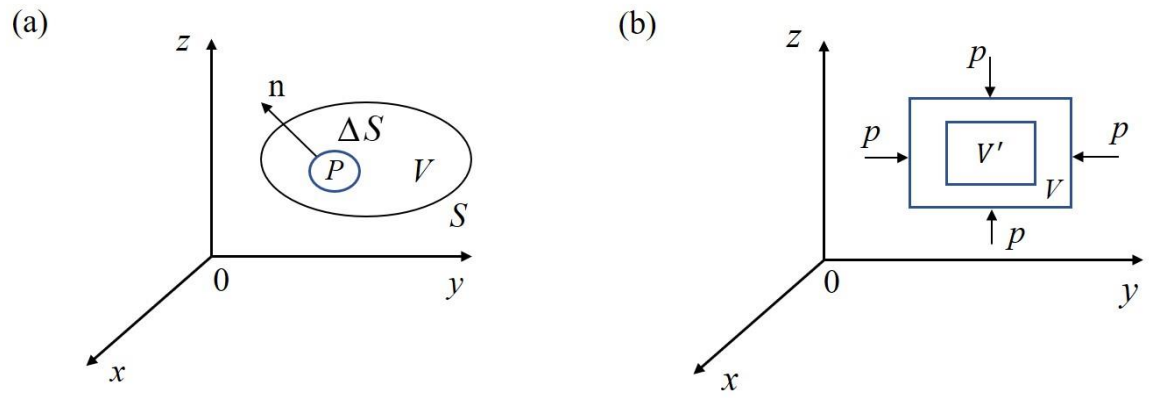

Fig. 2.1: Schematic sketch of (a) a volume V in a deformable medium, with S being the surface of V and ΔS an element of S around a point P that lies on S, and (b) the volume V subjected to a hydrostatic pressure p [26].

In the absence of body forces, the equations of motion of an elastic solid of the volume V as shown in Fig. 2.1(a) can be written as

$$\rho \frac{\partial^2 \mathbf{u}}{\partial t^2} = (\lambda + \mu) \nabla \, (\nabla \cdot \mathbf{u}) + \mu \nabla^2 \mathbf{u} \,, \tag{2.1}$$

where $\mathbf{u}$ is the displacement vector, ρ is the mass density of the medium, ∇ is the Nabla operator, λ and μ are the Lame constants, and ∇^2 is the Laplace operator. In the case of acoustic waves propagating in an inviscid fluid, μ vanishes. When the volume V is subjected to a hydrostatic pressure p as shown in Fig. 2.1(b), the dilatation ϑ can be expressed as

$$\vartheta = -p / \lambda \,. \tag{2.2}$$

The ratio $-p / \vartheta$ is the bulk modulus K of the material and the bulk modulus K for a fluid becomes simply λ. Thus, Eq. (2.1) is simplified to

$$\rho \frac{\partial^2 \mathbf{u}}{\partial t^2} = K\nabla\ (\nabla \cdot \mathbf{u}) . \tag{2.3}$$

For convenience, a displacement potential φ is introduced, which is related to the displacement vector $\mathbf{u}$ by

$$\mathbf{u} = \nabla\varphi. \tag{2.4}$$

Substitute Eq. (2.4) into Eq. (2.3) yields

$$\nabla^2\varphi = \frac{1}{c^2} \cdot \frac{\partial^2 \varphi}{\partial t^2} , \tag{2.5}$$

where $c = \sqrt{K / \rho}$ is phase velocity of the acoustic waves. As an example, a simple solution of Eq. (2.5) for a 1D time-harmonic acoustic wave propagating in the *x*-direction can be written as

$$\varphi(x,t) = \frac{A}{\rho\omega^2} \exp\left[j(-kx + \omega t) + \psi \right], \tag{2.6}$$

where $j = \sqrt{-1}$, ω is the angular frequency, A represents the wave amplitude, ϑ denotes the phase angle, and the wave number k is given by

$$k = \omega / c. \tag{2.7}$$

Thus, the phase velocity of the acoustic waves can be also expressed as

$$c = \omega / k . \tag{2.8}$$

Then, the displacement, the pressure and the particle velocity can be deduced from Eqs. (2.2), (2.4) and (2.6) as

$$u_x(x,t) = \frac{\partial \varphi}{\partial x} = -\frac{jkA}{\rho\omega^2} \exp\left[j(-kx + \omega t) + \psi \right], \tag{2.9}$$

$$p(x,t) = -K\vartheta = -K\nabla^2\varphi = A \exp\left[j(-kx + \omega t) + \psi \right], \tag{2.10}$$

$$v_x(x,t) = \frac{\partial u_x}{\partial t} = \frac{kA}{\rho\omega} \exp\left[j(-kx + \omega t) + \psi \right]. \tag{2.11}$$

The pressure and the particle velocity are related via the characteristic impedance Z_c by

$$v_x(x,t) = \frac{1}{Z_c} p(x,t), \tag{2.12}$$

and Z_c is related to the material properties by

$$Z_c = \left(\rho K\right)^{1/2}. \tag{2.13}$$

In principle, the acoustic wave propagation problems can be solved either by using Eq. (2.5) in conjunction with the corresponding boundary and initial conditions in the time-domain, or by using the Fourier-transformed form of Eq. (2.5) with the corresponding boundary conditions in the frequency-domain. In the former case, the frequency-domain solution $u(\boldsymbol{x},\omega)$ can be obtained by using the following Fourier-transform after the time-domain solution $u(\boldsymbol{x},\mathrm{t})$ has been obtained

$$u(\boldsymbol{x},\omega) = \mathbb{F}\left[u(\boldsymbol{x},t)\right] = \int_{-\infty}^{\infty} u(\boldsymbol{x},t)e^{-j\omega t}dt\,. \tag{2.14}$$

In contrast, the time-domain solution $u(\boldsymbol{x},\mathrm{t})$ can be obtained by using the inverse Fourier-transform when the frequency-domain solution $u(\boldsymbol{x},\omega)$ has been computed.

For acoustic wave propagation problems, the pressure p is often used as the physical quantity, and Eq. (2.5) becomes in the frequency-domain or time-harmonic case the following Helmholtz equation

$$\nabla^2 p + k^2 p = 0\,. \tag{2.15}$$

2.2 Acoustic wave propagation in porous materials

When the plane acoustic waves propagate in porous materials or narrow tubes, it is too complicated to establish a model which can characterize the dissipation mechanism inside exhaustively. Thus, with the assumption of motionless skeletons, the equivalent fluid model which characterizes the dissipation by the frequency-dependent complex density and complex bulk modulus is introduced, and the Helmholtz equation can be rewritten as

$$\nabla^2 p + \frac{\omega^2}{\tilde{c}_{eq}{}^2}\, p = 0\,, \tag{2.16}$$

where $\tilde{c}_{eq} = \sqrt{\tilde{K}_{eq}/\tilde{\rho}_{eq}}$ denotes the equivalent acoustic wave velocity, with $\tilde{\rho}_{eq}$ and $\tilde{K}_{eq}$ being the equivalent mass density and equivalent bulk modulus of the porous material, respectively. Thus, the determination of $\tilde{\rho}_{eq}$ and $\tilde{K}_{eq}$ of the porous materials is of vital importance for solving the Helmholtz equation. For this aim, three classes of models are developed, namely analytical models, semi-phenomenological models and empirical models and they are introduced in details in the following sections.

2.2.1 Analytical models

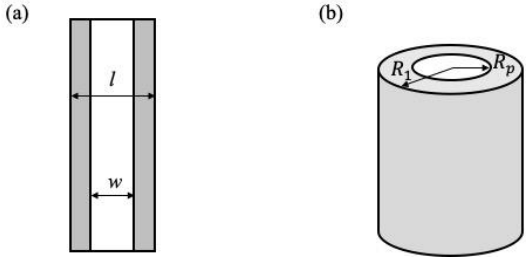

Fig. 2.2: Schematic sketch of a homogeneous medium with (a) slit-like pore, and (b) parallel cylindrical pore with circular cross-section.

The analytical models developed by Zwikker & Kosten [31] for regular-shape pores in a homogeneous medium are based on the Kirchhoff theory of sound propagating in cylindrical tubes. The viscosity effects and the thermal effects [129] are taken into account separately and the boundary conditions of zero air velocity and zero excess temperature (i.e., difference between actual and ambient temperatures) at the interface of the medium and the pore are supposed. Besides, the pressure p only varies along the direction of the incident wave and the hydraulic radius of the pore should be larger than 10 microns approximately and the frequency should be lower than 10^8 Hz [31].

The two most common cases which are also used in this work are the slit-like pores and the parallel cylindrical pores with circular cross-section as shown in Fig. 2.2 and the expressions for the equivalent dynamic mass density and dynamic bulk modulus are given below. For the slit perforation, we have

$$\rho_s = \frac{\rho_0}{\phi_s}\left[1-\frac{\tanh\left(\beta\sqrt{j}\right)}{\beta\sqrt{j}}\right]^{-1}, \tag{2.17}$$

$$K_s = \frac{\gamma P_0}{\phi_s}\left[1+(\gamma-1)\frac{\tanh\left(\beta\sqrt{j\,\mathrm{Pr}}\right)}{\beta\sqrt{j\,\mathrm{Pr}}}\right]^{-1}, \tag{2.18}$$

where P_0 is the ambient pressure, ρ_0 and γ are the mass density and the specific heat ratio of air, respectively, $\mathrm{Pr}=\eta C_p/\kappa$ is the Prandtl number where η and κ are the dynamic viscosity and the heat conductivity of air, respectively, C_p is the specific heat capacity of air at constant pressure, $\beta=\bar{r}\sqrt{\omega\rho_0/\eta}$, in which $\bar{r}$ is the so-called hydraulic radius which equals to $w/2$ for the case with slits and $\omega=2\pi f$ represents the angular frequency, $j=\sqrt{-1}$ represents the imaginary unit, $\phi_s=w/l$ for the case shown in Fig. 2.2(a), which is used to characterize the proportion of the pore to the whole structure.

For the parallel cylindrical pores with circular cross-section, we have

$$\rho_p = \frac{\rho_0}{\phi_p}\left[1-\frac{2}{\beta\sqrt{-j}}\frac{J_1\left(\beta\sqrt{-j}\right)}{J_0\left(\beta\sqrt{-j}\right)}\right]^{-1}, \tag{2.19}$$

$$K_p = \frac{\gamma P_0}{\phi_p}\left[1+(\gamma-1)\frac{2}{\beta\sqrt{-j\,\mathrm{Pr}}}\frac{J_1\left(\beta\sqrt{-j\,\mathrm{Pr}}\right)}{J_0\left(\beta\sqrt{-j\,\mathrm{Pr}}\right)}\right]^{-1}, \tag{2.20}$$

where J_i represents the i-th order Bessel function of the first kind, and $\phi_p = R_p^{\,2}/R_1^{\,2}$ for the case shown in Fig. 2.2(b) which represents the ratio of the slit size to the size of the whole structure.

2.2.2 Semi-phenomenological models

Several semi-phenomenological models were developed in the past few decades, such as Johnson-Champoux-Allard (JCA) model [34,35], Johnson-Champoux-Allard-Lafarge (JCAL) model [34,35,37] and Johnson-Champoux-Allard-Pride-Lafarge (JCAPL) model [35-37,130]. Among the above-mentioned models, the five-parameter JCA model is the most commonly used as these five parameters can all be measured without difficulties, which is also applied in this work. From the JCA model, the equivalent dynamic density and the equivalent dynamic bulk modulus of the porous material can be expressed as

$$\rho_m = \frac{\alpha_\infty \rho_0}{\phi}\left[1+\frac{\sigma\phi}{j\omega\rho_0\alpha_\infty}\sqrt{1+j\frac{4\alpha_\infty^{\,2}\eta\rho_0\omega}{\sigma^2\Lambda^2\phi^2}}\right], \tag{2.21}$$

$$K_m = \frac{\gamma P_0/\phi}{\gamma-(\gamma-1)\left[1-j\frac{8\kappa}{\Lambda'^2 C_p\rho_0\omega}\sqrt{1+j\frac{\Lambda'^2 C_p\rho_0\omega}{16\kappa}}\right]^{-1}}, \tag{2.22}$$

where P_0 is the ambient pressure, ρ_0 and γ are the mass density and the specific heat ratio of air, respectively, η and κ are the dynamic viscosity and the heat conductivity of air, respectively, C_p is the specific heat capacity of air at constant pressure, and $\omega = 2\pi f$ represents the angular frequency, $j = \sqrt{-1}$ represents the imaginary unit. Besides the above-mentioned air property parameters, the five particular material parameters include: porosity ϕ, static air-flow resistivity σ, tortuosity α_∞, viscous characteristic length Λ and thermal characteristic length Λ', and their definitions as well as measurements are introduced below.

1) Porosity ϕ

Porous materials such as fiberglass and foams consist of a solid frame together with pores filled with air. It should be noted that a closed pore inside the porous material belongs to the frame. The porosity is defined as the ratio of the air volume V_a to the total volume V_T of the porous material, which can be written as

$$\phi = V_a / V_T . \tag{2.23}$$

It is a key parameter for describing the property of the porous materials and can be directly measured [131,132].

2) Static air-flow resistivity σ

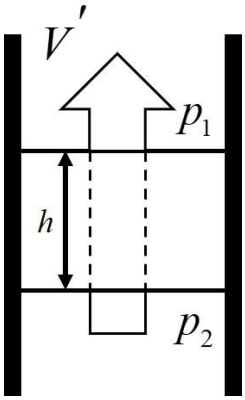

Fig. 2.3: Schematic representation of the static air-flow resistivity measurement [26].

The air-flow resistivity is a crucial parameter that governs the sound absorption of porous materials. It is defined as the ratio of the pressure difference across a sample of the material to the normal flow velocity through the material. A sketch of the set-up for measuring the air-flow resistivity σ is shown in Fig. 2.3. The material is placed in a pipe, and a steady flow of air passes through the material which induces a pressure difference and σ can be calculated by [26]

$$\sigma = (p_2 - p_1)/V'h , \tag{2.24}$$

where V' is the mean flow of air per unit area of the material, and h represents the thickness of the material. More ways of measuring the flow resistivity can be found in standards ISO9053 [133], ASTM C 522-3, Stinson [134] and Tang [135].

3) Tortuosity α_∞

The value of α_∞ can be considered as a measurement of the disorder in the material. It can be directly measured or estimated from ultrasound or impedance tube measurements [26]. Its mathematical

definition is given by Johnson et al. [34] as follows

$$\alpha_\infty = \frac{\frac{1}{V}\int_V v^2 dV}{\left(\frac{1}{V}\int_V v dV\right)^2}, \tag{2.25}$$

where V is the homogenization volume and v is the velocity of the fluid at high frequencies, when the viscous boundary layer is much smaller than the characteristic size of the pores. The tortuosity can partly characterize the visco-inertial effects at high frequencies.

4) Viscous characteristic length Λ

The viscous characteristic length is a parameter employed to characterize the viscous effects at medium and high frequencies. It was introduced by Johnson et al. [34] and can also be directly measured [136,137], which can be written as

$$\Lambda = 2\frac{\int_V v_i^2(\boldsymbol{r})dV}{\int_A v_i^2(\boldsymbol{r}_w)dA}. \tag{2.26}$$

The integration in the numerator is over the volume of the pores V and the integration in the denominator is over the surface A which is the fluid-frame interface in the pore, and $v(\boldsymbol{r})$ is the microscopic velocity of the fluid (air) in the pores. It should be noted that the quantity does not depend on the characteristics of the fluid (air).

5) Thermal characteristic length Λ'

The thermal characteristic length is a parameter used to describe the thermal effects at medium and high frequencies. It was proposed by Champoux et al. [35] and can be expressed as

$$\Lambda' = 2\frac{\int_V dV}{\int_A dA}. \tag{2.27}$$

The integral in the numerator is performed over the pore surfaces A in the elementary representative volume and the integral in the denominator is performed over the volume V of the pore. This parameter can be estimated by ultrasonic techniques [136].

2.2.3 Empirical models

Based on a large number of measurements on fibrous materials with porosity close to 1, the Delany and

Bazley model [32] was proposed. This empirical model can provide reasonable estimations of k and Z_c instead of the equivalent dynamic mass density and the equivlent dynamic bulk modulus, and is still widely used for its simplicity since only one parameter σ is needed to describe the acoustic behaviour of a porous material. However, it is less convenient to apply this model to complicated structures such as the DP material which will be presented in the following sections. The empirical expressions for the complex wave number k and the characteristic impedance Z_c are as follows:

$$k = \frac{\omega}{c_0}\left[1 + 0.0978\left(\frac{\rho_0 f}{\sigma}\right)^{-0.700} - j0.1890\left(\frac{\rho_0 f}{\sigma}\right)^{-0.595}\right], \tag{2.28}$$

$$Z_c = \rho_0 c_0\left[1 + 0.0571\left(\frac{\rho_0 f}{\sigma}\right)^{-0.754} - j0.0870\left(\frac{\rho_0 f}{\sigma}\right)^{-0.732}\right], \tag{2.29}$$

where ρ_0 and c_0 are the density of air and the speed of sound in air, respectively, f is the frequency, $\omega = 2\pi f$ is the angular frequency, and σ is the static air-flow resistivity of the porous material in the direction of the wave propagation. The range for the validity of these power law expressions is $0.01 < \frac{f}{\sigma} < 1.00$.

2.2.4 High temperature effects

Since the acoustic wave absorption is also crucial at high temperatures, in this section the effects of high temperature on the sound absorption characteristics of porous materials are studied. More specifically, how temperature can affect the material parameters of both air and porous materials is analysed.

In this thesis, it's assumed that the volume and internal morphology of the porous material do not change at high temperatures. Thus, among the five parameters of the porous materials in the JCA model, only the static air-flow resistivity varies significantly with temperature t [138] and its temperature dependence can be described by Christie's power law [121]

$$\sigma = \sigma_0\left(\frac{t + 273.15}{293.15}\right)^{0.6}, \tag{2.30}$$

where σ_0 is the static airflow resistivity at the room temperature of t_0=20°C or t_0=293.15K and this equation was further verified by Williams et al. [123] using experimental data measured with different fibrous materials (i.e. rockwool, basalt wool and an E-glass fibre).

Table 2.1: Physical parameters of air at different temperatures

t (°C)	ρ_0 (kg/m^3)	c_0 (m/s)	η (10^{-5} Pa·s)	C_p (J/kg/K)	γ (1)	κ (10^{-2} W/m/K)
20	1.23	343	1.82	1006.4	1.402	2.55
100	0.94	387	2.19	1011.5	1.397	3.11
300	0.614	476	2.98	1045.4	1.379	4.37
500	0.456	549	3.66	1092.7	1.356	5.48

Nevertheless, the physical properties of air exhibit a significant dependence on temperature. The software REFPROP of NIST can be used to compute the corresponding physical parameters of air at selected temperatures at the atmospheric pressure $P_0 = 101330\text{Pa}$ based on numerous fitted curves derived from experimental data, and the corresponding parameters are listed in Table 2.1.

Once the corresponding air and material parameters at high temperatures are obtained, they can be applied to the equations presented in the previous sections for describing the acoustic wave propagation in porous materials at high temperatures.

2.2.5 Double porosity theory

As mentioned in Chapter 1, due to the disadvantage of using single porous materials, the DP materials were proposed, which can improve the sound absorption characteristics. The DP refers to the micro-pores of the porous materials and the macro-pores which are of different characteristic sizes, and a typical DP structure which consists of a porous material matrix with macro-pores is shown in Fig. 2.4(a). The homogenization procedure and the determination of $\tilde{\rho}_{eq}$ and $\tilde{K}_{eq}$ of such structures are demonstrated in details in the following part, as this theory is applied extensively in this thesis.

In order to describe such inhomogeneous medium and explore their sound absorption characteristics with normally incident acoustic wave, the DP theory was proposed and established by Olny et al [40,41]. The detailed theory is not explained here for the sake of brevity, and only the key points which are necessary for this thesis are highlighted. Due to the periodicity of the structure, the UC shown in Fig. 2.4(b) is extracted, and to simplify the analysis, an equivalent cylindrical UC shown in Fig. 2.4(c) is adopted with $a^2 = \pi R_1^2$.

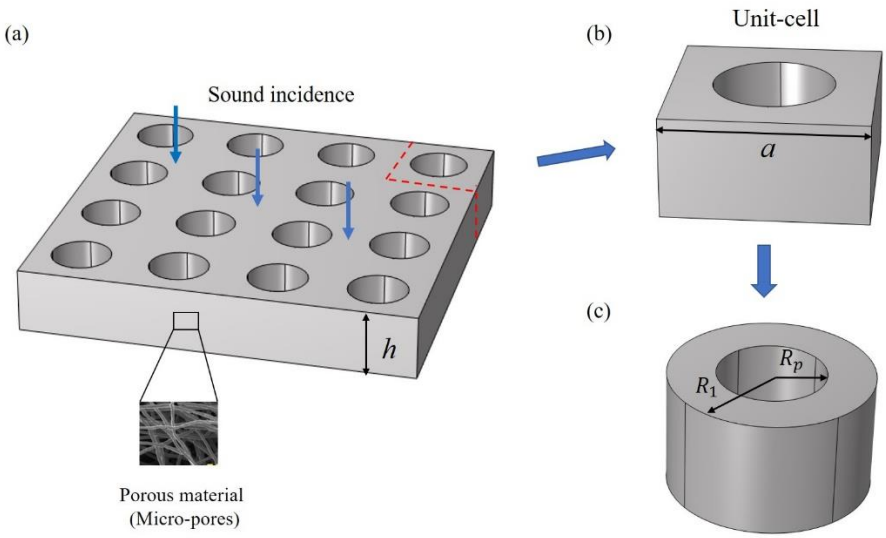

Fig. 2.4: (a) Schematic sketch of a DP structure, (b) the UC and (c) the equivalent cylindrical UC.

Here we define $\phi_p = R_p^{\,2}/R_1^{\,2}$ to represent the proportion of the pore to the porous material matrix. Due to the the difference of scales between the micro-pores inside the porous material and the macro-pore and the difference between the material properties of air and the porous material, two cases are considered, namely low permeability contrast (LPC) case and high permeability contrast (HPC) case. The HPC case occurs when

$$\omega \ll \omega_{VM},\ \omega_d \ll \omega_{VM} \tag{2.31}$$

is met, where $\omega_{VM} = \sigma_m \phi_m / \left(\rho_0 \alpha_{\infty m}\right)$ is a cut-off angular frequency, and it is defined by taking the limit of the dynamic viscous permeability $q(\infty) = \eta\phi_m / j\omega\rho_0\alpha_{\infty m}$ equal to the static viscous permeability $q_0 = \eta/\sigma_m$. At frequencies below this cut-off frequency, the viscous forces dominate in the micro-pore domain, while above this frequency, the inertial forces dominate. In Eq. (2.31), $\omega_d = (1-\phi_p)P_0/\phi_m\sigma_m D(0)$ and $D(0)$ is a geometric parameter. For a circular cross-section, it can be evaluated analytically as [40,139]

$$D(0) = \frac{R_1^{\,2}}{4}\left(\ln\left(\frac{1}{\phi_p}\right) - \frac{3}{2} + 2\phi_p - \frac{\phi_p^{\,2}}{2}\right). \tag{2.32}$$

For both LPC and HPC cases, the equivalent dynamic mass density is obtained by the mix law as

$$\rho_{dp} = \left[\frac{1}{\rho_p} + \left(1-\phi_p\right)\frac{1}{\rho_m}\right]^{-1}, \tag{2.33}$$

where ρ_p is the equivalent density calculated in Section 2.2.1 depending on the pore shape, and ρ_m is the equivalent density of the porous material matrix with single porosity. For the LPC case, the macroscopic air-flow participates in both the micro-pores network and the macro-pore network, and the acoustic pressure presents a homogeneous distribution along the wave propagation direction. Thus, the equivalent bulk modulus is also calculated based on the mix law by

$$K_{dp}^{L}=\left[\frac{1}{K_p}+\left(1-\phi_p\right)\frac{1}{K_m}\right]^{-1}, \tag{2.34}$$

where K_p is the equivalent bulk modulus calculated in Section 2.2.1 depending on the pore shape and K_m is the equivalent bulk of the porous material matrix with single porosity. However, for the HPC case, the macroscopic air-flow does not involve the microscopic air-flow and the acoustic pressure distribution at the interface of the two pore networks are affected remarkably. Therefore, a new function $F_d(\omega)$ is introduced to describe this pressure diffusion effect as

$$F_d(\omega)=1-j\frac{\omega}{\omega_d}\frac{D(\omega)}{D(0)}, \tag{2.35}$$

and a semi-phenomenological expression for $D(\omega)$ is given by [40]

$$D(\omega)=\frac{D(0)}{j\dfrac{\omega}{\omega_d}+\sqrt{1+j\dfrac{M_d}{2}\dfrac{\omega}{\omega_d}}}. \tag{2.36}$$

Here, $D(0)$ is defined by Eq. (2.32), and the form parameter M_d is given by [40]

$$M_d=\frac{8D(0)}{\Lambda_d{}^2(1-\phi_p)}, \tag{2.37}$$

where

$$\Lambda_d=\frac{2h\left(\pi R_1{}^2-\pi R_p{}^2\right)}{2\pi hRp+\pi R_1{}^2-\pi R_p{}^2}. \tag{2.38}$$

Then the equivalent bulk modulus is expressed as

$$K_{dp}^{H}=\left[\frac{1}{K_p}+\left(1-\phi_p\right)\frac{F_d\left(\omega\dfrac{P_0}{\phi_m K_m}\right)}{K_m}\right]^{-1}. \tag{2.39}$$

The above theory is also applicable to slit perforation with $D(0)=b^2(1-\phi_s)/3$ and $\Lambda_d=2bh/(b+h)$. For the same configuration as Fig. 2.2(a), b equals to (l-w)/2.

2.2.6 Porous composite theory

The porous composite structure can contain several different porous materials, and here we take a simple porous composite plate which consists of two porous materials shown in Fig. 2.5 as an example to show the calculation procedure of the equivalent density and bulk modulus of such structures.

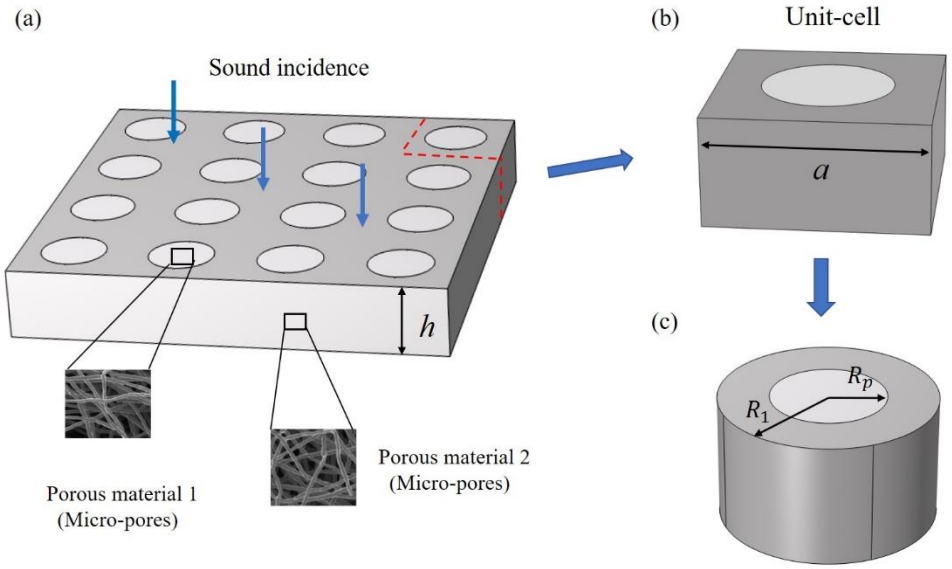

Fig. 2.5: (a) Schematic sketch of a porous composite structure, (b) the UC and (c) the equivalent cylindrical UC.

The equivalent dynamic density is also deduced by the mixture law as

$$\rho_{pc}=\left[\frac{\phi_p}{\rho_{m1}}+\left(1-\phi_p\right)\frac{1}{\rho_{m2}}\right]^{-1}, \tag{2.40}$$

where ρ_{m1} and ρ_{m2} denote the equivalent mass density of the two constituent porous materials, respectively. Meanwhile, the equivalent bulk modulus is obtained by

$$K_{pc}=\left[\frac{\phi_p}{K_{m1}}+\left(1-\phi_p\right)\frac{F_d}{K_{m2}}\right]^{-1}, \tag{2.41}$$

where F_d can be calculated by Eqs. (2.35)-(2.38), and K_{m1} and K_{m2} denote the equivalent bulk modulus of the two constituent porous materials, respectively.

2.2.7 Determination of the acoustic wave absorption characteristics

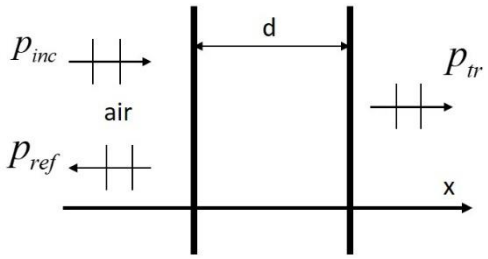

Fig. 2.6: Plane waves propagate from air into a porous material layer.

When the acoustic waves propagate from air into a porous material layer of thickness *d* as shown in Fig. 2.6, three kinds of the wave motion will occur: reflection, transmission and absorption. Therefore, the total sound energy can be regarded as the sum of the energy being reflected, absorbed and transmitted, i.e.,

$$E_{inc} = E_{tr} + E_{ref} + E_a , \tag{2.42}$$

where E_{inc} is the total incident acoustic wave or sound energy, E_{tr}, E_{ref} and E_a are the transmitted, reflected and absorbed sound energy, respectively.

The sound absorption coefficient α is often used to characterize the sound absorption ability of the porous material. The closer α to 1 is, the better the sound absorption ability is. It is calculated by the proportion of the energy absorbed in the material to the total energy of the incidence wave and can be deducted from the transmitted and reflected energy as

$$\alpha = \frac{E_a}{E_{inc}} = 1 - \frac{E_{tr} + E_{ref}}{E_{inc}} . \tag{2.43}$$

Meanwhile, the reflection coefficient can be written as the ratio of the pressure p_{ref} induced by the reflected outgoing waves and that generated by the incident waves p_{inc} at the surface of the layer:

$$R = \frac{p_{ref}}{p_{inc}} , \tag{2.44}$$

and the transmission coefficient can be written as the ratio of the pressure transmitted through the layer p_{tr} to the pressure generated by the incident waves p_{inc}, i.e.,

$$T = \frac{p_{tr}}{p_{inc}} . \tag{2.45}$$

Hence, the sound absorption coefficient can be rewritten as

$$\alpha = 1 - |R|^2 - |T|^2 . \tag{2.46}$$

2.3 Acoustic wave propagation in metamaterial structures

2.3.1 Bloch theorem

Time-harmonic acoustic waves propagating along the periodicity direction of the metamaterial structures can be described by the Bloch's theorem, which can be expressed for the pressure as

$$p(\mathbf{r}) = p_k(\mathbf{r}) e^{j(\mathbf{k}\cdot\mathbf{r})}, \tag{2.47}$$

where **r** is the position vector, p is the acoustic pressure, $p_k(\mathbf{r})$ is a periodic function whose periodicity is the same as the periodic material or structure and **k** is the Bloch wave vector in the irreducible Brillouin zone as shown in Fig. 2.7(c).

According to Eq. (2.47), with **a** denoting the lattice constant vector, the periodic boundary conditions for the unit-cell (UC) can be written as

$$p(\mathbf{r}+\mathbf{a}) = p(\mathbf{r}) e^{j(\mathbf{k}\cdot\mathbf{a})}. \tag{2.48}$$

2.3.2 Band structure analysis

For an infinite periodic metamaterial structure, the band structure or dispersion relation analysis is often used to investigate its acoustic wave propagation characteristics. For example, for a typical 2D metamaterial shown in Fig. 2.7(a), the UC shown in Fig. 2.7(b) is often used for the calculation and the Bloch's periodic boundary conditions are applied to the opposite boundaries. By substituting Eq. (2.47) into the equations of motion and considering the periodicity of the structure, an eigenvalue equation which contains both the wave vector and the frequency can be formulated. Then the dispersion relations or band structures can be calculated in two ways. The first approach is often called $\omega(k)$-approach as the eigenfrequency ω is calculated by varying the wave vector **k** along the boundary of the first irreducible Brillouin zone (IBZ) of the UC as shown in Fig. 2.7(c). On the contrary, the second approach which is called $k(\omega)$-approach is realized by giving the eigenfrequencies ω and compute the wave vector **k**. The wave vector can be usually expressed as $\mathbf{k} = \mathbf{k}_r + j\mathbf{k}_i$ with the real part describing the propagating waves and the imaginary part denoting the wave attenuation. Then the bandgaps and pass-bands can be identified from the band structures. In the frequency ranges of the bandgaps, the acoustic waves are forbidden to travel through the material, which is ideal for noise control.

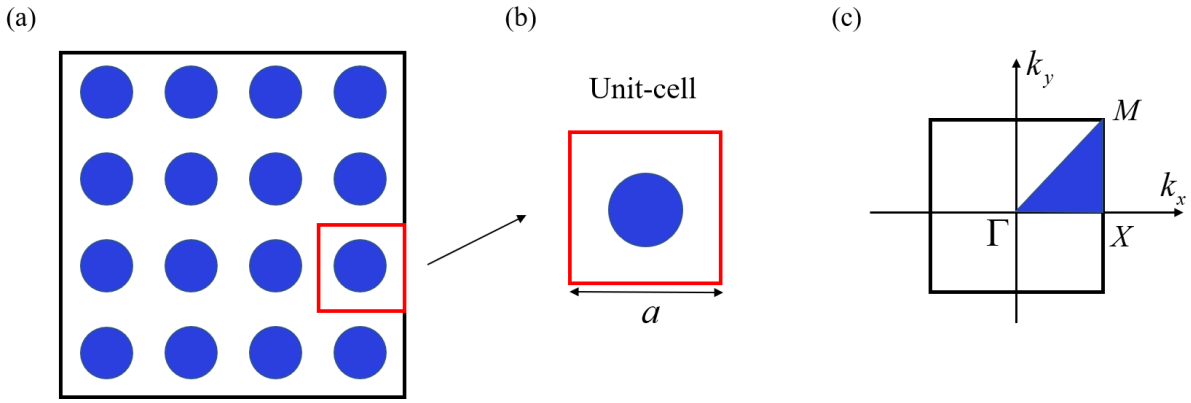

Fig. 2.7: (a) Schematic diagram of a 2D metamaterial structure, (b) the UC, (c) first irreducible Brillouin zone (IBZ).

2.3.3 Wave transmission analysis

Another way to explore the acoustic wave propagation characteristics is the wave transmission analysis of the metamaterial structure, which can be considered as a dynamic response analysis of the periodic material or structure. For a given incident acoustic wave, the transmitted acoustic wave can be calculated and the transmission coefficient is defined by Eq. (2.45). The transmission loss is often used, which can be calculated from the transmission coefficient as

$$TL = 10\log(|T|^2). \tag{2.49}$$

From the transmission spectra or frequency responses, the bandgaps and the pass-bands can be obtained. However, this technique is not as accurate as the band structure analysis for the determination of the edges of the bandgaps.

2.4 Conclusions

In this chapter, some theoretical fundamentals are presented and described in details, which are required for this thesis. First, the fundamentals of acoustic waves are elaborated and the Helmholtz equation is set forth to describe the acoustic waves propagating in a lossless fluid. Then the Helmholtz equation is further applied to porous materials and complex parameters $\tilde{\rho}_{eq}$ and $\tilde{K}_{eq}$ are introduced to describe the properties of porous materials accounting for the dissipation. In order to calculate the $\tilde{\rho}_{eq}$ and $\tilde{K}_{eq}$, three types of models are presented, namely analytical models, semi-phenomenological models and empirical models. Then the material properties at high temperatures are explored. Besides the conventional porous materials, the DP theory and the porous composite theory are also described which are the basis for this thesis. Furthermore, the determination of acoustic wave absorption characteristics of porous materials including the reflection coefficient, transmission coefficient and sound absorption

coefficient are demonstrated.

In addition, the Bloch's theorem which describes the propagation of acoustic waves in periodic metamaterial structures is introduced and the periodic boundary conditions for metamaterial structures are deduced. In the end, the band structure or dispersion relation and the wave transmission analysis which are used to characterize the acoustic wave propagation in periodic metamaterial structures are presented.

3. Computational methods

Acoustic wave propagation problems in periodic materials and structures can be solved analytically in only some special and simple cases. Thus, many numerical and computational methods have been developed to deal with such problems, for instance, the plane wave expansion method (PWEM), the boundary element method (BEM), the finite element method (FEM), the transfer matrix method (TMM) and the meshless methods, etc. Each of these methods has its own advantages and drawbacks, which will not be introduced thoroughly in this thesis. However, some details on the TMM and FEM will be given in this chapter as these two methods are mainly adopted in this thesis.

3.1 Transfer matrix method (TMM)

3.1.1 Calculation of the sound absorption coefficient

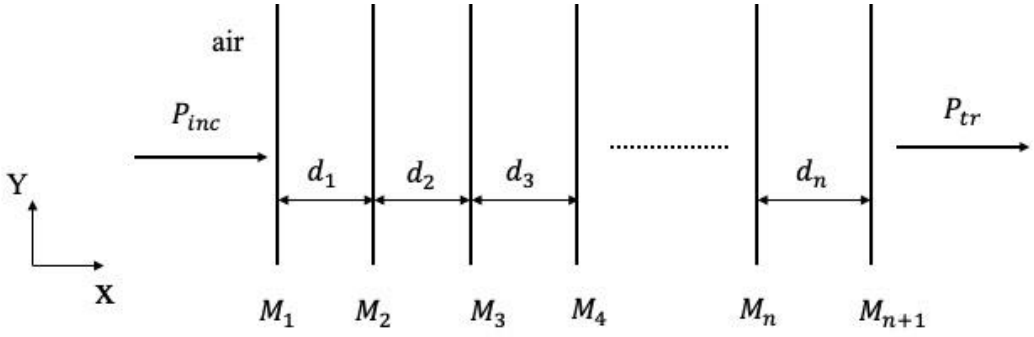

Fig. 3.1: An incident acoustic plane wave propagates in a multi-layered porous material structure.

Consider a plane acoustic wave impinging upon a structure consisting of *n* layers of porous materials shown in Fig. 3.1, the acoustic field at each interface is completely defined by the vector

$$\mathbf{V}^f = \left[p,\ v\right]^T. \tag{3.1}$$

The homogeneous layers can be modelled analytically by the transfer matrix method [140,141], and the acoustic pressure and the normal acoustic particle velocities on the two faces of each layer can be related by the transfer matrix

$$\begin{bmatrix} p \\ v \end{bmatrix}_{x(M_i)} = \mathbf{t}_i \begin{bmatrix} p \\ v \end{bmatrix}_{x(M_{i+1})} = \begin{bmatrix} t_{i,11} & t_{i,12} \\ t_{i,21} & t_{i,22} \end{bmatrix} \begin{bmatrix} p \\ v \end{bmatrix}_{x(M_{i+1})}, i = 1, 2...n, \tag{3.2}$$

where $\mathbf{t}_{i,mn}$ are the coefficients of the transfer matrix $\mathbf{t}_i$. Assuming the *i*th porous layer with a thickness d_i can be considered as homogeneous, isotropic equivalent fluid layer with rigid and motionless skeletons, the normal incidence transfer matrix $\mathbf{t}_i$ can be written as [26]

$$\mathbf{t}_i = \begin{bmatrix} \cos k_i d_i & jZ_{c,i} \sin k_i d_i \\ \dfrac{j}{Z_{c,i}} \sin k_i d_i & \cos k_i d_i \end{bmatrix}, \tag{3.3}$$

where k_i and $Z_{c,i}$ are the wave number and the characteristic impedance of the porous material, respectively. Since the structure consists of *n* layers of porous materials, the total transfer matrix can be expressed as

$$\mathbf{T}_n = \prod_1^n \mathbf{t}_i = \begin{bmatrix} T_{11} & T_{12} \\ T_{21} & T_{22} \end{bmatrix}. \tag{3.4}$$

The acoustic pressure and the normal acoustic particle velocities on the two sides of the structure can be related as

$$\mathbf{V}^f_{x(M_1)} = \mathbf{T}_n \mathbf{V}^f_{x(M_{n+1})}. \tag{3.5}$$

Based on the transfer matrix $\mathbf{T}_n$, the surface impedance Z_s of the structure can be written as

$$Z_s = \frac{T_{11} Z_0 + T_{12}}{T_{21} Z_0 + T_{22}}, \tag{3.6}$$

where Z_0 denotes the characteristic impedance of air. For a single layer, it can be simplified to

$$Z_s = Z_{c,i} \frac{-jZ_0 \cot k_i d_i + Z_{c,i}}{Z_0 - jZ_{c,i} \cot k_i d_i}. \tag{3.7}$$

With an anechoic termination, the transmission coefficient *T* and the reflection coefficient *R* can be expressed respectively as [142]

$$T = \frac{2e^{jkd}}{T_{11} + T_{12}/Z_0 + Z_0 T_{21} + T_{22}}, \tag{3.8}$$

$$R = \frac{T_{11} + T_{12}/Z_0 - Z_0 T_{21} - T_{22}}{T_{11} + T_{12}/Z_0 + Z_0 T_{21} + T_{22}}. \tag{3.9}$$

A special but common case is that the porous structure is backed by a rigid impervious wall. In this case, the surface impedance of a single layer can be simplified by considering Z_0 tending to infinity as

$$Z_s = -jZ_{c,i} \cot k_i d_i, \tag{3.10}$$

and the reflection coefficient is reduced to

$$R = \frac{T_{11} - Z_0 T_{21}}{T_{11} + Z_0 T_{21}}, \tag{3.11}$$

which can be rewritten as

$$R = \frac{Z_s - Z_0}{Z_s + Z_0}. \tag{3.12}$$

As no energy can be transmitted through the structure and T becomes 0, we have for the sound absorption coefficient

$$\alpha = 1 - |R|^2. \tag{3.13}$$

The above calculation is also applicable to the situation with oblique sound incidence by substituting k_i with $k_i \cos\theta$, and $Z_{c,i}$ with $Z_{c,i} \cos\theta$ assuming $\theta = 0$ as the normal sound incidence. The reflection coefficient turns into

$$R = \frac{Z_s \cos\theta - Z_0}{Z_s \cos\theta + Z_0}, \tag{3.14}$$

and the sound absorption coefficient with an oblique sound incidence can be calculated by Eq. (3.13).

3.1.2 Calculation of the band structures and the transmission spectra

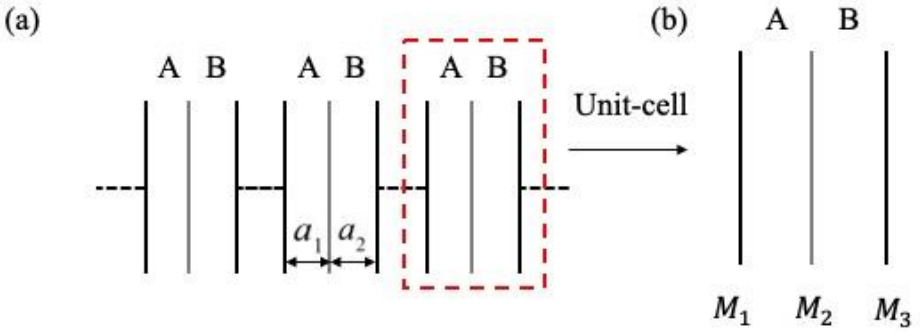

Fig. 3.2: (a) Schematic diagram of 1D metamaterial structure with two periodically distributed materials and (b) UC.

In this section, the calculation of the band structure by the TMM is demonstrated and we take a typical 1D metamaterial structure with two periodically distributed materials as shown in Fig. 3.2 as an example. The lattice constant $a=a_1+a_2$ and the structure is assumed to be infinitely large in the two other dimensions. Considering the periodicity of the structure and for the sake of simplicity, the UC of the structure shown in Fig. 3.2(b) is investigated. Based on the Bloch's theorem presented in Section 2.3.1, the acoustic field at the two sides of the UC can be related by the following equation

$$\mathbf{V}^f_{x(M_1)} = e^{-j\mathbf{k}a}\mathbf{V}^f_{x(M_3)}. \tag{3.15}$$

Based on the total transfer matrix and Eq. (3.15), we have

$$\mathbf{V}^{f}_{x(M_1)} = \mathbf{T}_2 \mathbf{V}^{f}_{x(M_3)} . \tag{3.16}$$

Combining Eqs. (3.15) and (3.16), an eigenvalue equation can be obtained as

$$(\mathbf{T}_2 - e^{-j\mathbf{k}a}\mathbf{I})\mathbf{V}^{f} = \mathbf{0} . \tag{3.17}$$

By calculating the determinant of the matrix $\mathbf{T}_2$ at different frequencies, the dispersion relation between the wave vector **k** and the frequency ω can be obtained, which is a $k(\omega)$-approach as introduced in Section 2.3.2. This method is also valid for UCs with multiple layers as long as $\mathbf{T}_n$ is changed accordingly, since Eq. (3.5) only relates the two sides of the UC and is only dependent on the lattice constant *a*.

As for the transmission loss, they can be obtained easily by Eqs. (2.49), (3.4) and (3.8).

3.2 Finite element method (FEM)

The FEM is a well-established numerical method which is widely used in engineering. It is based on the weak-from or variational formulation of the governing partial differential equations of the problem and the scheme of mesh-type discretization. The standard procedure of the FEM can be found in many textbooks and literatures so it will not be described in details in this section and we will only briefly present some information which is necessary for our present work.

The FEM can be applied for the numerical simulation of the acoustic wave propagation problems in porous materials and structures. It is capable of not only computing the sound absorption coefficient and the transmission spectra but also the band structures of different porous materials and metamaterial structures. The FEM leads to the following discrete eigenvalue equation for the UC

$$(\mathbf{K} - \omega^2 \mathbf{M}) \cdot \mathbf{p} = \mathbf{0} , \tag{3.18}$$

in which **K** and **M** are the stiffness and mass matrices, and **p** is the pressure vector related to the FE nodes, respectively.

In this thesis, the commercial FEM software COMSOL Multiphysics is used owing to its convenience and flexibility. The “Pressure Acoustics Module - Frequency Domain” is used for the calculation of the sound absorption coefficient as well as the transmission spectra and the PDE module is used for the calculation of the band structures or dispersion relations and they will be demonstrated in more details in the following subsections.

3.2.1 Calculation of the sound absorption coefficient

The "Pressure Acoustics Module - Frequency Domain" is used as it's more concise and appropriate than the time-domain approach for the calculation of the sound absorption coefficient. Besides, in the poroacoustic module, the theoretical models for describing the porous materials including the JCA model are already implemented, which can facilitate the modelling procedure. By giving an incident acoustic wave or background pressure field, the acoustic field inside the porous material or structure can be computed and the pressure at each point is obtained. Based on the pressure obtained, the density of the time-averaged dissipated power can be derived and previous works [39] have revealed that the density of the time-averaged dissipated power inside a porous material can be divided into contributions through viscous and thermal effects

$$e_{diss} = e_{diss}^{v} + e_{diss}^{t}, \tag{3.19}$$

and the density of the time-averaged power dissipated through the viscous effects can be obtained by

$$e_{diss}^{v} = \frac{1}{2}\mathrm{Im}\left(\frac{1}{\omega\tilde{\rho}_{eq}}\nabla p\cdot\nabla p^{*}\right), \tag{3.20}$$

where p^{*} represents the complex conjugate of the acoustic pressure p. The density of the time-averaged power dissipated through the thermal effects can be calculated by

$$e_{diss}^{t} = -\frac{1}{2}\mathrm{Im}\left(\frac{\omega}{\tilde{K}_{eq}}p\cdot p^{*}\right). \tag{3.21}$$

Based on Eqs. (3.19)-(3.21), the total time-averaged dissipation power density can be written as

$$e_{diss} = \frac{1}{2}\mathrm{Im}\left[\frac{1}{\omega\tilde{\rho}_{eq}}\nabla p\cdot\nabla p^{*}\right] - \frac{1}{2}\mathrm{Im}\left[\frac{\omega}{\tilde{K}_{eq}}p\cdot p^{*}\right]. \tag{3.22}$$

The time-averaged dissipation power of the porous material can be obtained by taking the volume integration of the time-averaged dissipation power density as

$$E_{diss} = \int_{V} e_{diss}\,dV = \frac{1}{2}\mathrm{Im}\left[\int_{V}\frac{1}{\omega\tilde{\rho}_{eq}}\nabla p\cdot\nabla p^{*}\mathrm{d}V\right] - \frac{1}{2}\mathrm{Im}\left[\int_{V}\frac{\omega}{\tilde{K}_{eq}}p\cdot p^{*}\mathrm{d}V\right]. \tag{3.23}$$

For a plane normally incident acoustic wave of amplitude p_0, the incident power is given by

$$E_{inc} = S\left|p_0\right|^2 \big/ 2\rho_0 c_0, \tag{3.24}$$

where S is the cross-section of the incident waveguide, which is the surface of the porous material subject to the incident wave. As the energy dissipated in a porous material can be also referred to as the energy absorbed by a porous material and time-averaging is taken for the calculation, the sound

absorption coefficient is deduced as

$$\alpha = E_{diss} / E_{inc} \,. \tag{3.25}$$

3.2.2 Calculation of the transmission spectra

For the calculation of the transmission spectra, the boundary condition of air impedance should be defined for the outbound of the porous material so that acoustic wave can be transmitted instead of completely reflected as for the case with a rigid back. Since the acoustic field especially the pressure distribution inside the porous material structure is already obtained after the calculation, the transmission coefficient can be derived directly from the ratio of the average pressure at the outbound of the material to the incident pressure, and then the transmission loss versus the frequency can be deduced easily from Eq. (2.49).

3.2.3 Calculation of the band structures

The "Pressure Acoustics Module - Frequency Domain" can no longer be used for the calculation of the band structures as in this module only the $\omega(k)$ -approach is possible, where only the eigenfrequencies can be computed as the eigenvalues of Eq. (3.18). However, for the porous materials used in our work, the equivalent material parameters such as the equivalent dynamic mass density and equivalent bulk modulus are all dependent on the frequency. Thus, only the $k(\omega)$ -approach is applicable and the wave vector is computed as the eigenvalue. For this aim, the PDE module is adopted as it's very convenient for the user to define the partial differential equations, the boundary conditions as well as the desired eigenvalues. The governing equation in the coefficient form in the PDE module for acoustic problems is given by

$$\lambda^2 e_a p - \lambda d_a p + \nabla \cdot \left(-c_a \nabla p - \boldsymbol{\alpha} p + \boldsymbol{\gamma}\right) + \boldsymbol{\beta} \cdot \nabla p + b p = q \,, \tag{3.26}$$

where λ represents the eigenvalue, e_a is the mass coefficient, d_a is the damping or mass coefficient, c_a is the diffusion coefficient, $\boldsymbol{\alpha}$ represents the conservative flux convection coefficient vector, $\boldsymbol{\gamma}$ is the conservative flux source term vector, $\boldsymbol{\beta}$ stands for the convection coefficient vector, b is the absorption coefficient and q stands for the source term. The key point to solving this equation and obtaining the band structures is the determination of the non-zero coefficients. For this aim, the Bloch's theorem introduced in Chapter 2 is substituted in the Helmholtz equation. By considering a 1D case, we obtain

$$-\rho\omega^2 p_k(x) = K\left(\nabla + j\mathbf{k}\right) \cdot \left(\nabla + j\mathbf{k}\right) p_k(x), \tag{3.27}$$

where $p_k(x)$ is a periodic function with

$$p_k(x) = p_k(x + a) \,. \tag{3.28}$$

Comparing Eqs. (3.26) and (3.27), assuming the eigenvalue $\lambda = -j\mathbf{k}$, the non-zero coefficients in Eq. (3.26) are

$$c = K,\ a = -\rho\omega^2,\ \mathrm{e}_a = -K,\ \alpha = K\lambda,\ \beta = -K\lambda, \tag{3.29}$$

where K denotes the bulk modulus of the porous material. By sweeping the frequency ω in the considered range, the corresponding wave vector **k** or complex band structures can be obtained.

3.3 Validation of the computational methods

3.3.1 Validation of the calculation of the sound absorption coefficient

Table 3.1: Material parameters

Material	ϕ_m	$\sigma_m\left(\mathrm{N\cdot s/m^4}\right)$	$\alpha_{\infty m}$	$\Lambda_m\left(\mu\mathrm{m}\right)$	$\Lambda'_m\left(\mu\mathrm{m}\right)$
Green foam	0.99	175000	1	50	142
Rockwool	0.94	135000	2.1	49	166
Melamine foam A	0.99	10000	1	100	200
u160 (recycled foam)	0.90	47700	1.29	24	200

In this section, the TMM and the FEM are used to calculate the sound absorption coefficients of the porous materials and structures. The semi-phenomenological model, the double porosity theory and the porous composite theory introduced in Section 2.2, which are mainly used in this thesis, are first used to evaluate the equivalent dynamic density and equivalent bulk modulus of the structures which are necessary for the application of the TMM. Then the results are compared with existing experimental data [39,41,59] in order to validate the theories as well as the computational methods. The material parameters which are used for the validation are given in Table 3.1 [39,41,59], among which u160 is a foam composed of recycled materials.

First the JCA model is adopted to evaluate the equivalent density as well as the equivalent bulk modulus of a cylindrical porous material made of green foam and Fig. 3.3 shows the comparison between the experimental [41], numerical (FEM) and theoretical results calculated by TMM based on the JCA model. Then the results [39] for the DP rockwool using DP theory is presented in Fig. 3.4, and Fig. 3.5 shows the result [59] for porous composite structure with melamine foam being the inclusion and u160 being the outer matrix. For the sake of simplicity, the results calculated by the TMM combined with the

theoretical models which homogenize the porous materials or structures as an equivalent 1D layer with corresponding thickness are abbreviated as “Theory” in these figures. It can be found in these three figures that good agreements have been obtained which can not only validate the theoretical models employed but also verify the computational methods FEM and TMM.

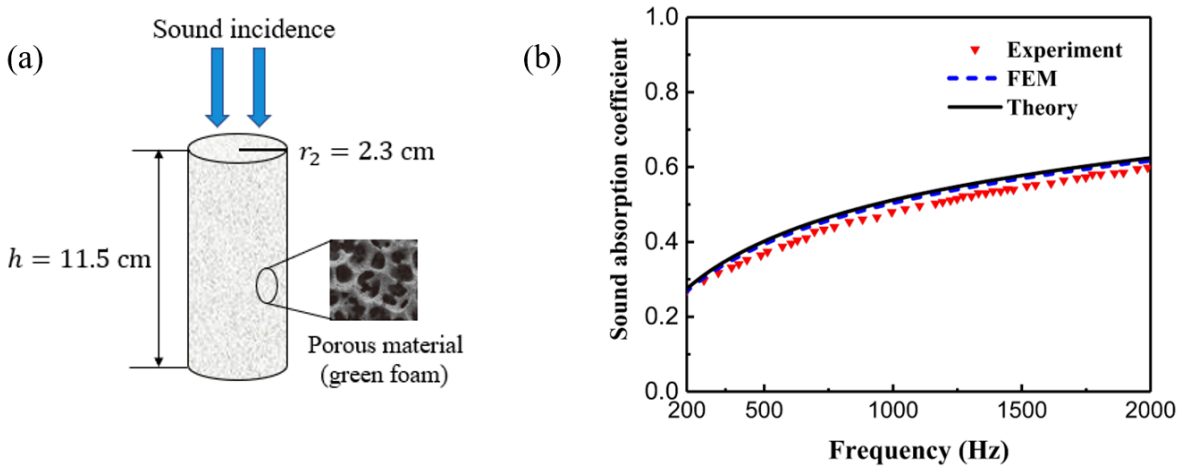

Fig. 3.3: Comparison between experimental, numerical and theoretical results of the sound absorption coefficient for green foam.

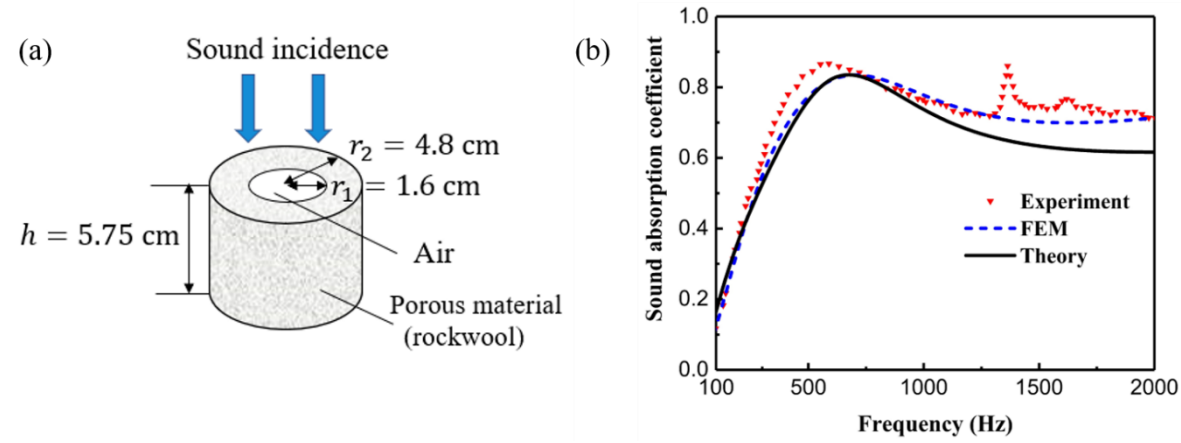

Fig. 3.4: Comparison between experimental, numerical and theoretical results of the sound absorption coefficient for DP rockwool.

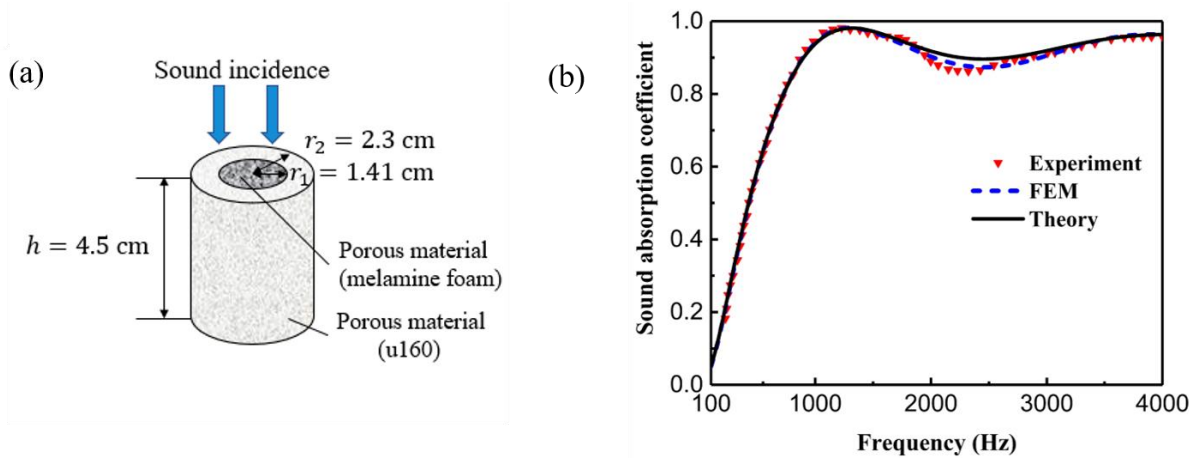

Fig. 3.5: Comparison between experimental, numerical and theoretical results of the sound absorption coefficient for porous composite structure with melamine foam A as the inclusion and u160 as the outer matrix.

3.3.2 Validation of the calculation of the band structures and the transmission spectra

In this section, the calculation of the complex band structures by the FEM is validated through comparison with the transfer matrix method (TMM) solution for 1D metamaterial structure as shown in Fig. 1.6. For the 1D case, the wave vector **k** is reduced to a wave number *k*. Previous research [143] has shown that the dispersion relation between the wave vector and the frequency for a 1D metamaterial structure with two periodically distributed materials shown in Fig. 3.2 calculated by TMM can be simplified to

$$\cos(ka)=\cos(k_1a_1)\cos(k_2a_2)-\frac{1}{2}\left(\frac{\rho_1c_1}{\rho_2c_2}+\frac{\rho_2c_2}{\rho_1c_1}\right)\sin(k_1a_1)\sin(k_2a_2)\,, \tag{3.30}$$

where c_1, c_2 and ρ_1,ρ_2 are the sound velocity and the density of the two materials, respectively, $k_1=2\pi f/c_1$ and $k_2=2\pi f/c_2$ represent the wave number of the two materials, respectively, and $a=a_1+a_2$ denotes the lattice constant. In our calculation $a_1=a_2$=2mm and two material combinations are considered for the validation.

First, two materials namely steel and rubber with constant material properties $\rho_1=7850\text{kg}/\text{m}^3$, c_1=5960m/s and $\rho_2=1300\text{kg}/\text{m}^3$, c_2=96m/s are used. In the PDE module of COMSOL Multiphysics, 1D model is used and two PDEs are defined for the two materials considering their material parameters respectively. For the 1D case with two components, the non-zero coefficients in Eq. (3.26) are

$$c=K_i,\ a=-\rho_i\omega^2,\ \mathrm{e}_a=-K_i,\ \alpha=K_i\lambda,\ \beta=-K_i\lambda\quad i=1,2, \tag{3.31}$$

with $K_i = \rho_i c_i^2$ denoting the bulk modulus of the constituent materials, $\lambda = -jk$ denoting the eigenvalues of Eq. (3.18). At both ends of the structure, the continuous periodic boundary condition is applied. By sweeping the frequency ω in the considered range, the complex band structures can be obtained.

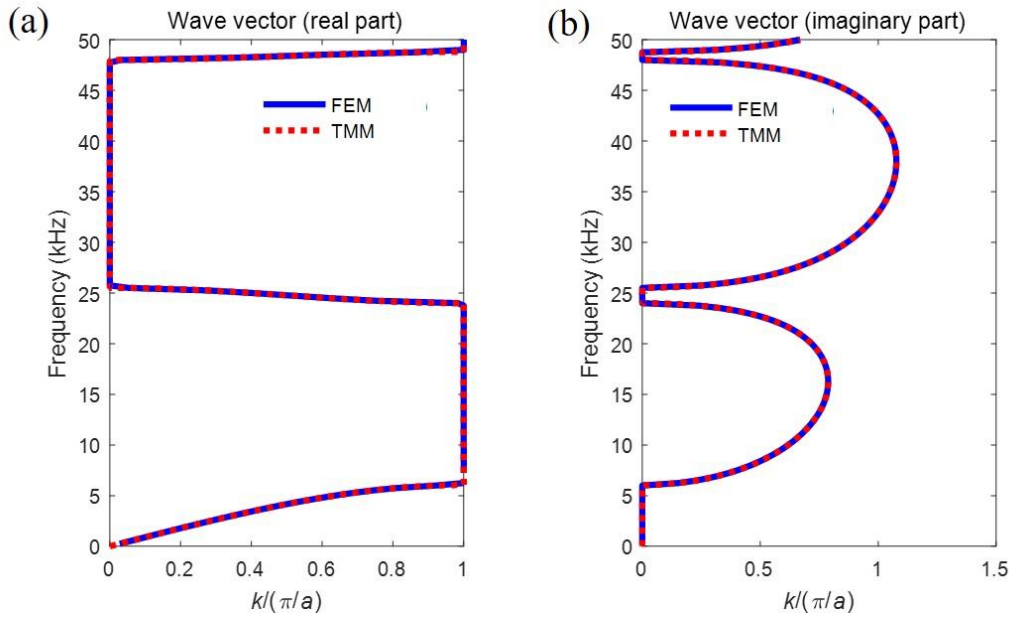

Fig. 3.6: Comparison of the FEM and TMM results for the band structures of a 1D metamaterial structure made of rubber and steel: (a) The real, and (b) the imaginary part of the wave vector.

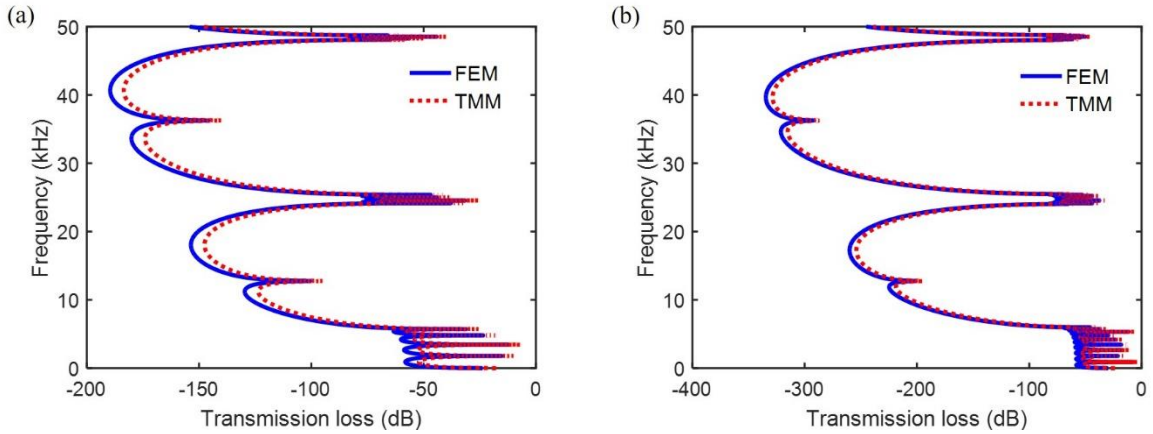

Fig. 3.7: Comparison of the transmission spectra or frequency responses calculated by the FEM and TMM for (a) 5 UCs, and (b) 10 UCs of the 1D metamaterial structure made of rubber and steel.

The comparison of the results obtained by the FEM and TMM is shown in Fig. 3.6. The blue lines represent the FEM results while the red dashed lines represent the TMM results. It can be observed that the fairly good agreements have been achieved as the curves are almost the same, which validates the

FEM and the TMM that we use for calculating the band structures of the metamaterials reciprocally. Besides, the transmission loss is calculated by the FEM (Acoustic module) and the TMM, and the results for 5 UCs and 10 UCs are shown in Figs. 3.7(a) and 3.7(b), respectively. Fairly good agreements have been achieved between the FEM and TMM results and the position of the two troughs corresponds well with the band-gaps where the wave vector is complex and its imaginary part represents the attenuation of the acoustic wave. The more UCs there are, the stronger the attenuation is, which finally leads to a band-gap in which no acoustic wave can pass. Thus, the correctness of using FEM and TMM to obtain the transmission loss is also proved.

Table 3.2: Material parameters

Material	ϕ_m	$\sigma_m\left(\mathrm{N\cdot s/m^4}\right)$	$\alpha_{\infty m}$	$\Lambda_m\left(\mu\mathrm{m}\right)$	$\Lambda'_m\left(\mu\mathrm{m}\right)$
Melamine foam B	0.995	10500	1.0059	240	470

Since for the porous materials, the material parameters are no longer constant and dependent on the frequency, we select another material constitution with rockwool and melamine foam for the validation. The material properties for the rockwool are the same as shown in Table 3.1, while those for another kind of melamine foam are shown in Table 3.2. In this case, the JCA model is adopted to express the time-dependent equivalent bulk modulus in the coefficients presented in Eq. (3.33), which is implemented in the definition of variables. All the other settings remain unchanged and then the band structures can be obtained after parametric sweep calculations.

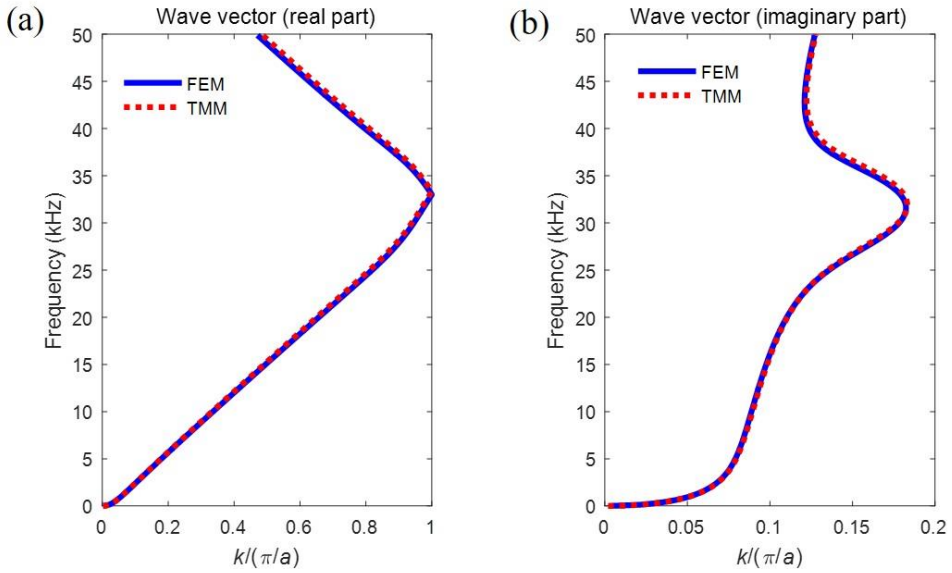

Fig. 3.8: Comparison of the FEM and TMM results for the band structures of a 1D metamaterial made of rockwool and melamine foam: (a) The real, and (b) the imaginary part of the wave vector.

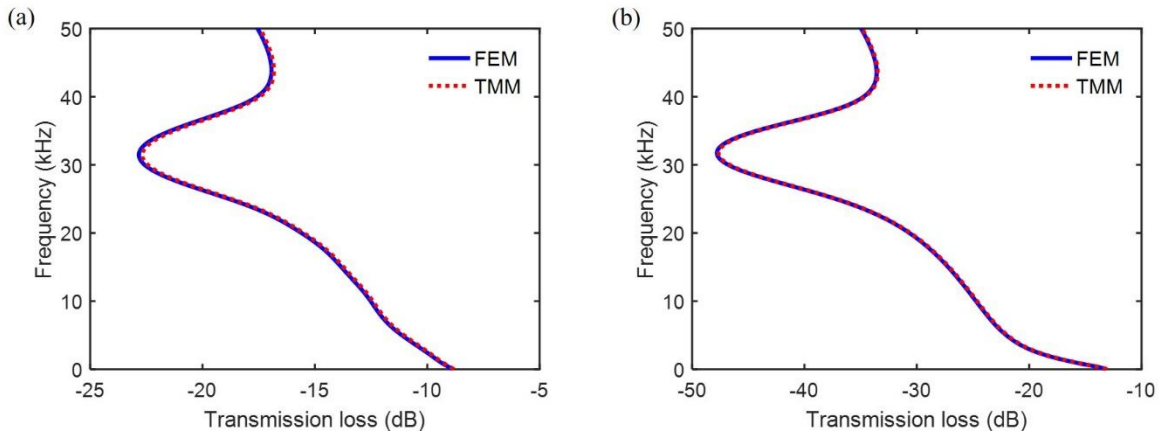

Fig. 3.9: Comparison of the transmission spectra or frequency responses calculated by the FEM and TMM for (a) 5 UCs, and (b) 10 UCs of the 1D metamaterial made of rockwool and melamine foam.

The results for the band structures and the transmission loss are demonstrated in Figs. 3.8 and 3.9, respectively. Again, good consistency has been achieved, which mutually validates the feasibility and accuracy of the two methods for calculating both the band structures and the transmission spectra for 1D PMs. Additionally, based on the results from Figs. 3.7 and 3.9, it can be observed that there is not a significant difference in the shape of the curves obtained when using 5 UCs compared to 10 UCs. The only distinction is that the attenuation is more pronounced for the case with 10 UCs. Since using 5 UCs allows for faster and more time-efficient calculations, we have opted to showcase the results obtained with 5 UCs in subsequent analyses.

3.4 Conclusions

In this chapter, the computational methods which are applied in this thesis are presented. The FEM and TMM are introduced and used to calculate the sound absorption coefficients of various porous materials and structures and the results are compared with the existing experimental results. Fairly good agreements have been achieved, which not only validates the theoretical models presented in Chapter 2, but also proves the correctness of these two computational methods. Besides, the FEM (PDE module) is used to calculate the band structures of a 1D metamaterial structure considering two material selections and the results are compared with those calculated by the TMM. The results obtained using both approaches are in good accordance with each other. The FEM (Acoustics module) is also used to calculate the transmission spectra or frequency responses which are compared with those obtained by the TMM, and their good consistency again validates these two methods reciprocally.

4. Band structure and transmission analysis of porous metamaterial structures

4.1 Introduction

In this chapter, we consider the case of acoustic waves propagating along the periodic direction of a PM. As mentioned in Chapter 2, the Bloch's theorem is used to describe acoustic waves propagating in periodic structures or materials, and the band structures together with the wave transmission analysis are used to investigate the acoustic wave propagation characteristics. As our metamaterial structure is composed of porous materials, the frequency-dependent equivalent dynamic mass density and equivalent bulk modulus deduced from the JCA model are used to describe the material properties, and the band structures of different PM structures are calculated and studied in details based on the computational methods demonstrated in Chapter 3. The material parameters of all the porous materials used in this chapter are listed in Table 4.1 [124,144], and their normalized characteristic impedance curves obtained from the JCA model are shown in Fig. 4.1. To simplify the analysis, in the following study, the common time-harmonic factor $e^{-j\omega t}$ is omitted, where ω denotes the angular frequency of the incident acoustic waves. A frequency range from 1Hz to 50kHz is considered in the analysis.

Table 4.1: Material parameters

Material	ϕ_m	$\sigma_m\left(\mathrm{N\cdot s/m^4}\right)$	$\alpha_{\infty m}$	$\Lambda_m\left(\mu\mathrm{m}\right)$	$\Lambda'_m\left(\mu\mathrm{m}\right)$
Sintered metallic fibres (SMF)	0.9	12057	1.085	141	225
Aluminuim foam	0.66	3190	1.7	223	544
Glasswool	0.999	15957	1	97	530

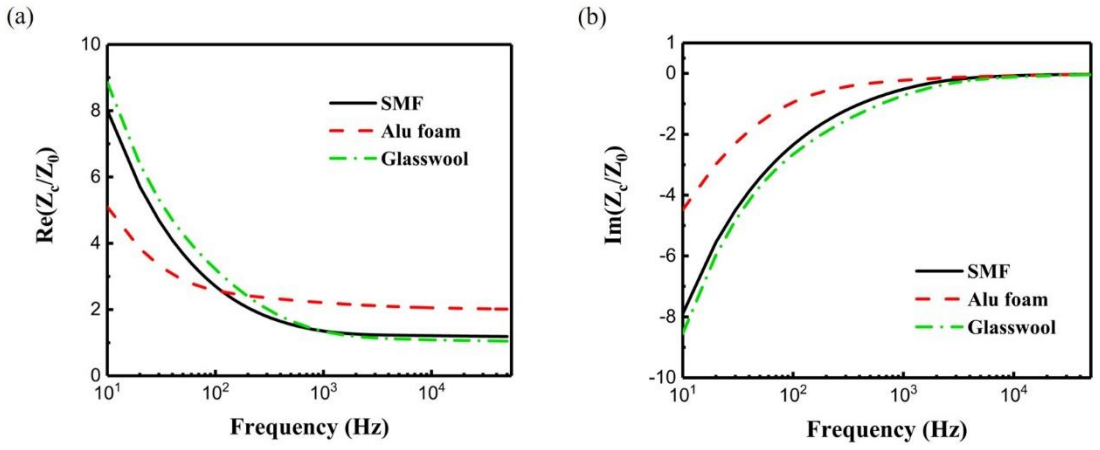

Fig. 4.1: (a) Real part and (b) imaginary part of the normalized characteristic impedance of the porous materials versus frequency.

4.2 Slit-perforated porous metamaterial structure

4.2.1 Problem formulation

The slit-perforated porous metamaterial (SPM) structure consists of periodically distributed porous material matrix and slits and the acoustic waves propagate along the direction of the periodicity as presented in Fig. 4.2(a). As the sound incidence is perpendicular to the structure, the infinite structure can be simplified to a 1D metamaterial structure with two components as shown in Fig. 4.2(b). Due to the periodicity of the structure, a unit-cell with lattice constant $a=a_1+a_2$ as marked by the red dashed line is considered.

The detailed process of calculating the band structures using the FEM has been thoroughly explained in Chapter 3, so there is no need to reiterate it here. The main difference lies in substituting the parameters of the second porous material with those of air. For the calculation of the band structures and the transmission spectra by TMM, the total transfer matrix for one UC with two layers can be written as $\mathbf{T}_2 = \mathbf{t}_1\mathbf{t}_{air}$, and the wave number and the characteristic impedance of the porous material and air are applied in $\mathbf{t}_1$ and $\mathbf{t}_{air}$ respectively.

As for the calculation of the transmission spectra of the SPM structure by the FEM, the schematic representation of the model with 5 UCs is shown in Fig. 4.2(c). The "Pressure Acoustics Module-Frequency Domain" is used and a 2D model is established. The porous material is defined as the "Poroacoustics domain" described by the JCA model and the slit is defined as "Air domain". In order to generate the incident plane acoustic waves, a background pressure field is introduced as the air domain. A perfectly matched layer (PML) is defined at the left side of the background pressure field to avoid acoustic wave reflections. The acoustic or sound waves can pass through the structure and come out from the right side outbound of the SPM structure and two modelling ways can be adopted to realize the procedure: the first way is to add an air domain which is backed by another PML layer, and the second approach is to match the impedance of the outbound boundary with that of air. The second way is employed in our calculation as it's simpler and fewer meshes are needed which can decrease the computational time and improve the efficiency. Periodic boundary conditions are applied to the upper and lower boundaries of the model to avoid the effect of the height of the structure. Free triangular meshes are utilized for all the computational domains except the PML where the mapped meshes are used. In order to obtain sufficient accuracy, the sizes of all the meshes are defined to be smaller than one-tenth of the minimum wave length in the structure, which is calculated by the ratio of the sound velocity to the frequency.

The transmission coefficient is calculated by $T = \langle p_{out} \rangle / \langle p_{inc} \rangle$, where $\langle p_{out} \rangle$ represents the average values of the sound pressure at the outbound of the structure and $\langle p_{in} \rangle$ represents the given incident

pressure. Thus, the transmission loss can be deduced by Eq. (2.49).

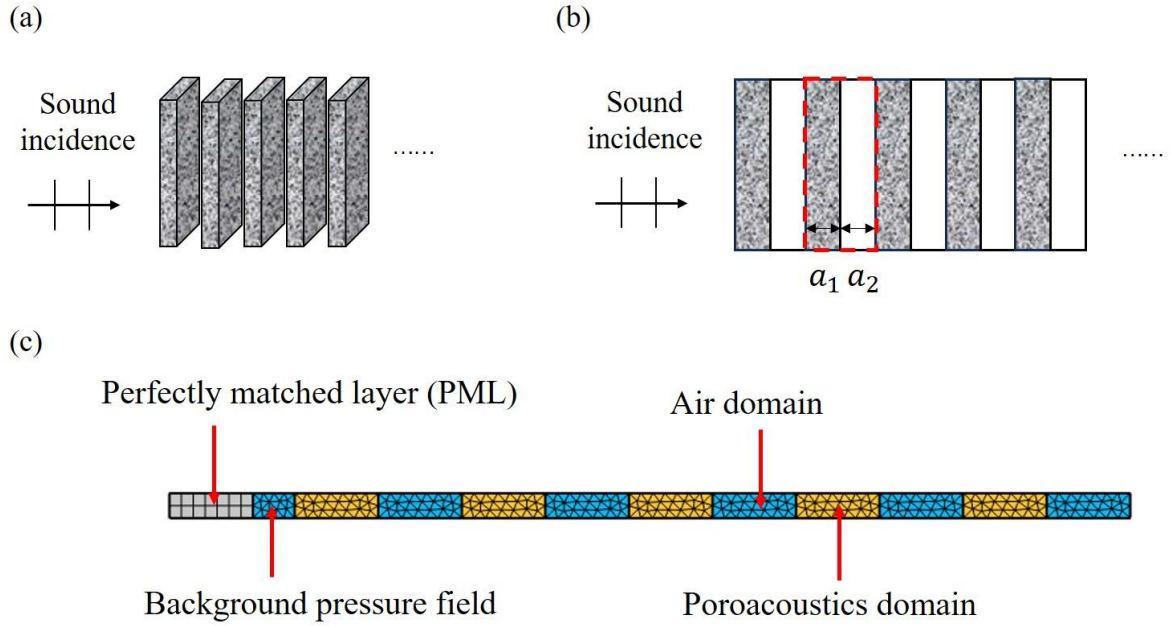

Fig. 4.2: (a) Schematic representation of acoustic wave propagation in the slit-perforated porous metamaterial (SPM) structure, (b) simplified 1D problem, (c) FE model of the structure with 5 UCs for the wave transmission analysis.

4.2.2 Results and discussions

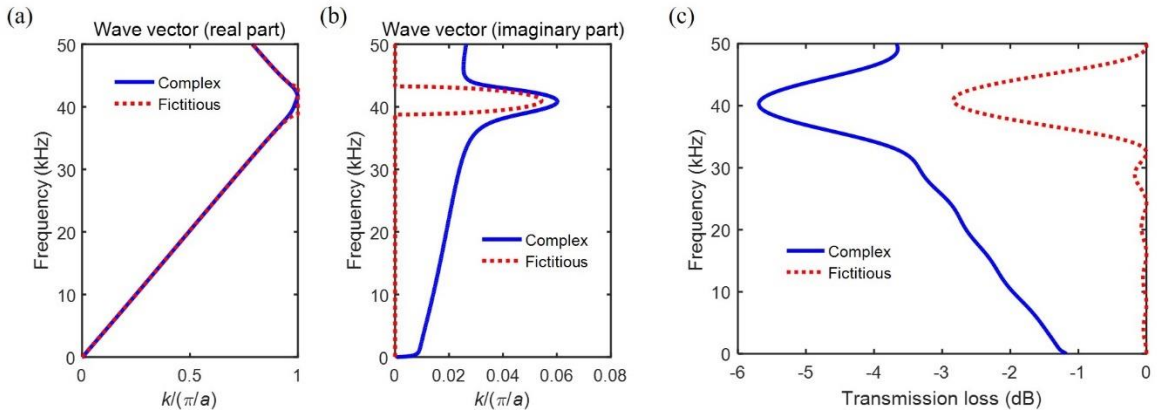

Fig. 4.3: (a) Real part and (b) imaginary part of the band structures, and (c) transmission spectra considering 5 UCs for the SPM structure composed of the SMF and air calculated by the TMM.

We first consider the SPM structure consists of aluminium foam and air and the geometry is defined as $a_1 = a_2 = 2$mm. Since the FEM and TMM for calculating the band structures and the transmission spectra are already validated in the previous chapter, here only the results obtained by the TMM are presented.

Fig. 4.3 shows the band structures and the transmission spectra considering 5 UCs of the SPM structure composed of the SMF and air while those for the SPM structure composed of aluminium foam and air are shown in Fig. 4.4. The case with only the real part of the equivalent material properties (dynamic mass density and bulk modulus) is also plotted for comparison and it is named as "Fictitious" in the following figures.

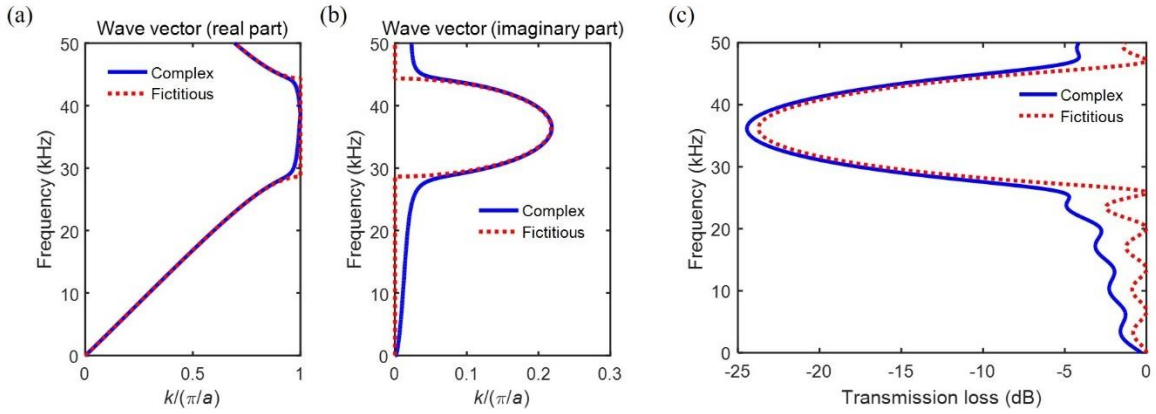

Fig. 4.4: (a) Real part and (b) imaginary part of the band structures, and (c) transmission spectra considering 5 UCs for the SPM structure composed of the aluminium foam and air calculated by the TMM.

First it can be observed that there is a slight difference between the results obtained considering the complex material properties and those obtained considering the fictitious ones. The introduction of the imaginary part of the material properties will not only change the imaginary part of the band structure, but also alter the real part. To be more specific, the corners of the starting and ending point of the real part of the bandgap of the band structures are smoothened. This phenomenon can be roughly explained by the related theory of photonic crystals [145,146] as presented in previous literatures [147]. Let us have a look at the real vector of the band structures near the bandgap when there is no attenuation which means the material properties are real. If we approximate the lower boundary of the bandgap by expanding $\omega(k)$ near the high-symmetry points $k_0 = 0$ and $k_0 = \pi / a$ in a series of the complex k using the Taylor expansion, no odd powers of k will be included in the series based on the time-reversal symmetry. Therefore, for the lowest order we have

$$\Delta\omega = \omega(k) - \omega(k_0) \approx \varsigma\left(k - k_0\right)^2 = \varsigma\left(\Delta k\right)^2 = \varsigma\left(e + gj\right)^2 \tag{4.1}$$

where ς is a constant related to the curvature or second derivative of the band structures. When no imaginary part exists in the material properties, and if a certain frequency is slightly higher than the lower boundary of the bandgap, then $\Delta\omega > 0$ and Δk should be a pure imaginary number $\left(e = 0, g \neq 0\right)$. However, when the imaginary part exists, for the same $\Delta\omega > 0$, g will either increase

or decrease. According to Eq. (4.1), in order to make $\Delta\omega > 0$ valid, f must be non-zero. Thus, the real part of the wave vector within the first Brillouin zone will either decrease or increase, resulting in the bands near the high-symmetry points becoming smoother.

Besides, it can be observed that the transmission spectra correspond well with the imaginary part of the wave vector of the band structures for both cases, as both of these two figures characterize the attenuation of the acoustic waves propagating in the SPM structure.

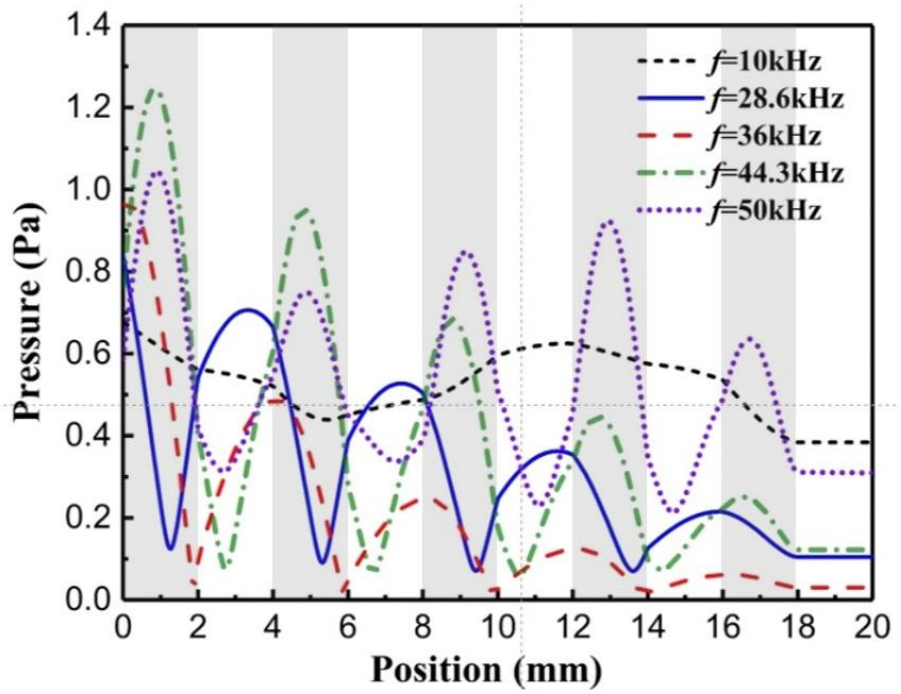

Fig. 4.5: Pressure distribution (Unit: Pa) for the SPM structure composed of aluminium foam and air calculated by the FEM at different frequencies.

However, in previous works, for the complex band structures the bandgap is defined as the frequency range within which the imaginary part of all wave vectors is non-zero, where only the evanescent waves exist [148]. Nevertheless, this criterion is no longer applicable for the PM structures since both the equivalent dynamic mass density and the equivalent bulk modulus are complex, which leads to a complex wave vector as attenuation always occurs regardless of the frequency. Therefore, the pressure distribution inside the SPM structure composed of aluminium foam and air with 5 UCs are also plotted here to help determine the bandgap. Five different frequencies are chosen:10kHz, 28.6kHz, 36kHz, 44.3kHz and 50kHz, among which 28.6kHz and 44.3kHz are the starting and ending point of the bandgap obtained considering the fictitious material properties. Significant variations are noticed between the pressure distribution among these five cases. At 10kHz and 50kHz, it is apparent that the acoustic waves can propagate through the structure, thus they do not belong to the bandgap range. But due to the existence of the pores where dissipation takes place, the acoustic waves attenuate. At the right

end of the structure consisting of 5 UCs, the pressure is approximately around 0.4Pa. On the contrary, at 28.6kHz and 44.3kHz, this value is about 0.1Pa and at 36kHz where the imaginary part of the wave vector is the largest, the pressure is reduced to almost 0. In summary, a very wide gap is formed from about 28.6kHz to 44.3kHz for the SPM structure consists of aluminum foam and air. For the metamaterial structures composed of conventional materials, sound waves are not able to propagate within the bandgap, while waves in other frequency ranges can pass through. However, for PM structures, attenuation also exhibits outside the bandgap, which is obviously an advantage. Similarly, the bandgap can be identified as from 38.7kHz to 43.2kHz for the SPM structure consists of SMF and air as shown in Fig. 4.3. The bandgap is much narrower than that of the SPM structure consists of aluminum foam and air, which is due to the effect of the impedance ratio. As presented in Fig. 4.1, at high frequency range, the impedance ratio between aluminum foam and air is much larger than that for SPM, which is more conducive to the formation of a band gap as proved by previous research works [149].

Then in the following the influence of the geometric parameters on the band structures of the SPM structure is studied. We use the material composition of aluminium foam and air as an example and first consider the case of either keeping a_2=2mm or a_1=2mm unchanged and varying the other. Four different cases are evaluated and the results are shown in Fig. 4.6.

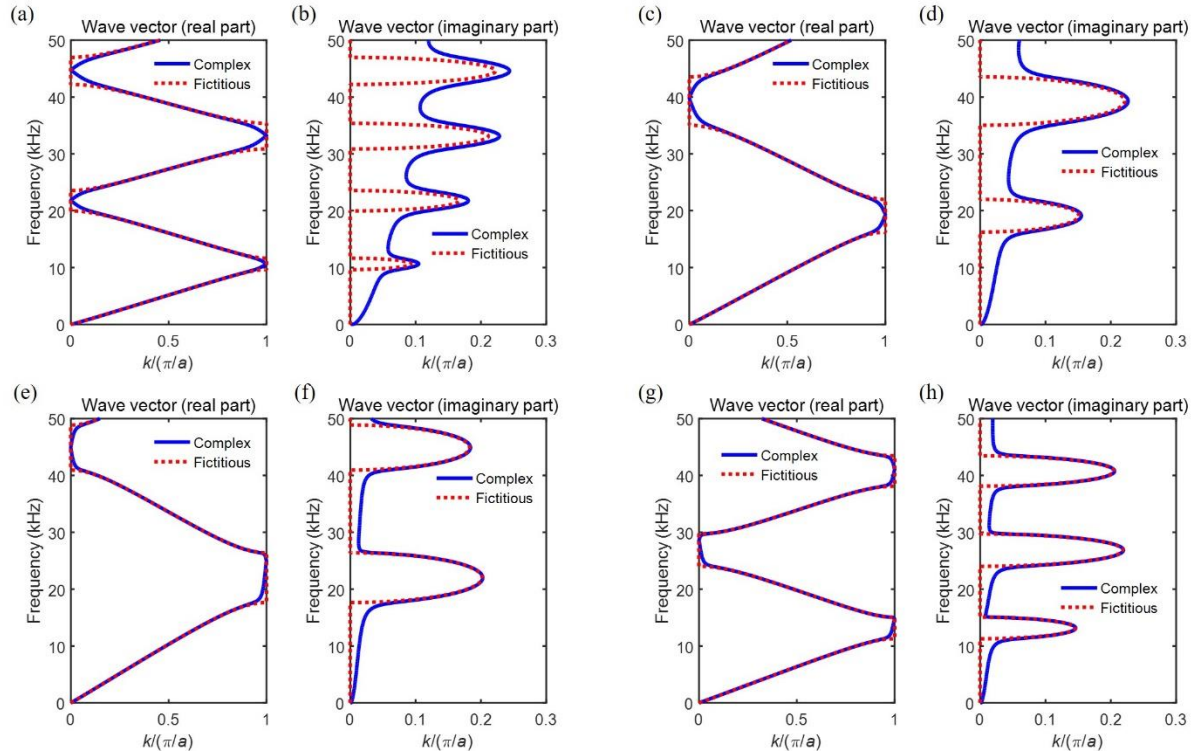

Fig. 4.6: Real and imaginary parts of the band structures for the SPM structure consisting of the aluminium foam and air calculated by the TMM (a) and (b) a_1=10mm, a_2=2mm, (c) and (d) a_1=5mm, a_2=2mm, (e) and (f) a_1=2mm, a_2=5mm, (g) and (h) a_1=2mm, a_2=10mm.

Compared with the results shown in Fig. 4.4 with equal width of the two constituent porous materials, it can be seen that having different widths for the two components will result in more band gaps and the first bandgap will move to a lower frequency range. Besides, the greater the difference, the more the bandgaps. However, the bandgap is the widest when a_1= a_2=2mm. From Figs. 4.4 and 4.6 (a)-(d), it is observed that with the increase of a_1, the smoothing effect of the real part of the wave vector near the boundary of the bandgap becomes more obvious. It is logical and explainable according to Eq. (4.1) as a larger imaginary part will cause the real part of the wave vector to decrease or increase to a greater extent to satisfy the equation. Besides, the imaginary part of the wave vector out of the bandgap range gets bigger evidently as $a_1$increases, which is due to the fact that more attenuation is brought in with more porous materials. If a_1 remains unchanged, comparing Figs. 4.4 and 4.6(e)-(h), we can see that the smoothing effect and the attenuation impact are almost the same, while a larger a_2 will give rise to the generation of more bandgaps.

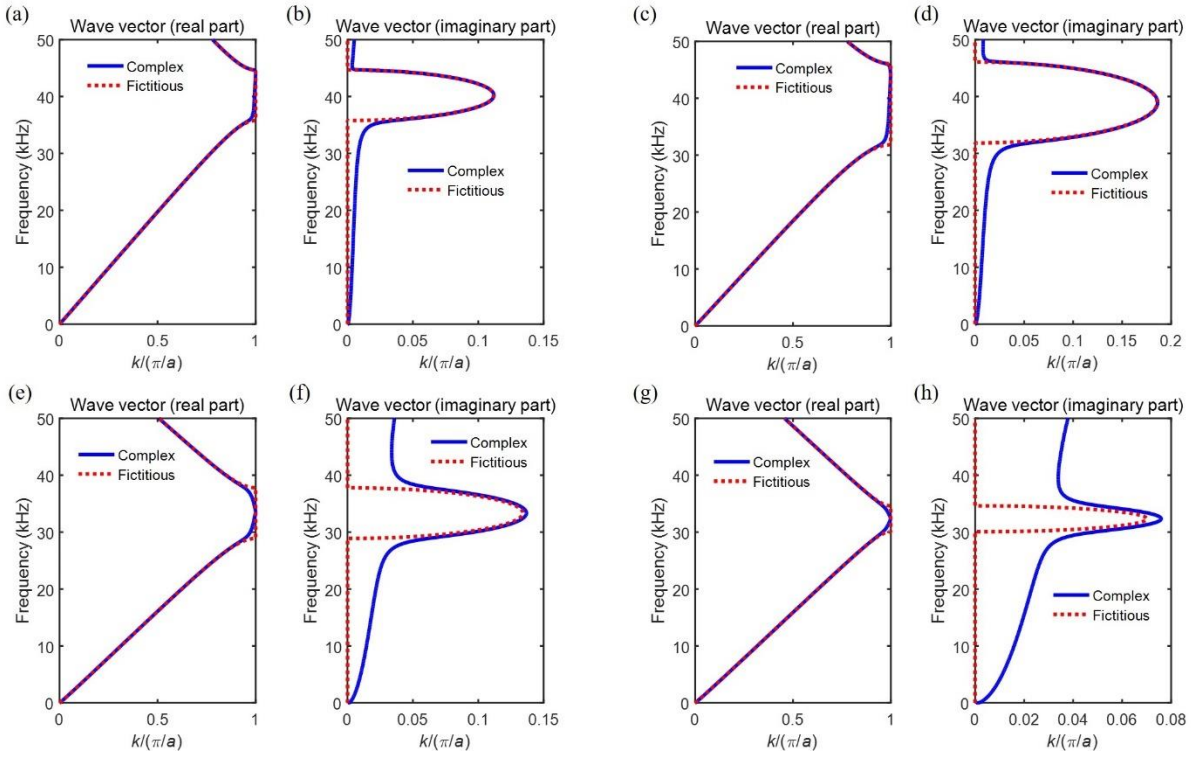

Fig. 4.7: Real and imaginary parts of the band structure for the SPM structure consists of the aluminium foam and air calculated by the TMM (a) and (b) a_1=0.5mm, a_2=3.5mm, (c) and (d) a_1=1mm, a_2=3mm, (e) and (f) a_1=3mm, a_2=1mm, (g) and (h) a_1=3.5mm, a_2=0.5mm.

Then the influence of the material composition ratio is studied. The size of the UC a=4mm is kept unchanged and we vary the values of a_1 and a_2, and the results for the band structures are presented in Fig. 4.7. By comparing Figs. 4.3 and 4.7, we found that when a_1=a_2, the bandgap is the widest and the starting point is lowest. It is also evident that with the increase of the proportion of the porous material,

the smoothing effect of the real part of the band structures becomes more noticeable. Meanwhile, the increase in the imaginary part of the wave vector outside the bandgap range also becomes more obvious, which signifies that the attenuation is more apparent.

4.3 Porous composite metamaterial structure

4.3.1 Problem formulation

In this subsection, we consider the acoustic wave propagation in the porous composite metamaterial (PCM) structure as shown in Fig. 4.8(a). The structure consists of two different periodically distributed porous materials and a plane time-harmonic acoustic wave is normally incident onto the structure. It can be simplified to a 1D metamaterial structure with two components with width a_1 and a_2 respectively, as shown in Fig. 4.8(b). The UC is marked by the red dashed line as presented in Fig. 4.8(b) and the lattice constant $a=a_1+a_2$.

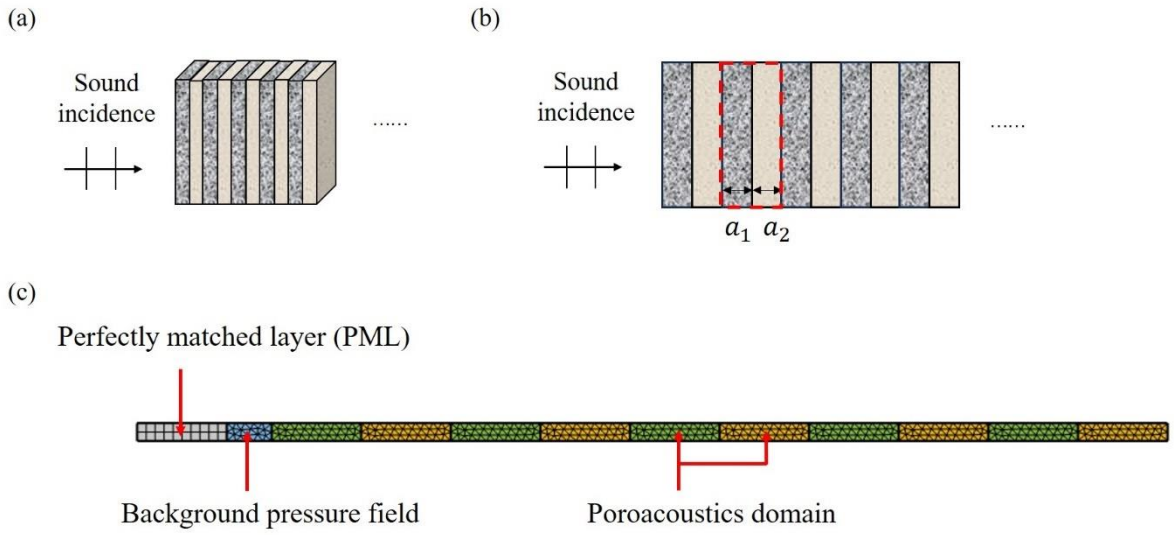

Fig. 4.8: (a) Schematic representation of acoustic wave propagation in the porous composite metamaterial (PCM) structure, (b) simplified 1D problem, (c) FE model of the structure with 5 UCs for the wave transmission analysis.

The detailed process of calculating the bandgaps of such structure using the FEM (PDE module) has been explained in detail in Chapter 3, so it is omitted here. As for the solution by the TMM, the transfer matrix for each material is obtained by Eq. (3.3) considering the two porous material parameters obtained by the JCA model respectively and $d_i=a_i$, i=1, 2. Then the total transfer matrix for one UC can be written as $\mathbf{T}_2 = \mathbf{t}_1\mathbf{t}_2$, and the eigenvalue equation Eq. (3.17) can be solved which gives the result for

the band structures. The same total transfer matrix is also used to calculate the transmission coefficient shown in Eq. (3.8) and then the transmission loss is deduced by Eq. (2.49). For the calculation of the transmission spectra of the PCM structure, similar process as detailed in subsection 4.2.1 is applied, except that the only difference lies in the modelling of the second porous material as poroacoustics domain instead of air domain. Then, the transmission spectra can be calculated without difficulties.

4.3.2 Results and discussions

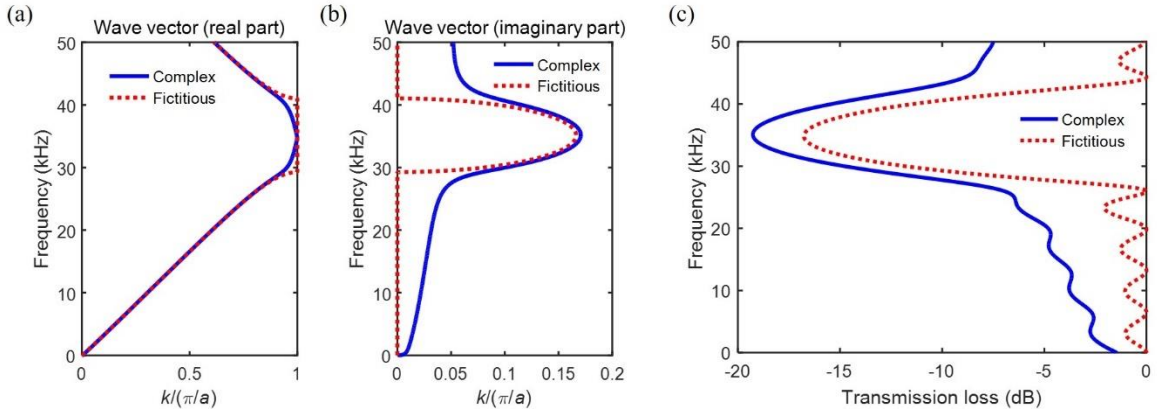

Fig. 4.9: (a) Real part and (b) imaginary part of the band structures, and (c) transmission spectra considering 5 UCs for the PCM structure composed of the SMF and the aluminium foam calculated by the TMM.

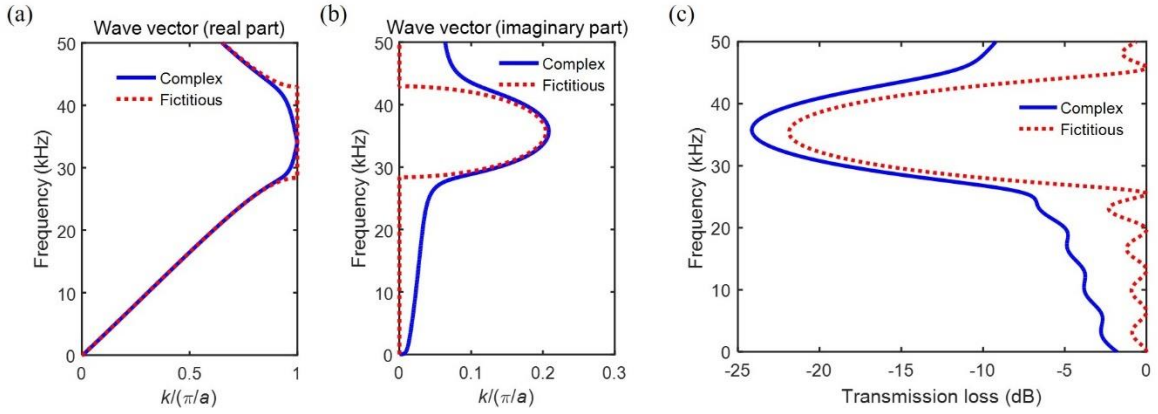

Fig. 4.10: (a) Real part and (b) imaginary part of the band structures, and (c) transmission spectra considering 5 UCs for the PCM structure composed of aluminium foam and glasswool calculated by the TMM.

First, the PCM structure with two porous materials of equal width a_1=a_2=2mm is considered, and two material constitutions are used. The corresponding results for the band structures and the transmission spectra considering 5 UCs of the SPM structure are shown in Figs. 4.9 and 4.10, respectively. Same in the previous case, the red dotted curves named “Fictitious” representing the case with only the real part

of the equivalent material properties (dynamic mass density and bulk modulus) are also plotted for comparison and the determination of the bandgap range.

Comparing Fig. 4.9 with Fig. 4.3, and Fig. 4.10 with Fig. 4.4, it can be observed that the introduction of a second porous material into the structure will lead to an enhanced smoothing effect of the real part of the wave vector at the bandgap boundaries. Besides, the bandgap ranges are changed due to the addition of the second porous material. For the PCM structure composed of SMF and aluminium foam, the bandgap ranges from about 29.2kHz to 41kHz while that for the PCM structure consists of aluminium foam and glasswool spans from about 28.3kHz to 42.9kHz. For both cases, in contrast to the SPM structure composed of one porous material and air, both the starting and ending frequencies of the bandgap shift towards lower frequencies. In other words, replacing air with porous material is beneficial to obtain a bandgap at lower frequencies.

Besides, it can be observed that the transmission spectra correspond well with the imaginary part of the wave vector of the band structures for both cases, which characterizes the attenuation of the acoustic waves inside the structure. In order to show the wave attenuation in the structure more intuitively, the pressure distribution inside the PCM structure composed of aluminium foam and glasswool with 5 UCs are also plotted in Fig. 4.11. Five different frequencies are chosen:15kHz, 28.3kHz, 35kHz, 42.9kHz and 50kHz, among which 28.3kHz and 42.9kHz are the starting and ending points of the bandgap obtained considering the fictitious material properties. It is evident that within the bandgap, the attenuation is much stronger. At f=35kHz which is the frequency where the imaginary part of the wave vector is the largest, almost no acoustic waves can pass after 3 UCs.

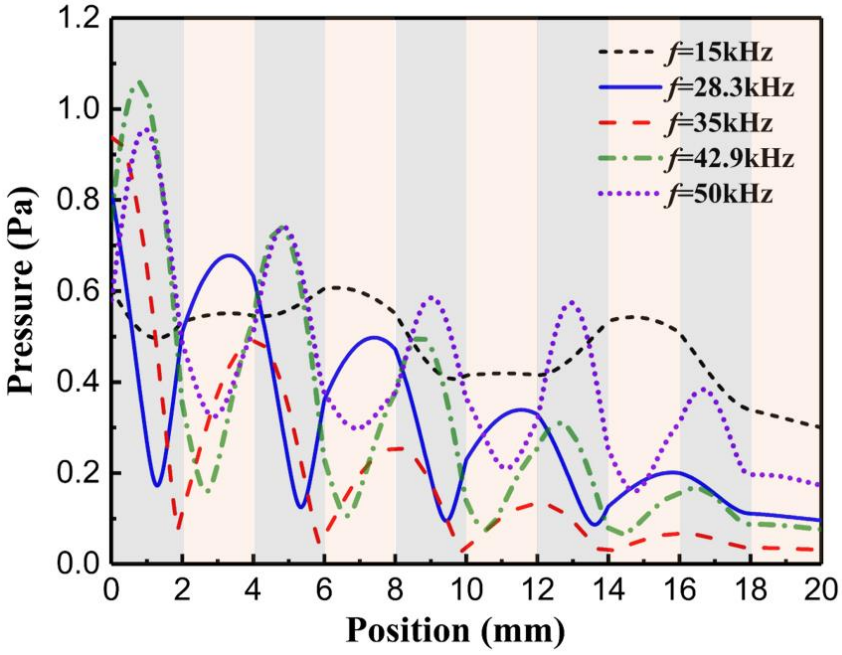

Fig. 4.11: Pressure distribution (Unit: Pa) for the SPM structure composed of the aluminium foam and glasswool calculated by the FEM at different frequencies.

Then in the following, the effects of the geometric parameters on the band structures of the PCM structure are investigated. We use the material composition of aluminium foam and glasswool as an example and first consider the case of either keeping a_2=2mm or a_1=2mm unchanged and varying the other. The band structures can better exhibit the acoustic wave propagation properties in the structure with infinite UCs. Thus, for the parametrical analysis only the band structures are demonstrated. The same geometric parameters as in Fig. 4.6 are chosen and the results are shown in Fig. 4.12. Compared with Fig. 4.10, it can be observed that with the increase of the size difference between the two materials, more bandgaps are generated. Furthermore, the position of the first bandgap gradually moves to a lower frequency. However, when the size of both porous materials is 2 mm, the resulting bandgap is the widest. For all these five cases, the smoothing effect of the real part of the wave vector is always apparent.

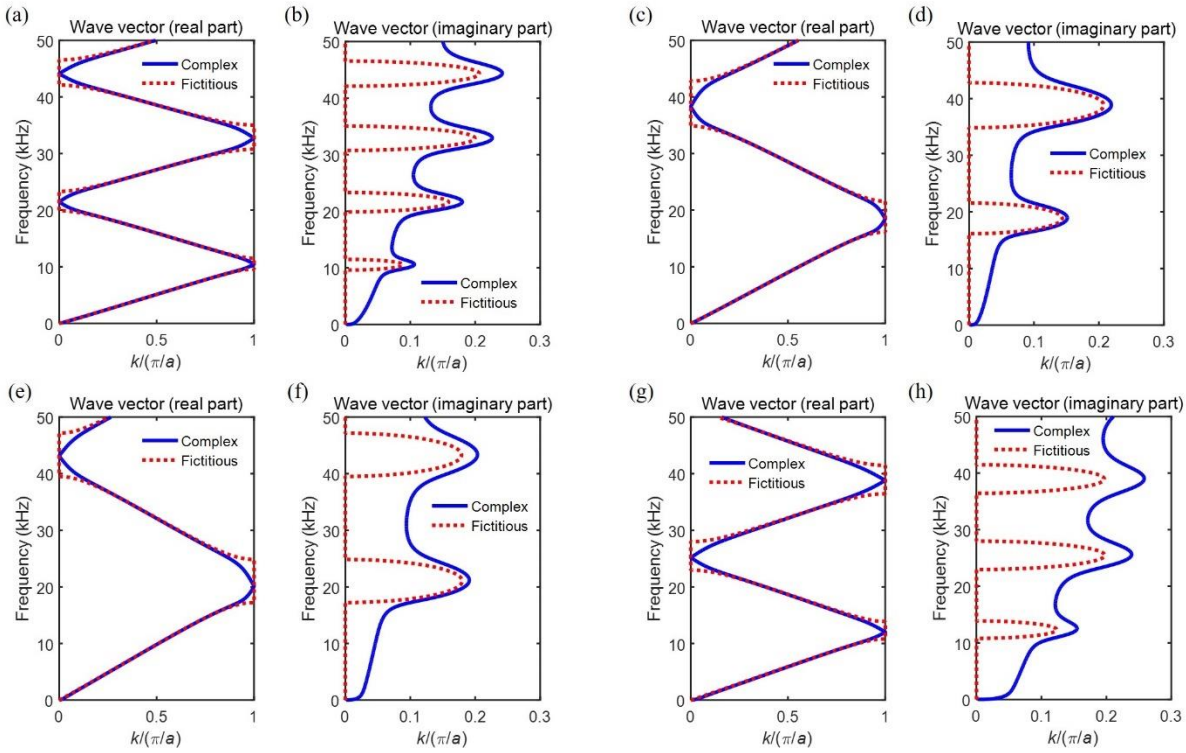

Fig. 4.12: Real and imaginary parts of the band structure for the PCM structure consists of the aluminium foam and glasswool calculated by TMM: (a) and (b) a_1=10mm, a_2=2mm, (c) and (d) a_1=5mm, a_2=2mm, (e) and (f) a_1=2mm, a_2=5mm, (g) and (h) a_1=2mm, a_2=10mm.

By comparing Figs.4.6 and 4.12, it can be observed that under the same dimensions, replacing air with glasswool does not lead to a significant change in the position of the bandgap. Yet, comparing Figs.4.6 (e)-(h) to 4.12(e)-(h), it can be found that replacing air with glasswool and gradually increasing its dimension result in a significant increase in the imaginary part of the wave vector outside the bandgap. On the contrary, this phenomenon is not observable when increasing the dimension of the aluminium

foam. In other words, it can be concluded that the aluminium foam contributes to the generation of the bandgap, while the glasswool contributes more to the attenuation especially outside the bandgap range.

Then the influence of the material composition ratio is studied. The size of the UC a=4mm is kept unchanged and we vary the values of a_1 and a_2 simultaneously. The same geometric parameters as used in Fig. 4.7 are chosen and the results for the band structures of the PCM structure composed of aluminum foam and glasswool are presented in Fig. 4.13. By comparing Figs. 4.10 and 4.13, it can be seen that the band structures are greatly affected by the ratio of the widths of the two constituent porous materials. Still, the widest bandgap is generated when a_1=a_2=2mm and the attenuation effect of the glasswool is evident.

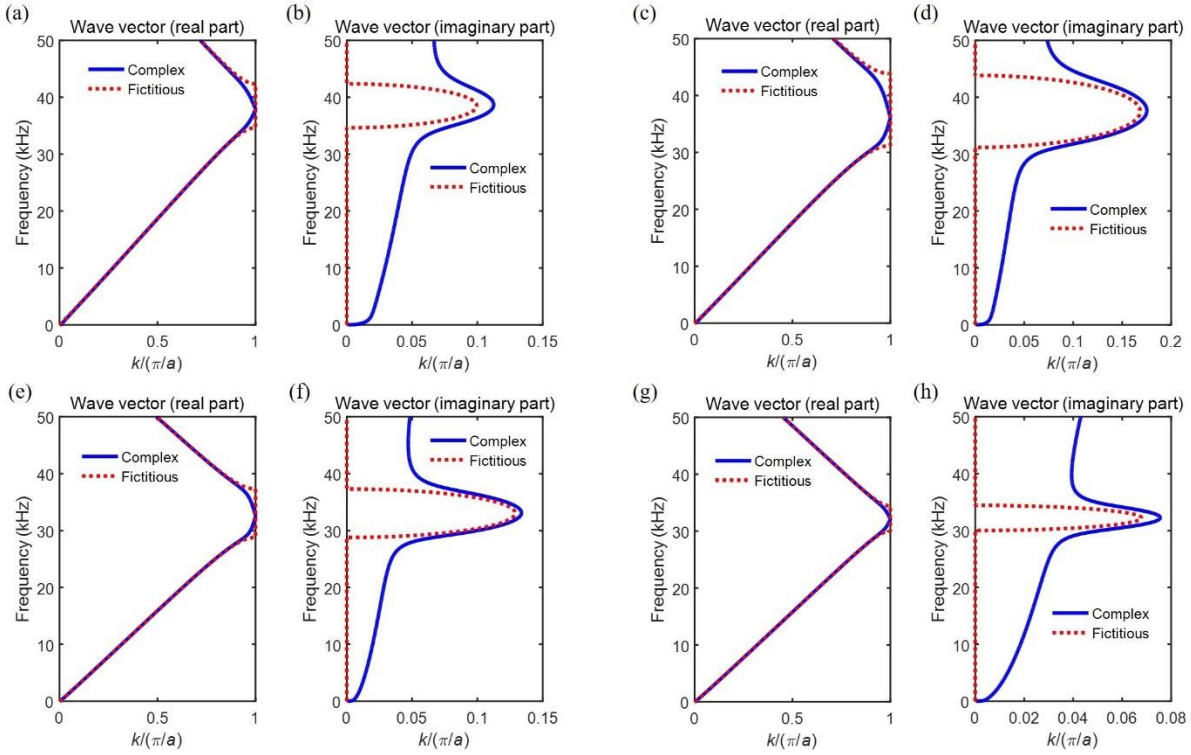

Fig. 4.13: Real and imaginary parts of the band structure for the PCM structure consists of the aluminium foam and glasswool calculated by TMM: (a) and (b) a_1=0.5mm, a_2=3.5mm, (c) and (d) a_1=1mm, a_2=3mm, (e) and (f) a_1=3mm, a_2=1mm, (g) and (h) a_1=3.5mm, a_2=0.5mm.

4.4 Slit-perforated multi-layered porous metamaterial structure

4.4.1 Problem formulation

In this section, the acoustic wave propagation in the slit-perforated multi-layered porous metamaterial (SMPM) structure as shown in Fig. 4.14(a) is studied. Both the slits and the two porous materials are combined in this structure and the same assumptions as previously explained for the geometry are

applied and the lattice constant $a=2a_1+2a_2+w$ is defined for the metamaterial structure shown in Fig. 4.14(b). Due to the periodicity of the structure, the choice of the UC can be either the four-layer structure marked with the red dashed lines or the five-layer structure marked with the green dashed lines. We have already verified that the results obtained from these two methods are the same, but we won't go into details here. Due to its symmetry, we use the five-layer UC as an example and the corresponding FE model used for calculating the transmission spectra is shown in Fig. 4.14(c). The definition for each field of the SMPM structure is similar to that for the SPM and PCM structures and the transmission loss can be easily calculated. As for the TMM, the transfer matrix for each material is obtained by Eq. (3.3) considering the two porous material parameters obtained by the JCA model respectively and $d_i=a_i$, i=1, 2, and for the determination of the transfer matrix for the slit the air properties are used with $d_{air}=w$. Then the total transfer matrix can be written as $\mathbf{T}_5=\mathbf{t}_2\mathbf{t}_1\mathbf{t}_{air}\mathbf{t}_1\mathbf{t}_2$, and the transmission coefficient is obtained by Eqs. (3.4) and (3.8) and then the transmission loss is further deduced by Eq. (2.49). To obtain the band structures by the TMM, the total transfer matrix $\mathbf{T}_5$ for one UC used to solve the eigenvalue equation Eq. (3.17) is the same as that for the calculation of the transmission spectra. The detailed procedure to compute the band structures by the PDE Module can be referred to Chapter 3, thus it is omitted here for the sake of brevity.

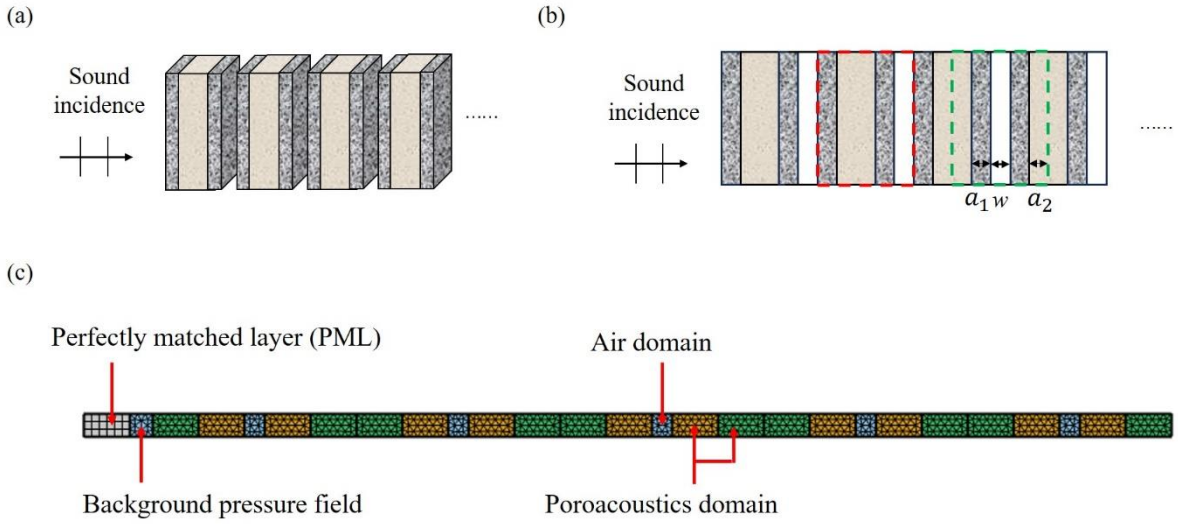

Fig. 4.14: (a) Schematic representation of acoustic wave propagation in the slit-perforated multi-layered porous metamaterial (SMPM) structure, (b) simplified 1D problem, and (c) FE model of the structure with 5 UCs for the wave transmission analysis.

Table 4.2: Material layout of the considered cases

Case	Porous material 1	Porous material 2
1	Glasswool	Aluminium foam
2	Aluminium foam	Glasswool
3	Aluminium foam	SMF
4	SMF	Aluminium foam

4.4.2 Results and discussions

We first consider the case with the geometrical parameters a_1=a_2=w=2mm. Unlike the SPM and the PCM structure, the layout or the order of the materials is also important for the SMPM structure, and the material composition Case 1 as shown in Table 4.2 is first used for the calculation. The band structure results considering both complex and fictitious material properties obtained by the TMM and the PDE Module of COMSOL Multiphysics are presented in Fig. 4.15, and good consistency has been achieved.

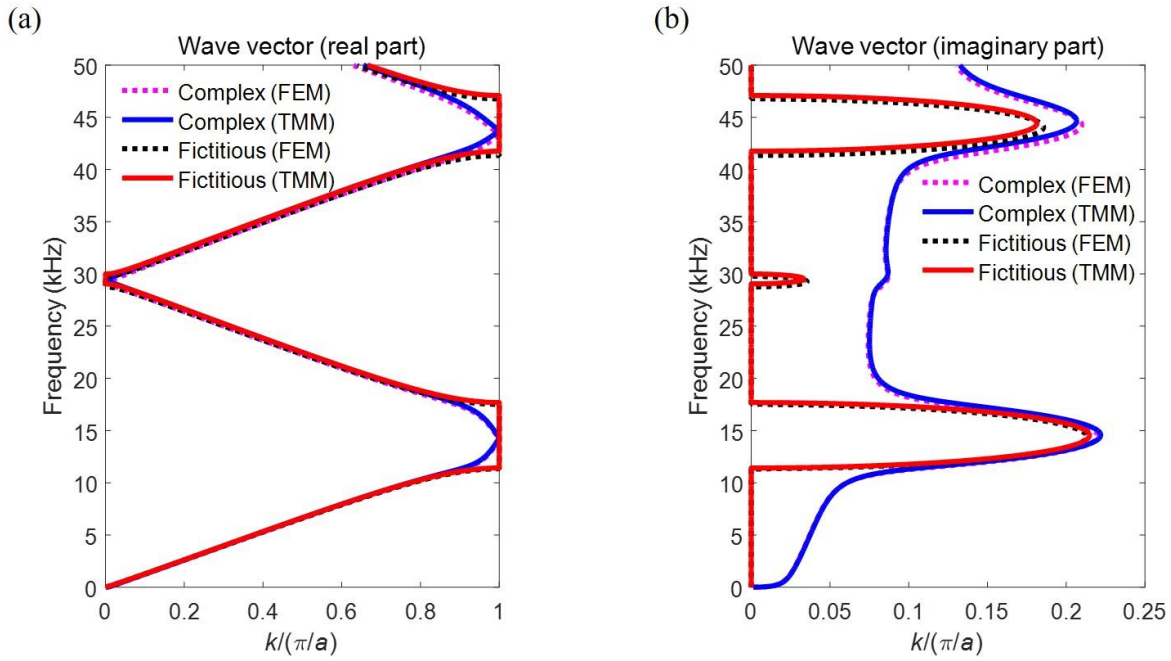

Fig. 4.15: Comparison of the band structures for the SMPM structure calculated by the FEM and TMM for Case 1. (a) Real part and (b) imaginary part.

Fig. 4.16 and Fig. 4.17 demonstrate the band structure results for all the four cases listed in Table 4.2, and the geometric parameters are defined as a_1=a_2=1mm, w=2mm so that in one UC, the proportions of each component are the same. It can be seen in both figures that the arrangement of the porous material

in the SMPM structure has a significant impact on the band structure. More specifically, using aluminium foam as porous material 2 and the other one as porous material 1 is favorable to obtain a wide bandgap at lower frequency range compared to the inverse arrangement. When aluminium foam is used as porous material 2, a bandgap from about 20kHz to 30kHz can be formed, otherwise the starting point of the bandgap will rise to about 40kHz. Besides, comparing the results of all the four considered cases, it can be concluded that aluminum foam is the key to creating the bandgap and determining its location, regardless of the other constituent material.

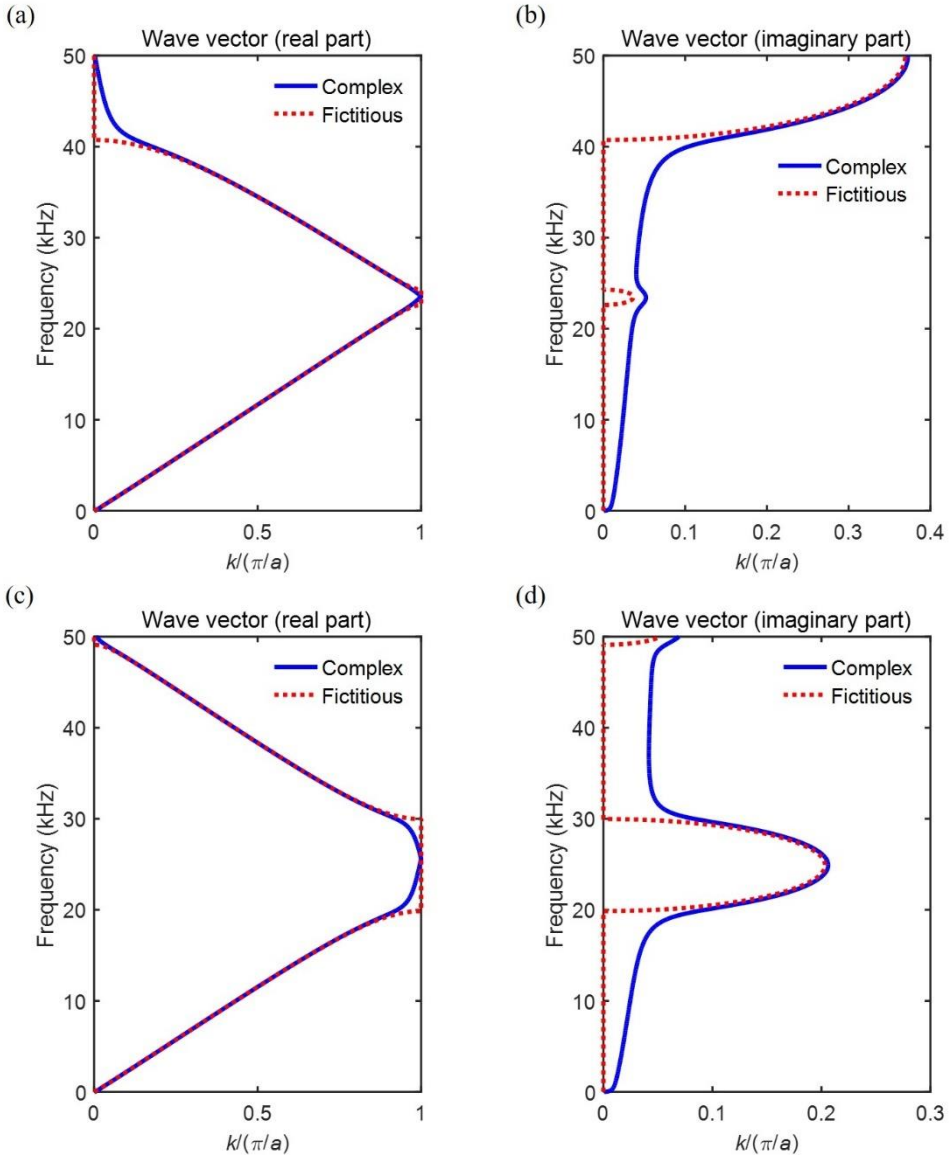

Fig. 4.16: (a) Real part and (b) imaginary part of the band structures for Case 3, (c) real part and (d) imaginary part of the band structures for Case 4 calculated by the TMM for the SMPM structure.

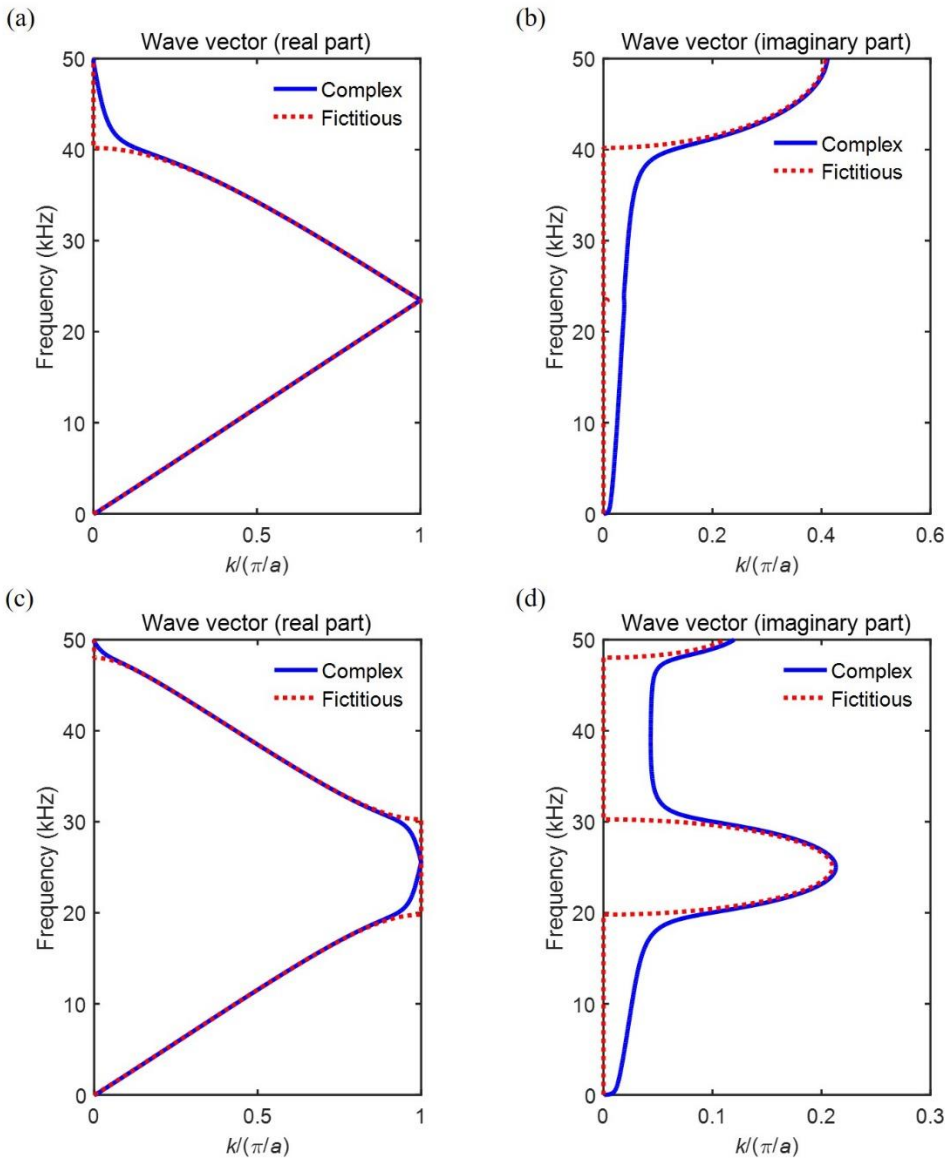

Fig. 4.17: (a) Real part and (b) imaginary part of the band structures for Case 2, (c) real part and (d) imaginary part of the band structures for Case 1 calculated by the TMM for the SMPM structure.

Then the pressure distributions inside the SMPM structure with 5 UCs for Case 1 and Case 2 are presented in Figs. 4.18 and 4.19, respectively. Since the imaginarty part of the wave vector of the band structures characterizes the attenuation effect, in both cases four frequencies are chosen, namely 15kHz, 25kHz, 40kHz and 50kHz to visualize this effect. At 15kHz, in both cases the pressure distributions are quite similar, and the value on the right end is also approximately the same around 0.3Pa. In contrast, at 25kHz, the pressure distributions exhibit significant differences. This is due to the fact that in Case 2 there is only partial attenuation, while in Case 1, it lies in the middle of the bandgap where acoustic waves can no longer pass through, resulting in almost a zero pressure at the right end. At 40kHz, in Case 2 the bandgap starts, while in Case 1 only attenuation dominates. Therefore, at the right end the

pressure is almost 0 in Case 2, yet this value is about 0.2Pa in Case 1. Then at 50kHz, in both cases it is within the bandgap range. After passing through five UCs, the pressure goes down to 0.1Pa in Case 1, while the pressure goes down to 0 after passing only three UCs in Case 2, due to the fact that a larger imaginary part of the wave vector signifies a larger attenuation.

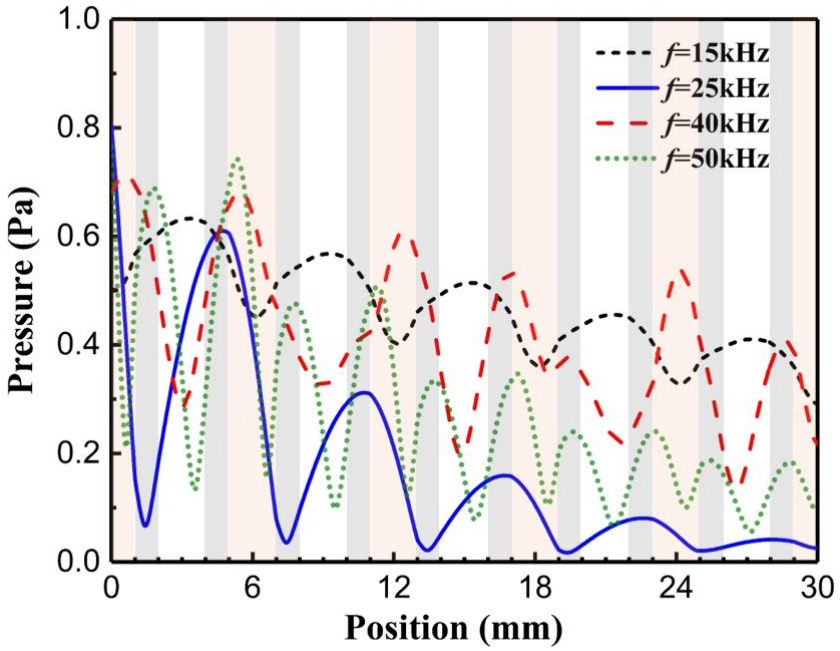

Fig. 4.18: Pressure distribution (Unit: Pa) for the SMPM structure with 5 UCs for Case 1 calculated by the FEM at different frequencies.

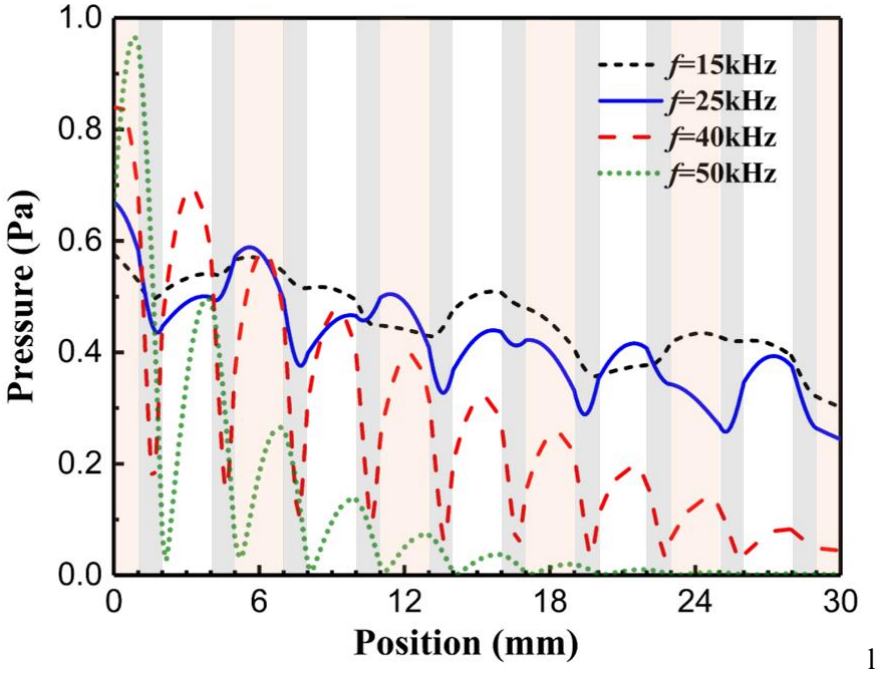

1

Fig. 4.19: Pressure distribution (Unit: Pa) for the SMPM structure with 5 UCs for Case 2 calculated by the FEM at different frequencies.

In the following, the effects of the geometric parameters of the SMPM structure are studied. The lattice constant a and the thickness of the air layer w remain unchanged and the thickness of the two porous materials a_1 and a_2 vary accordingly. Both material composition Case 1 and Case 2 are considered, and the results for the band structures are shown in Figs. 4.20 and 4.21, respectively. Comparing both figures, it is obvious that the layout of the constituent porous materials has a significant impact on the band structures, as simply changing the order of the materials while using the same materials can result in notable differences in the band structures. Besides, keeping the UC size a and the air width w unchanged, regardless of how a_1 and a_2 are altered, the arrangement of Case 1 favours the generation of the bandgaps.

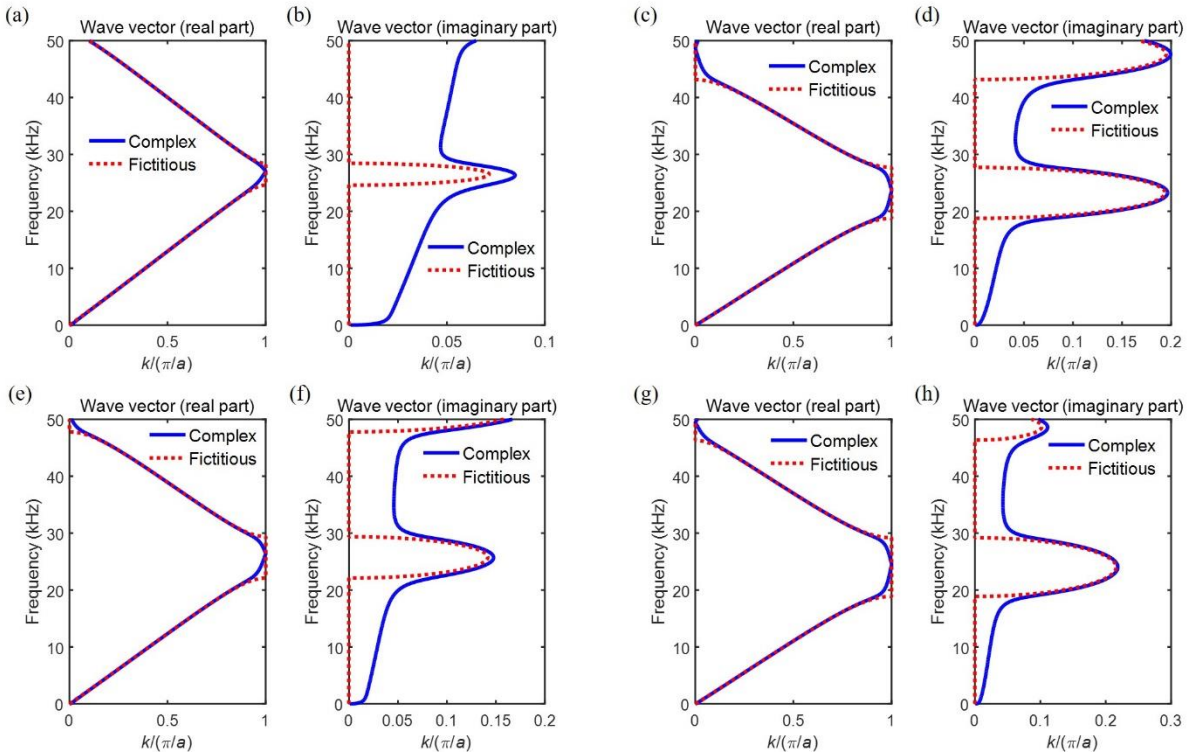

Fig. 4.20: Real and imaginary part of the band structure for SMPM structure for Case 1 calculated by the TMM: (a) and (b) a_1=1.8mm, a_2=0.2mm, (c) and (d) a_1=0.2mm, a_2=1.8mm, (e) and (f) a_1=1.5mm, a_2=0.5mm, (g) and (h) a_1=0.5mm, a_2=1.5mm.

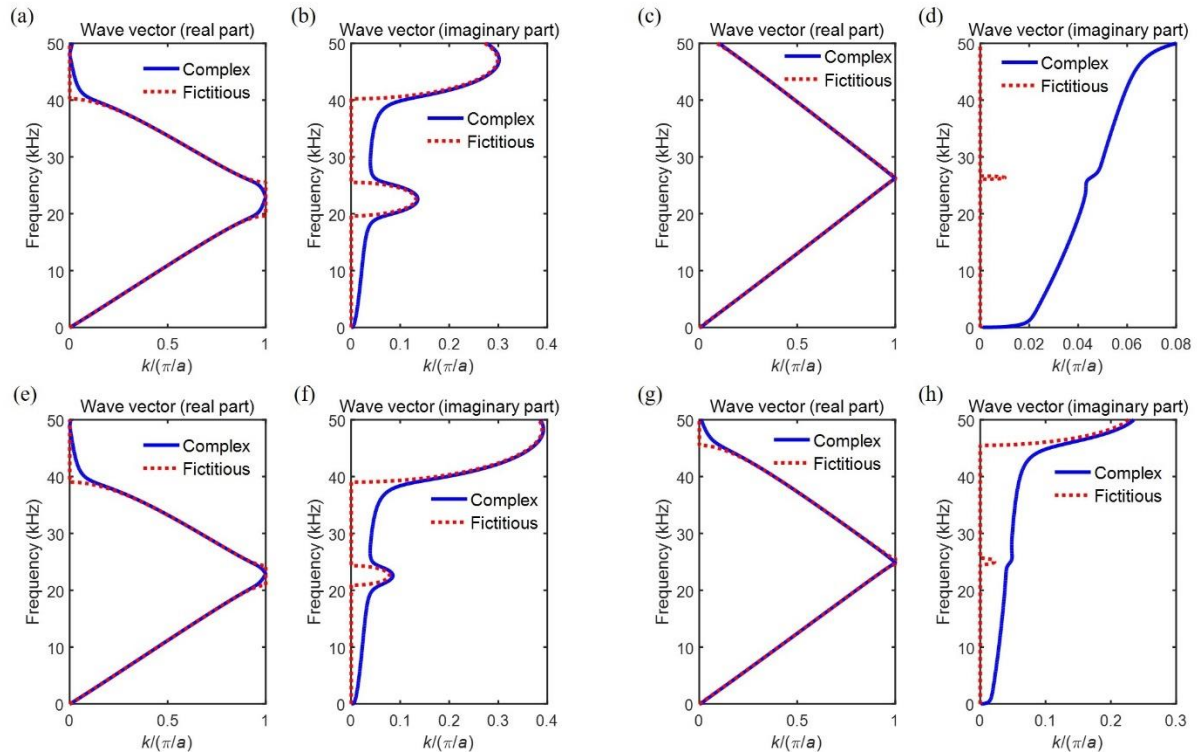

Fig. 4.21: Real and imaginary parts of the band structures for the SMPM structure in Case 2 calculated by the TMM: (a) and (b) a_1=1.8mm, a_2=0.2mm, (c) and (d) a_1=0.2mm, a_2=1.8mm, (e) and (f) a_1=1.5mm, a_2=0.5mm, (g) and (h) a_1=0.5mm, a_2=1.5mm.

4.5 Conclusions

In this chapter, the band structures of different 1D porous metamaterial (PM) structures are studied. To be more specific, the slit-perforated porous metamaterial (SPM) structure, the porous composite metamaterial (PCM) structure and the slit-perforated multi-layered porous metamaterial (SMPM) structure are investigated in details.

The band structures and the transmission spectra or frequency responses are computed by the TMM for the SPM and PCM structures with different material compositions. The transmission spectra correspond well with the imaginary part of the wave vector of the band structures and bandgaps are formed. The bandgap ranges are determined with the help of the band structures calculated by the TMM using the fictitious material properties (only the real part of the equivalent dynamic mass density and bulk modulus), which is further verified by the pressure distribution inside the structure computed by the FEM. A smoothing effect of the boundary of the bandgap in the real part of the wave vector is spotted, which can be explained by the Taylor expansion of the dispersion relations or band structures. The imaginary part of the wave vector of the band structure shows that unlike the conventional metamaterial that the acoustic waves cannot propagate only in the bandgap range, the attenuation also exists outside

the bandgap range for porous metamaterials, which is an obvious advantage. Through the parametrical analysis, it is found that for both SPM and PCM structures, the bandgap is the widest when the two component porous materials have equal width. In addition, the aluminium foam which has a stronger impedance mismatch with air dominates the generation of the bandgap, while the SMF and the glasswool contributes to the attenuation in the whole considered frequency range.

Then the band structures of the SMPM structure are calculated by the FEM (PDE Module) and TMM, and the results agree very well, which further validates both computational methods reciprocally. In contrast to the SPM and PCM structures, the layout of the constituent porous materials is also important for the SMPM structure, which is investigated in details. In the end, the effects of the geometric parameters are studied.

5. Acoustic wave absorption characteristics of a slit-perforated multi-layered porous metamaterial structure

In this chapter, the slit-perforated multi-layered porous metamaterial (SMPM) structure is proposed, which is motivated by the work by Xin et. al [150]. In their work, the slit-perforated DP materials are not only simple in structure, but also exhibit better sound absorption performance compared to its two constituent elements. However, it can be observed that the low-frequency sound absorption performance as well as the global effect are still far from satisfactory. Thus, the SMPM structure with slight modification on the basis of the slit-perforated DP materials is proposed and its acoustic wave propagation characteristics are studied in details, which shows noticeable improvements. The essential results presented in this chapter have been reported in our previously published papers [151] and [152].

5.1 Problem formulation

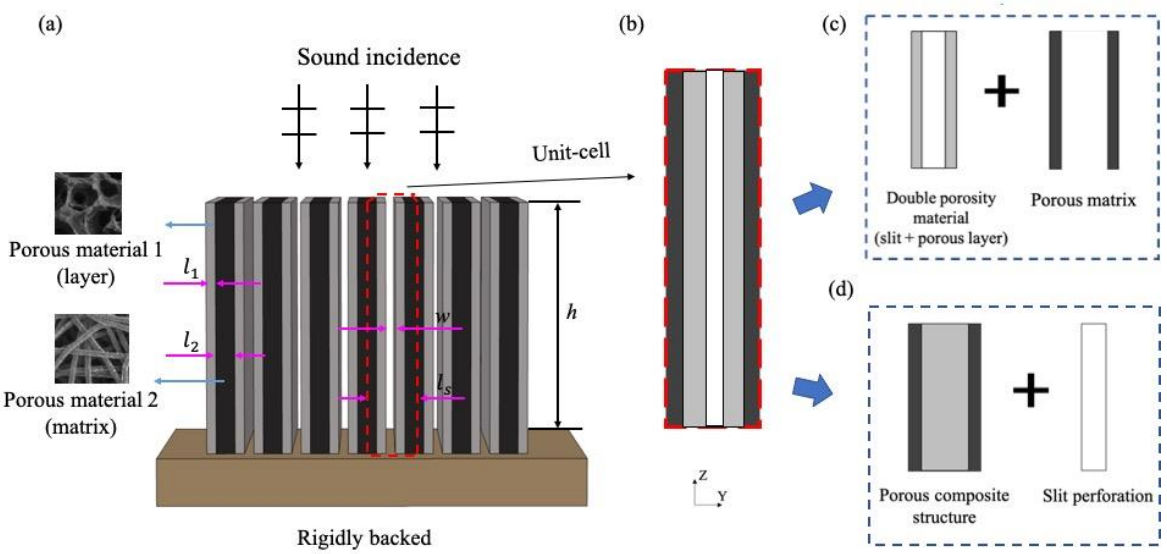

Fig. 5.1: (a) Acoustic wave propagation in the SMPM backed by a rigid plate, (b) UC of the SMPM, (c) Homogenization method 1, (d) Homogenization method 2.

The proposed SMPM is composed of periodic porous matrix layers and periodically distributed adjacent second-type porous layers containing slits as shown in Fig. 5.1. The whole SMPM structure is backed by a rigid plate and a plane time-harmonic acoustic wave is normally incident onto the SMPM structure. The following geometrical parameters of the UC of the SMPM are first chosen in our calculations: l_s=20mm, l_1=4.5mm, l_2=9mm, w=2mm and h=100mm. Different porous materials are used for the calculation, among which SMF, rockwool and glasswool are fibrous porous materials while the others are porous foams. The corresponding material property parameters are already shown in previous chapters.

In order to explore the acoustic wave absorption characteristics of the SMPM, two homogenization methods (HM) can be applied as shown in Fig. 5.1(c) and 5.1(d). The first method is to consider the SMPM as a DP material consisting of the porous material layer and the slit which is included in another porous matrix, while the second method is to consider the SMPM as a porous composite structure with a slit perforation. To be more specific, four steps are needed for the theoretical modelling procedure for both of the two methods and they are introduced in details as follows.

➢ Method 1

- **Step 1: Study of the wave propagation in both porous domains or materials.** For this purpose, motionless skeletons are assumed and the semi-phenomenological JCA model shown in Section 2.2.2 is adopted.
- **Step 2: Investigation of the wave propagation in the slit.** For this purpose, the conventional acoustic theory of slit model with impervious frames as presented in Section 2.2.1 can be applied.
- **Step 3: Analysis of the DP material.** The DP material consists of the porous material layer and the slit, which contains two interconnected networks of pores with different characteristic sizes. Thus, the DP theory introduced in Section 2.2.5 can be applied.
- **Step 4: Analysis of the SMPM structure.** The DP material introduced in Step 3 is embedded now into the porous material matrix and the theory of porous materials with acoustic inclusions (DP materials) as demonstrated in Section 2.2.6 can be applied.

➢ Method 2

- **Step 1:** For method 2, the step 1 is the same as that in Method 1.
- **Step 2: Analysis of the porous composite material.** The porous composite material consists of both the porous matrix and the porous layer as shown in Fig. 5.1 Thus, the porous composite theory of as presented in Section 2.2.6 can be applied.
- **Step 3: Investigation of the wave propagation in the slit.** For this purpose, the conventional acoustic theory of slit model with impervious frames as presented in Section 2.2.1 can be applied.
- **Step 4: Analysis of the SMPM structure.** The SMPM can be considered as the porous composite material obtained in Step 2 with slit perforation, where two interconnected networks of pores with different characteristic sizes are observed. Therefore, the DP theory introduced in Section 2.2.5 can be applied.

In order to validate these two homogenization methods, the results for the sound absorption coefficient are compared with the numerical results obtained by FEM model established in COMSOL Multiphysics considering normal incident acoustic wave. As indicated in Section 3.2, the commercial numerical software COMSOL Multiphysics is capable of calculating the acoustic wave absorption characteristics

accurately and efficiently. Here, the "Pressure Acoustics Module – Frequency Domain" is used for the whole UC. The two porous materials are defined as the "Poroacoustics domain" where the JCA model described by Eq. (2.21) and Eq. (2.22) is applied, while the slit-perforation is defined as the "Air domain" where the Helmholtz equation

$$\nabla^2 p + \frac{\omega^2}{c_0^2} p = 0 \tag{5.1}$$

is applied. In Eq. (5.1), c_0 represents the sound velocity in air, and neither the excess temperature at the air-wall interface, nor the thermal or viscous dissipation in the slit is taken into consideration. As shown in Fig. 5.2, a background pressure field is introduced as the air domain to generate the incident plane acoustic wave. A perfectly matched layer (PML) is applied to the top part of the air domain of the background pressure field to avoid acoustic wave reflections at the top boundary of the air domain of the background pressure field. Free triangular meshes are employed for all the computational domains except the PML, where mapped meshes are used. The choice of free triangular meshes is purely for the convenience to utilize the special meshing performance of COMSOL Multiphysics, and they can be indeed substituted with other types of meshes. As a widely approved rule of thumb and also based on our own experiences, a maximum mesh-size smaller than one-sixth (1/6) of the minimum wavelength is needed to gaurantee the accuracy and convergence of the FEM results. In our numerical calculations, the maximum mesh-size is chosen to be smaller than one-tenth (1/10) of the minimum wavelength in both the porous materials ("Poroacoustics domain") and the slit-perforation ("Air domain"), which is sufficient based on our sensitivity, accuracy and convergence analysis, and the minimum wavelength is defined by the ratio of the sound speed to the maximum frequency of the incidence wave.

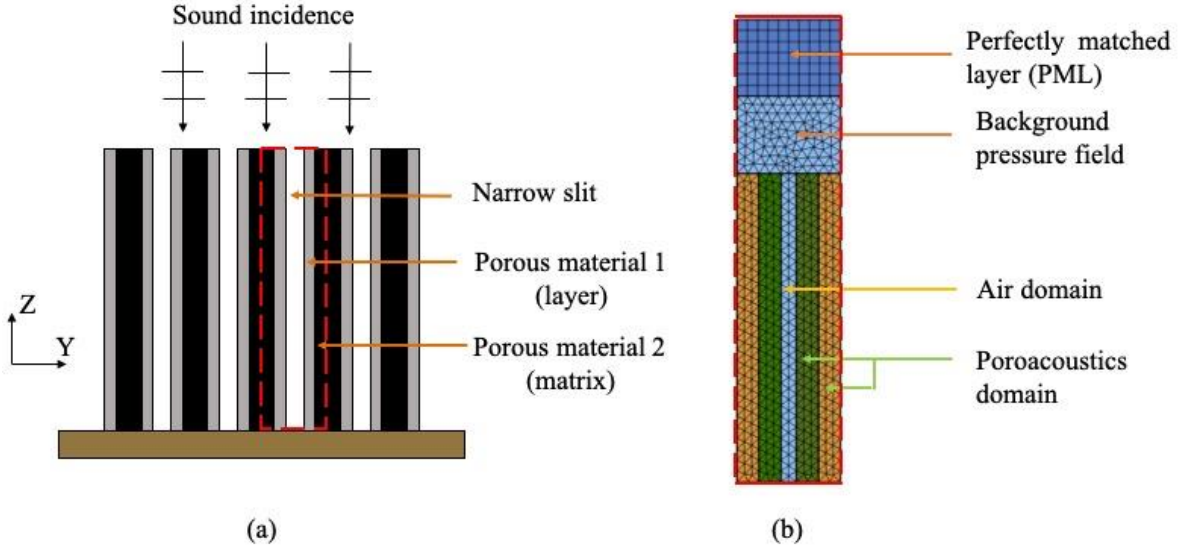

Fig. 5.2: (a) Front view of the considered SMPM with a UC marked by the red-dashed line, (b) partially enlarged view of the FE mesh of the UC.

As indicated in Section 3.2.1, the sound absorption coefficient can be computed through the ratio of the dissipated power inside the SMPM structure to the total power of the incident acoustic wave, which can be computed through defining them in the variable module of COMSOL Multiphysics. Once the pressure distribution within the structure is obtained after calculation, the sound absorption coefficient can be determined.

Table 5.1: Material composition of the considered cases

Case	Porous material 1 (layer)	Porous material 2 (matrix)
1	SMF	Green foam
2	SMF	Rockwool
3	Melamine foam B	Rockwool
4	Green foam	Melamine foam B

We consider the first two cases with different material arrangements as shown in Table 5.1. The comparison of the results calculated by the FEM and both two homogenization methods are shown in Fig. 5.3. The legends “HM1” and “HM2” are used to represent the theoretical results obtained by the two homogenization methods, respectively. It can be observed that fairly good agreements have been achieved between the theoretical and numerical results. However, if we compare more carefully, it can be seen that the results obtained by the HM1 outstands those obtained by the HM2, especially at the peaks. The position of the sound absorption peak calculated by method 2 always deviates from the numerical results to a higher frequency which is not accurate. Thus, in the subsequent works, the homogenization method 1 is adopted.

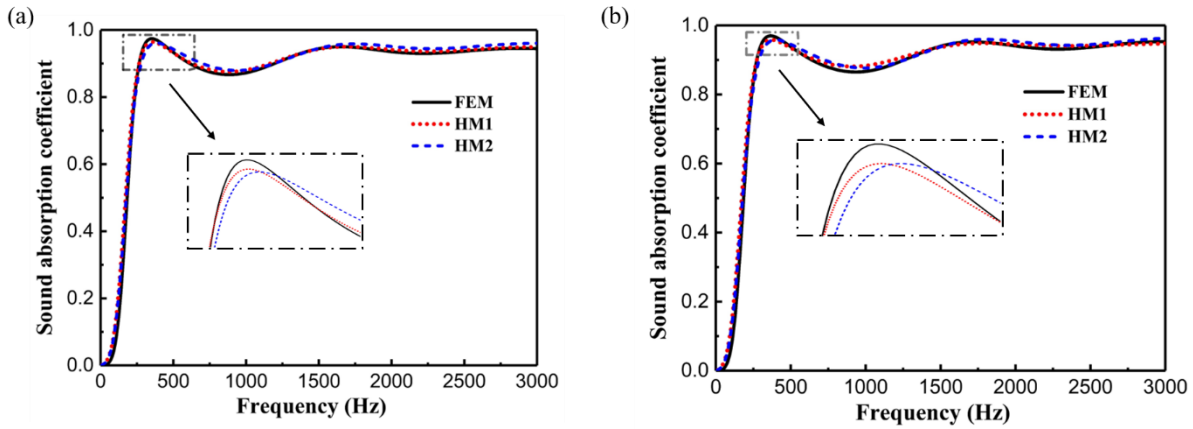

Fig. 5.3: Comparison of the sound absorption coefficient with two homogenization methods (a) Case 1, (b) case 2.

5.2 Results and discussions

In the previous section, the theoretical model is first validated through comparison with the numerical results. In this section, the acoustic wave absorption characteristics of the SMPM not only at room temperature environment, but also at high temperatures will be studied. To be more specific, the superiority of the SMPM is first demonstrated at room temperature with normal incident acoustic waves compared with the slit-perforated DP materials and the sound absorption mechanism are revealed through the analysis of the time-averaged power dissipation density distribution together with the energy dissipation ratio of the two constituent porous materials of the SMPM. Then the effects of various important parameters including the slit-width and the material composition ratio are investigated in order to further improve the design of the SMPM structure. Then the sound absorption coefficients with different oblique incident acoustic waves are given. In the end, the acoustic wave absorption characteristics of the SMPM at high temperatures are studied.

5.2.1 Acoustic wave absorption at room temperature

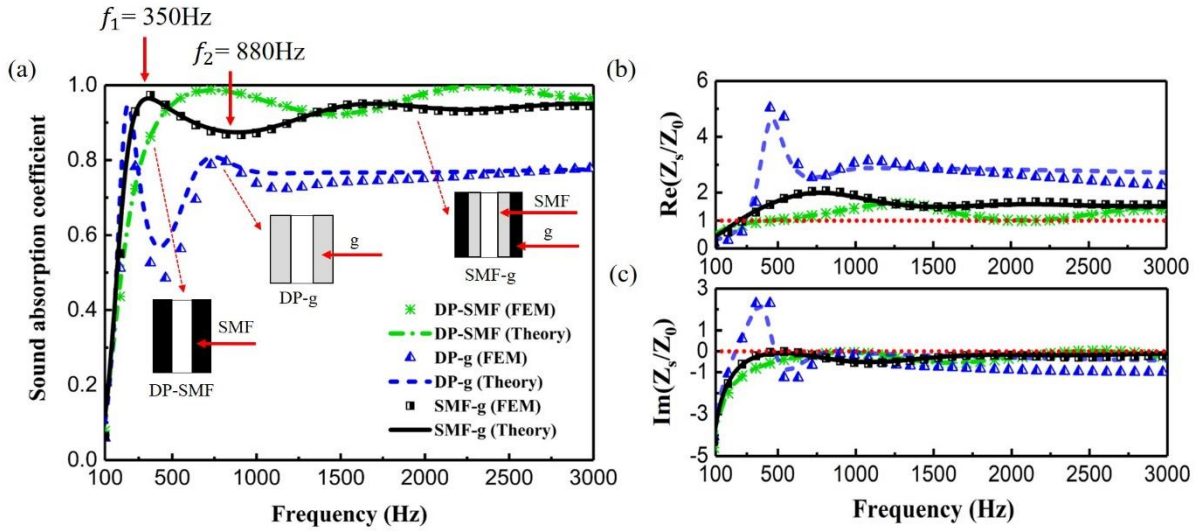

Fig. 5.4: (a) Sound absorption coefficient. (b) Real part and (c) imaginary part of the normalized surface impedance curves of Case 1.

In this section we consider the material arrangements of the first two cases shown in Table 5.2. The reason for selecting the three materials is based on their particular sound absorption characteristics. The sintered metallic fibrous material is a fibrous porous material with a rather low static air-flow resistivity while the green foam and rockwool have rather high static air-flow resistivity. Previous research works [40,150] have shown that the DP rockwool and green foam has a good sound absorption behaviour at low frequencies with a rather high peak value but an unsatisfactory mid-to-high sound absorption performance, while the porous materials [59] with low air-flow resistivity generally have a good sound

absorption characteristic at mid-to-high frequencies. Indeed, the proposed metamaterial concept can be also applied to other material combinations, which have been also investigated in our study. Since the corresponding results show similar enhancement effects on the sound absorption performance, they are not all presented here for the sake of brevity.

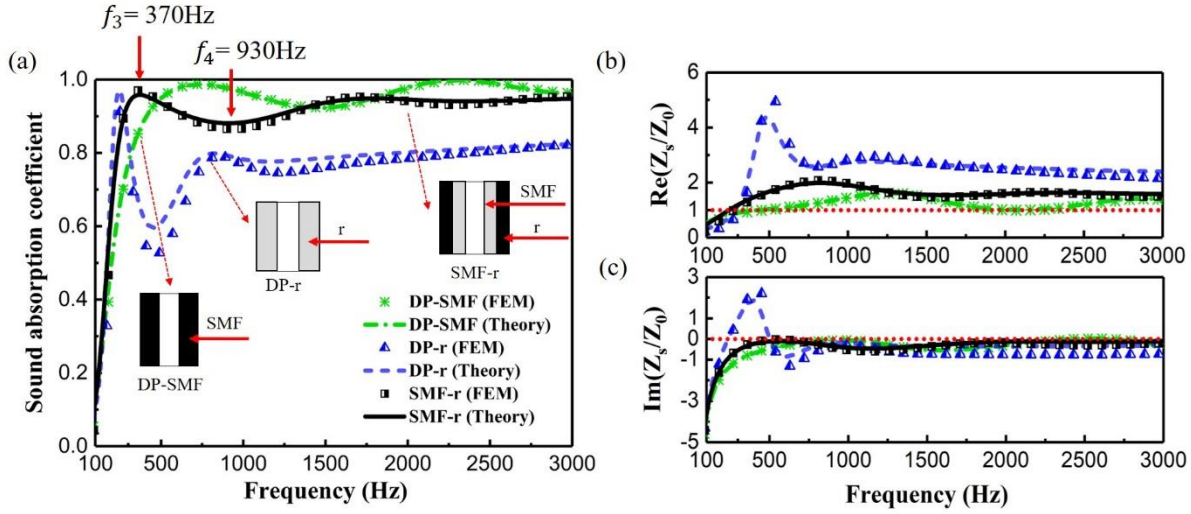

Fig. 5.5: (a) Sound absorption coefficient. (b) Real part and (c) imaginary part of the normalized surface impedance curves of Case 2.

The corresponding sound absorption coefficient as well as the surface impedance (normalized by the characteristic impedance of air) curves for these two cases are shown in Figs. 5.4 and 5.5 respectively. In order to show the superiority of our proposed SMPM, the results for the DP materials (with the same geometrical parameters w, h and l_s) made of SMF, green foam and rockwool are also shown and they are denoted by "DP-SMF", "DP-g" and "DP-r" respectively. It can be observed that excellent agreements between the theoretical and numerical results are achieved for both cases, which again validates the theoretical model established in the previous section. As can be observed in Fig. 5.4 for the DP material made of SMF (DP-SMF), the first sound absorption peak appears at 740Hz with a rather high value of 0.987. However, its sound absorption performance at frequencies lower than 500Hz is much poor. For the DP material made of green foam (DP-g), the sound absorption peak is located at a very low frequency of about 240Hz, and nevertheless, an obvious trough can be observed at around 440Hz and the sound absorption coefficient is below 0.5 which is very low. Besides, at middle frequencies, the sound absorption coefficient is only about 0.8. On the contrary, for our proposed SMPM, the sound absorption peak appears at 350Hz with a value of about 0.974, and the sound absorption coefficient is above 0.8 from 240Hz on. Similar results can be observed for the Case 2 in Fig. 5.5 where the sound absorption peak occurs at 370Hz with a value of about 0.97, and the sound absorption coefficient is above 0.8 from 250Hz on in the considered frequency range. Thus, it can be concluded

that the novel SMPM not only has an excellent sound absorption performance at low frequencies but also an improved global characteristic which indicates a broadband sound absorption capability. This can be explained by its surface impedance curves. For a perfect sound energy absorber [10,153], it is required that the real part of the surface impedance of the structure (acoustic resistance) should equal to that of air (i.e., $\mathrm{Re}(Z_s/Z_0)=1$) and the imaginary part of the surface impedance (acoustic reactance) should equal to zero (i.e., $\mathrm{Im}(Z_s/Z_0)=0$). Impedance matching with air implies that there is no reflection from the sound-absorbing structure, which can ensure that the maximum amount of sound energy can be subject to absorption inside the structure. For example, for the DP material made of SMF (DP-SMF) at around 2300Hz, the normalized acoustic resistance is almost 1 and the acoustic reactance is nearly 0, which results in an extremely high sound absorption coefficient of about 0.998. The better the impedance matching is, the higher the sound absorption coefficient will be.

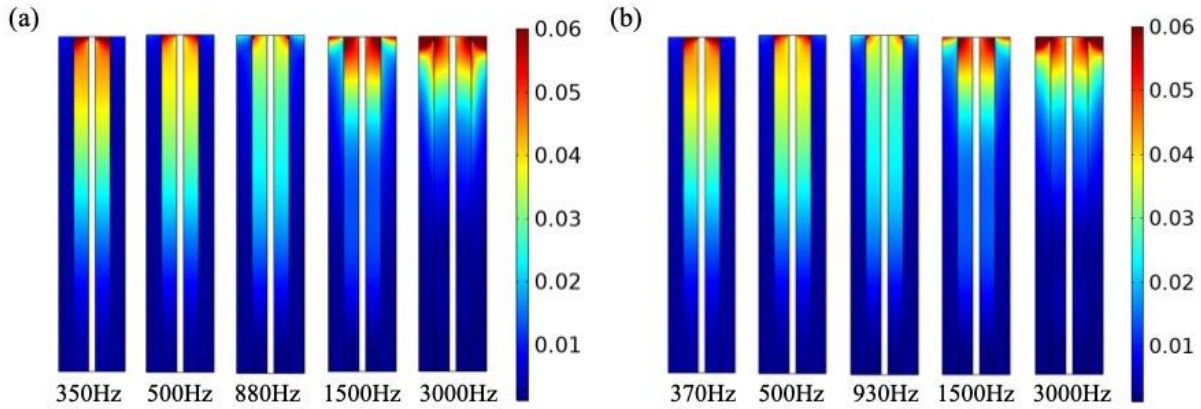

Fig. 5.6: Time-averaged power dissipation density (unit: W/m^3) of the SMPM (a) Case 1 and (b) Case 2.

To unveil the underlying mechanisms of the sound energy absorption, the distribution of the time-averaged power dissipation density inside the UC of the SMPM is shown in Fig. 5.6. As indicated in Section 3.2.1, the total acoustic energy dissipated in each constituent porous material is comprised of two parts: the energy dissipated through the viscous effects and that by the thermal effects, which can be calculated by considering the acoustic wave propagation in an equivalent fluid [39]. For both cases, five different frequencies are chosen, among which 350Hz is the sound absorption peak frequency and 880Hz is the sound absorption trough frequency shown in Fig. 5.4 while 370Hz is the sound absorption peak frequency and 930Hz is the sound absorption trough frequency shown in Fig. 5.5. It can be observed here that most of the energy is dissipated in SMF at low frequencies, while at high frequencies the energy dissipated in green foam also becomes remarkable and there is a concentration at the top surface of green foam. Besides, at 880Hz and 930Hz the lowest energy dissipation appears, which corresponds to the sound absorption trough frequencies f_2 and f_4 in Figs. 5.4 and 5.5 respectively.

Besides the distribution of the time-averaged power dissipation density inside the UC of the SMPM,

the energy dissipation ratio curves for the two considered cases are also plotted in Fig. 5.7 in order to gain a better understanding of the role of each constituent porous material in the sound absorption process. The energy dissipated in each constituent porous material can be calculated through the volume integration of the time-averaged power dissipation density. The energy dissipation ratio is defined as the fraction of the energy dissipated in each constituent porous material relative to the total energy dissipated in the whole UC of the SMPM. It can be seen that in both cases the energy dissipated in the SMF first increases and then decreases while an opposite trend is observed in green foam and rockwool, which is also consistent with the results shown in Fig. 5.6. Based on these two figures it can be deduced that at low frequencies the porous material with a lower air-flow resistivity contributes more to the energy dissipation process, while at high frequencies the contribution of the porous material with a higher air-flow resistivity also becomes remarkable.

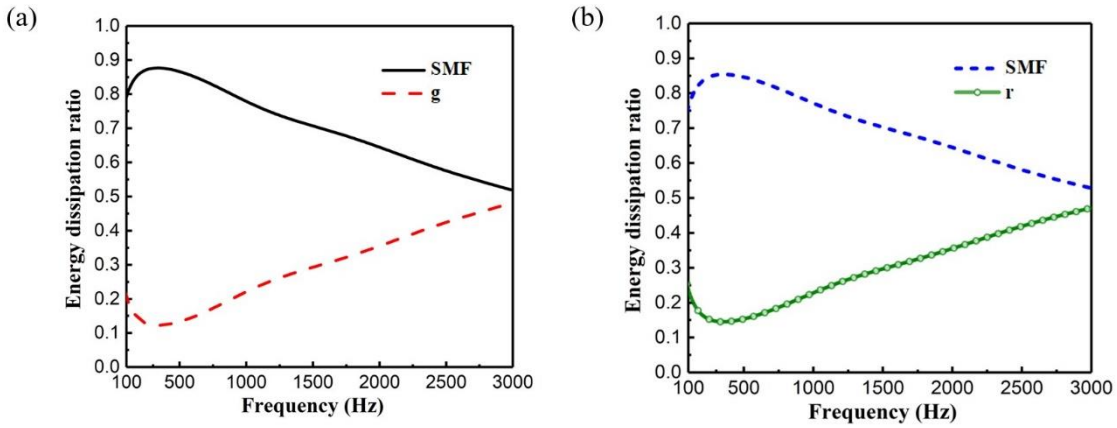

Fig. 5.7: Energy dissipation ratio of the two constituent porous materials of the SMPM (a) Case 1 and (b) Case 2.

5.2.2 Parametrical analysis

5.2.2.1 Effects of the slit width

In this subsection, the effects of the slit width are studied and the material combination of Case 1 is considered. To facilitate the study, we keep l_s=20mm, h=100mm and l_2=2l_1 unchanged and vary the value of the normalized slit width $\phi_s = w / l_s$. The theoretical results of the sound absorption coefficient curves for different ϕ_s are shown in Fig. 5.8. It can be observed that the slit width has a great influence on the sound absorption performance of the SMPM. When the slit width is too small, no sound absorption peak can be observed in the considered frequency range, while if the slit width is too large, there will be more fluctuations in the sound absorption curve. In particular, the first sound absorption peak appears when ϕ_s is larger than 0.05, and the peak frequency gradually moves to a higher frequency

as ϕ_s increases. However, the peak value of the sound absorption coefficient first increases, then decreases, and the maximum sound absorption coefficient can be found at 410Hz with a value of about 0.999 when $\phi_s = 0.15$.

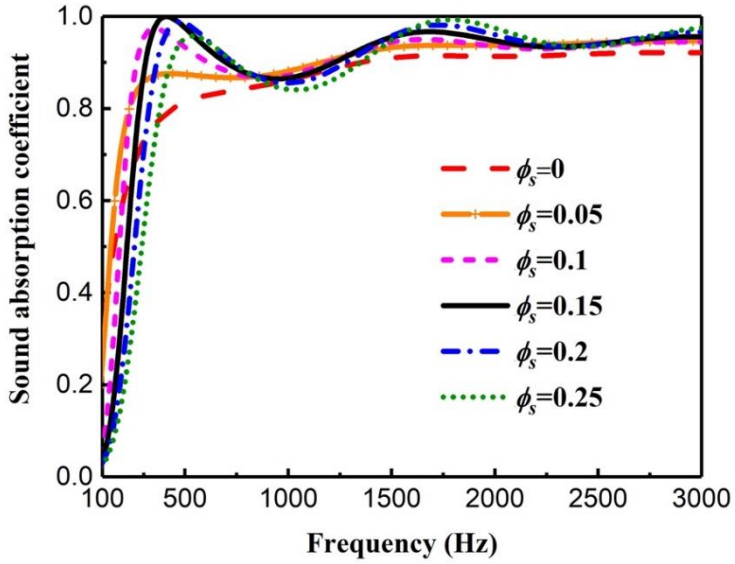

Fig. 5.8: Effect of the normalized slit width on the sound absorption coefficient of the SMPM.

Then, the effect of the normalized slit width on the pressure distribution inside the UC of the SMPM is studied, and the results are shown in Fig. 5.9. When there is no slit, no matter at which frequency, the pressure concentration is always located at the top surface of the UC. However, as the slit width increases, the sound wave can propagate into the UC more easily and reach the bottom rigidly backed plate, where the reflection of the sound wave will occur. Consequently, a higher pressure is located at the bottom part of the UC, especially at low frequencies. As the wave-length is largely reduced at high frequencies, the effect of a wider slit is weakened, which results in a concentration of the pressure still at the top surface of the UC of the SMPM.

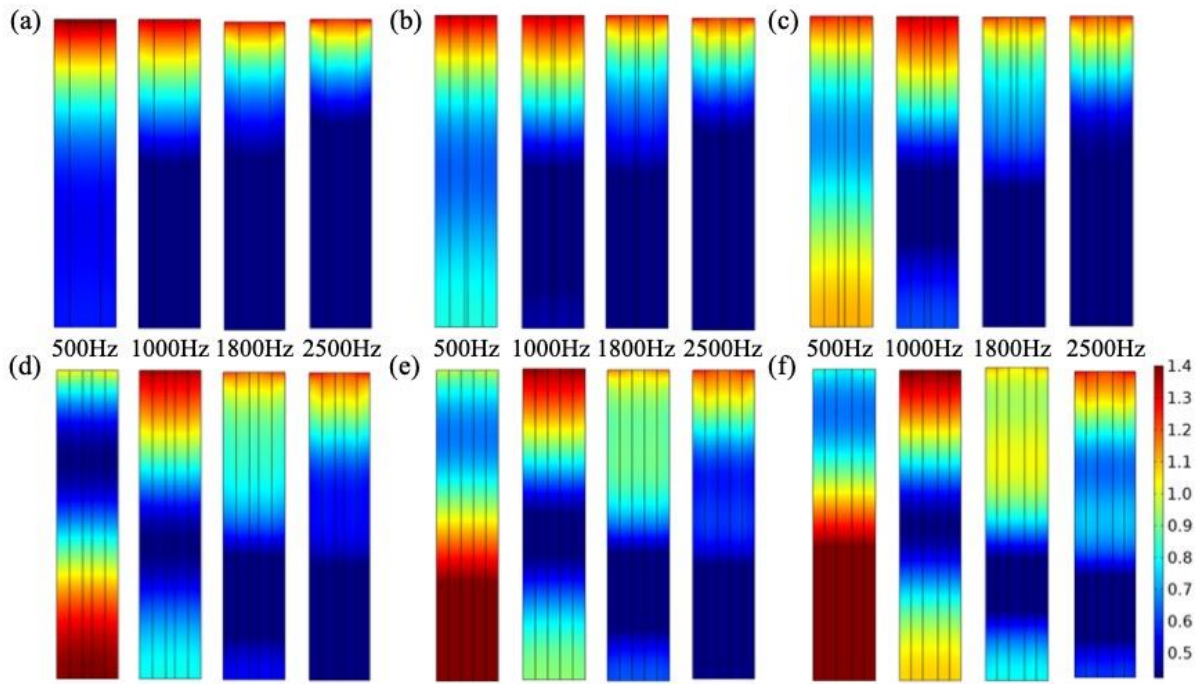

Fig. 5.9: Effect of the normalized slit width on the pressure (Unit: Pa) distribution in the SMPM: (a) $\phi_s = 0$, (b) $\phi_s = 0.05$, (c) $\phi_s = 0.1$, (d) $\phi_s = 0.15$, (e) $\phi_s = 0.2$, (f) $\phi_s = 0.25$.

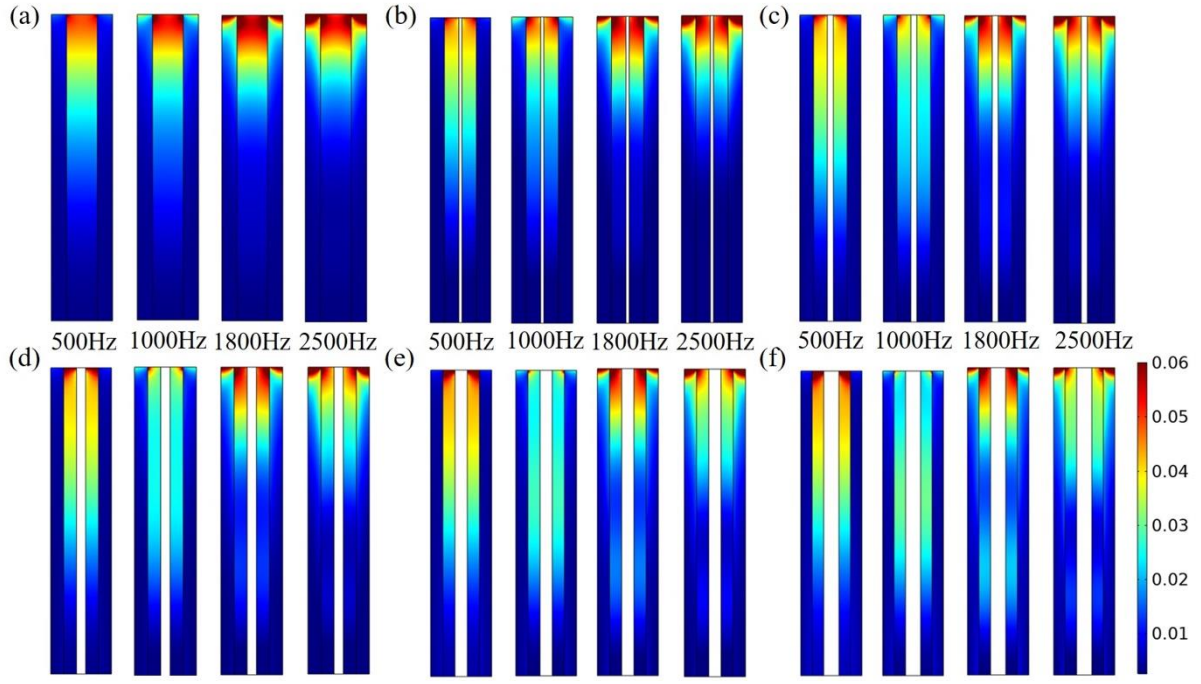

Fig. 5.10: Effect of the normalized slit width on the time-averaged power dissipation density (unit: W/m^3) of the SMPM: (a) $\phi_s = 0$, (b) $\phi_s = 0.05$, (c) $\phi_s = 0.1$, (d) $\phi_s = 0.15$, (e) $\phi_s = 0.2$, (f) $\phi_s = 0.25$.

In terms of the energy dissipation, the effects of the normalized slit width on the time-averaged power dissipation density as well as the energy dissipation ratio of the two constituent porous materials are shown in Figs. 5.10 and 5.11 respectively. It can be seen in Fig. 5.10 that most of the energy is dissipated in SMF at low frequencies, while at high frequencies rockwool also gets more involved in the energy dissipation process, which corresponds to the curves shown in Fig. 5.11. Besides, as the slit width increases, the maximum energy dissipation ratio in the SMF decreases, and the position of this maximum ratio also moves to a higher frequency. However, if there is no slit, the proportion of the dissipated sound energy in both porous materials is almost the same in the middle to high frequency range, while at low frequencies there is only a little difference. Thus, the previous conclusion is once again verified that the two porous materials play different roles in the energy absorption process. That is to say, at low frequencies the porous material with a smaller σ_m contributes more, while at high frequencies the porous material with a larger σ_m also gets more involved. The presence of the slit can promote the sound wave penetrating the SMPM, but if the slit width is too large, the role of the porous materials is diminishing in the sound absorption process which will lead to a lower sound absorption performance.

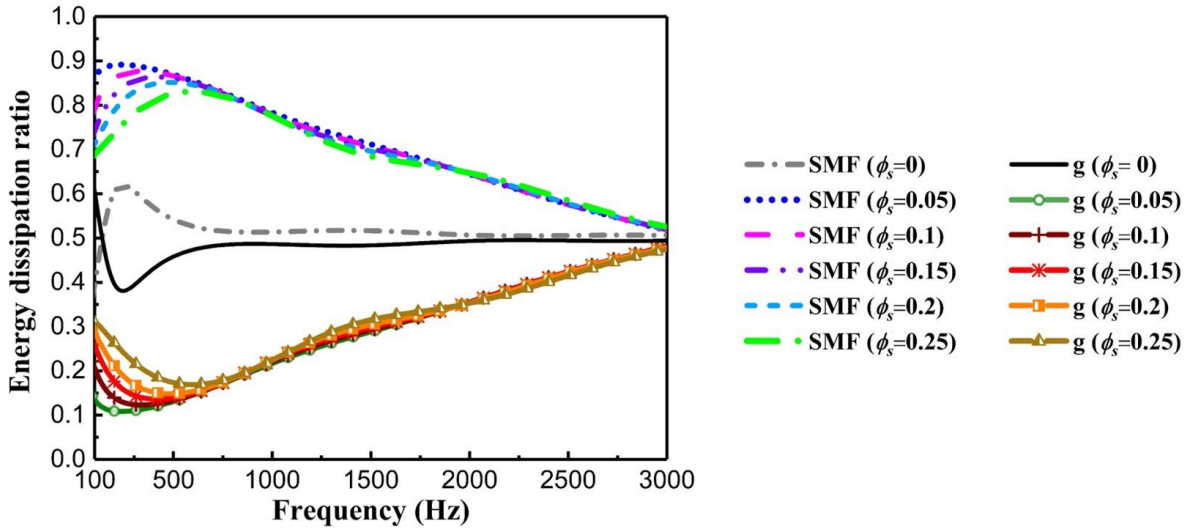

Fig. 5.11: Effect of the normalized slit width on the energy dissipation ratio of the two constituent porous materials.

5.2.2.2 Effects of the material composition ratio

In this subsection, the effect of the material composition ratio of the two constituent porous materials is explored and the material arrangement Case 1 is still used. Here, a new parameter r is defined to represent the ratio of the widths of the two porous material layers. The results for the sound absorption coefficient curves versus r are shown in Fig. 5.12. It is obvious that the material composition ratio has

a great influence on the sound absorption performance of the SMPM. If this ratio is too large or too small, the sound absorption performance of the SMPM will become nearly that of a DP material with either a high value of the low-frequency sound absorption peak or a good high-frequency sound absorption property as shown in Fig. 5.4. In particular, the higher the ratio *r* (which indicates a higher proportion of the porous matrix material green foam) is, the lower the first peak frequency is. However, for a lower ratio *r* the coefficient will be higher in the middle to high frequency range.

Then, the effect of the material composition ratio on the pressure distribution inside the UC of the SMPM is studied, and the results are shown in Fig. 5.13. For all the 6 considered cases at a very low frequency of around 250Hz, the concentration of the pressure always appears in the bottom part of the UC due to the acoustic wave reflections at the rigid back, while the pressure concentration is always located in the top part at middle to high frequencies. However, for the last two cases with a much thinner adjacent porous layer 1, the pressure distribution in the porous matrix in the high-frequency range is no longer perpendicular to the direction of the incident wave because the pressure diffusion effect is generated. In this case, in the slit and the porous layer 1 the inertial force dominates, while in the micro-pores of the porous matrix the viscous effect becomes dominant.

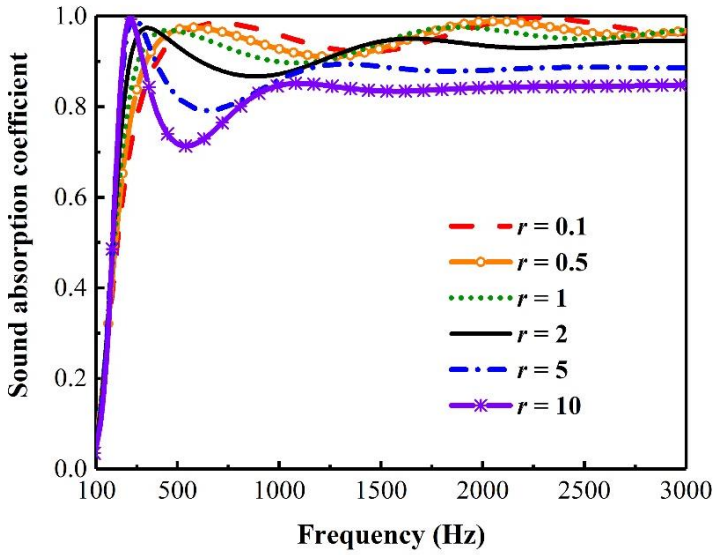

Fig. 5.12: Effect of the material composition ratio on the sound absorption coefficient of the SMPM.

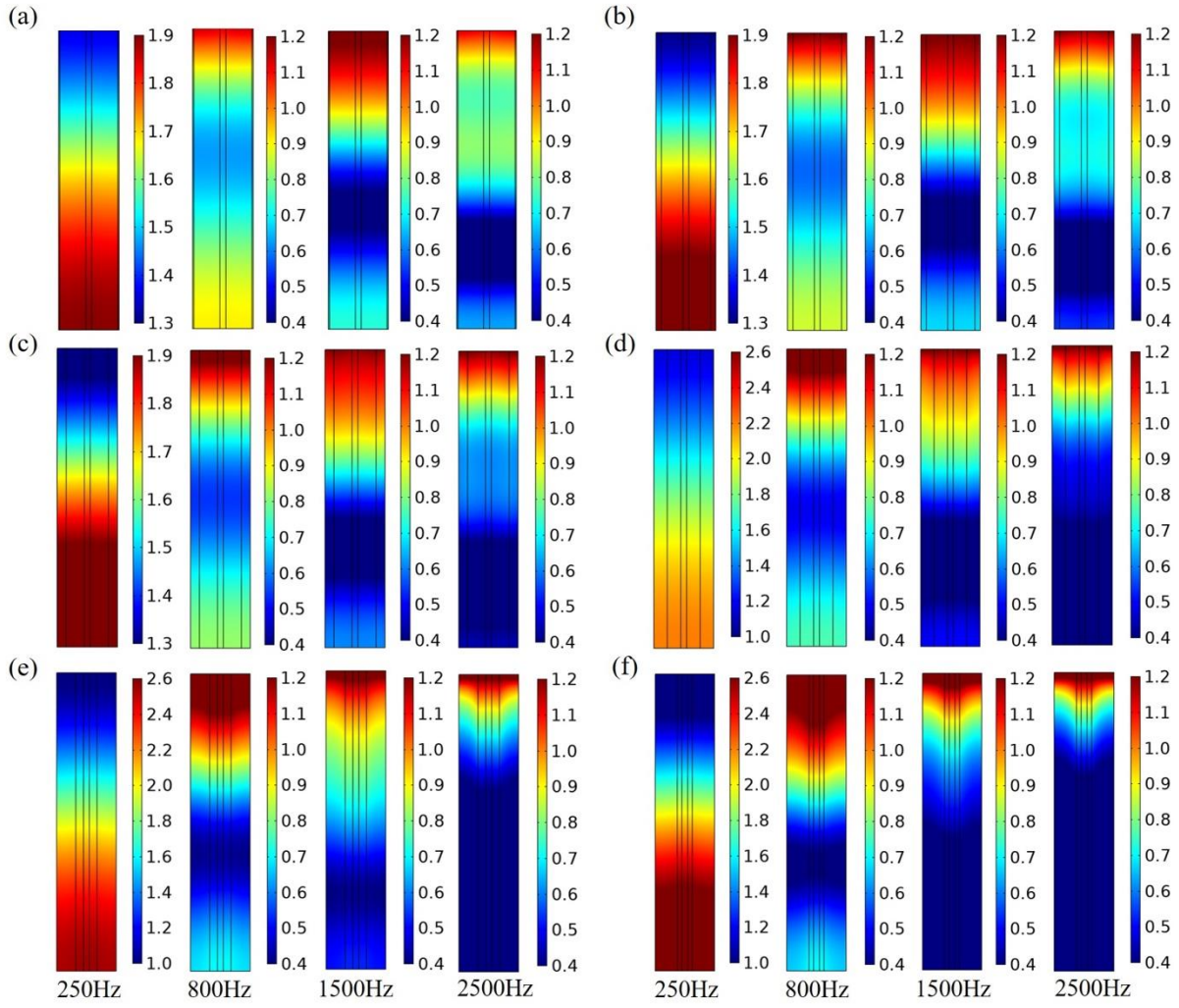

Fig. 5.13: Effect of the material composition ratio on the pressure (Unit: Pa) distribution in the UC of the SMPM: (a) r=0.1, (b) r=0.5, (c) r=1, (d) r=2, (e) r=5, (f) r=10.

Finally, the effects of the material composition ratio on the time-averaged power dissipation density as well as the energy dissipation ratio of the two constituent porous materials are shown in Figs. 5.14 and 5.15 respectively. It can be observed in Figs. 5.14(e) and 14(f) that even for a very thin porous material layer 1, at a very low frequency of around 250Hz most of the energy is still dissipated in this layer and the contribution of the porous matrix layer 2 is relatively small. However, with the increase of the frequency, a concentration of the dissipated sound power always occurs at the top surface of the porous matrix layer 2, which indicates more contribution to the energy dissipation and this corresponds also to the curves of the energy dissipation ratio shown in Fig. 5.15.

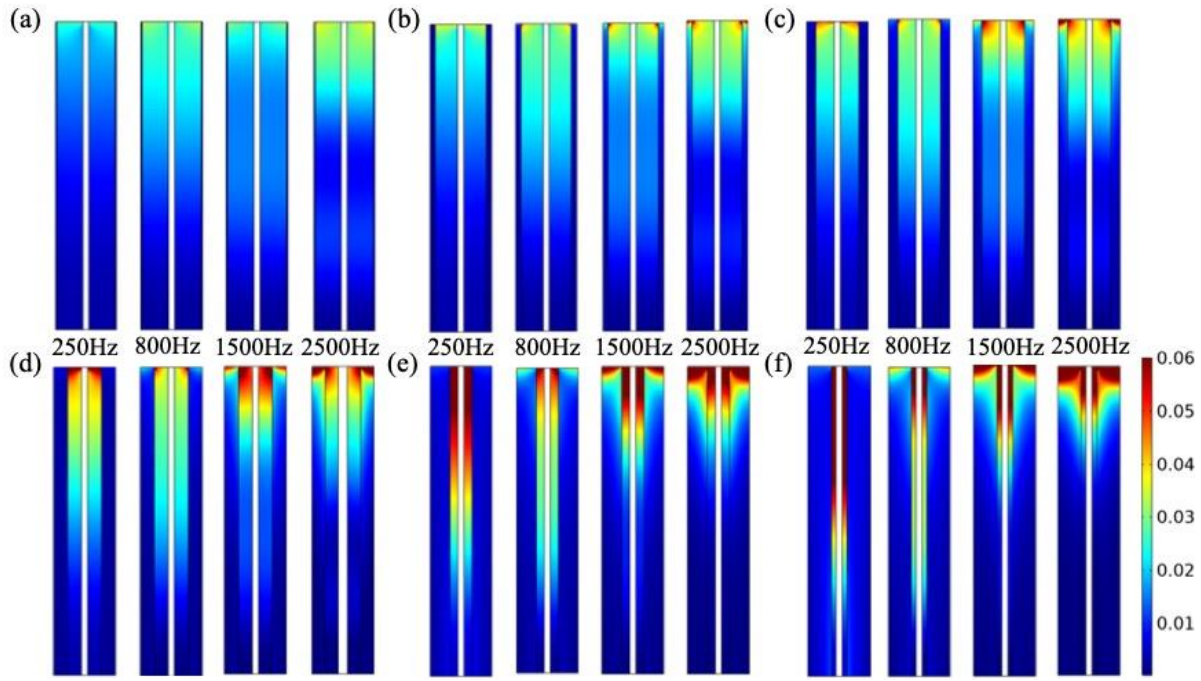

Fig. 5.14: Effect of the material composition ratio on the time-averaged power dissipation density (unit: W/m^3) of the two constituent porous materials: (a) r=0.1, (b) r=0.5, (c) r=1, (d) r=2, (e) r=5, (f) r=10.

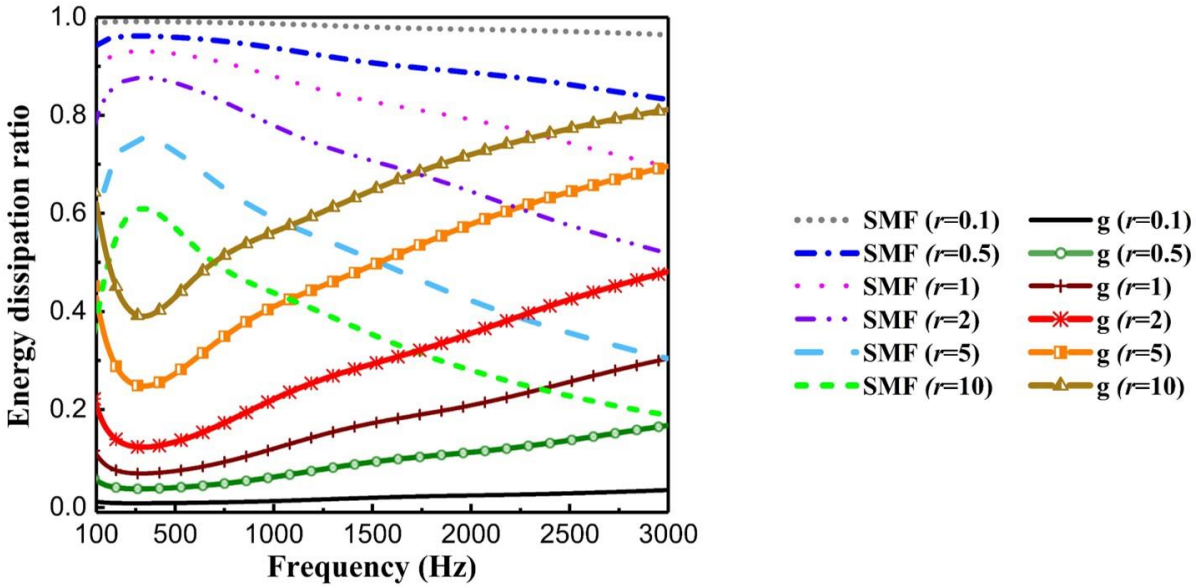

Fig. 5.15: Effect of the material composition ratio on the energy dissipation ratio of the two constituent porous materials.

5.2.3 Oblique wave incidence

In the previous sections, only the acoustic wave absorption characteristics of the SMPM with normal incidence wave are studied. Thus, in this section the oblique incident acoustic wave is considered,

with $\theta = 0°$ representing the normal incident wave. For the theoretical calculation, the equivalent dynamic mass density and equivalent bulk modulus of the SMPM remain the same as the case with normal incidence since they are independent on the incident wave. However, the calculation of surface impedance as well as the reflection coefficient are different, as is presented in Section 3.1. First the theoretical results are validated by comparison with the numerical results and the "m" and "r" in Fig. 5.16 represent the single porosity material made with melamine foam B and rockwool respectively, while material arrangement Case 3 of the SMPM shown in Table 5.2 is used.

Then the results for the sound absorption coefficient with different incident angles varying from 0 to 85° of the acoustic wave for the material arrangements Case 1 and Case 4 are shown in Fig. 5.17. It can be observed that with different incident angles of the acoustic wave, the sound absorption coefficients varies greatly. For Case 1, the maximum sound absorption coefficient can be found at 680Hz with an incident angle of 60° and the value is 0.9991, while for Case 4 it can be found at 690Hz with an incident angle of 55° and the value is 0.9964. Generally speaking, the sound absorption peak gradually moves to a higher frequcncy with the increase of the incident angle, and this peak value first increases then decreases. Besides, the increase of the incident angle will result in a smoother sound absorption curve.

Furthermore, the time-averaged dissipation power density of the two cases with various incident angles of the acoustic wave are shown in Figs. 5.18(a) and 5.18(b), respectively, and for both cases the frequency at which the maximum sound absorption coefficient occurs is selected, namely 680Hz and 690Hz. Irrespective of the mateiral composition, it is evident that as the incident angle of the acoustic wave increases, the energy dissipation in the structure becomes progressively more asymmetric and focused on the upper surface of the structure. Only at normal incidence, the SMPM structure is the most involved in the energy dissipation process.

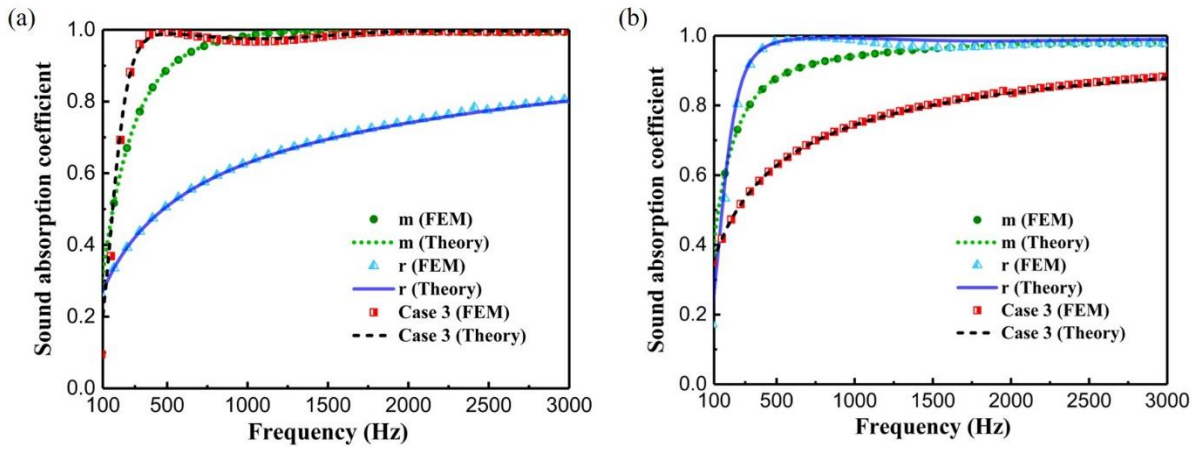

Fig. 5.16: Comparison of the sound absorption coefficients with an incident angle of (a) 45°, (b) 60°.

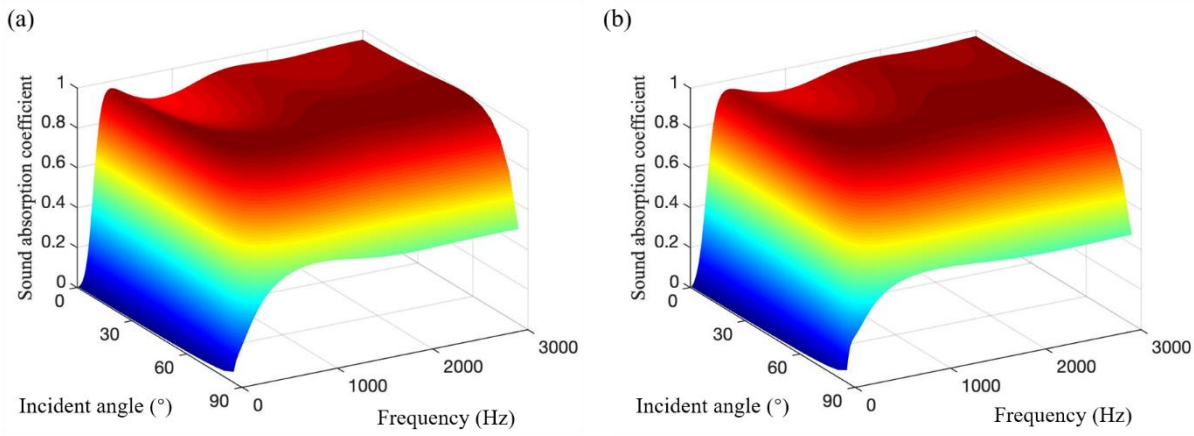

Fig. 5.17: Sound absorption coefficient with different incident angles for (a) Case 1 and (b) Case 4.

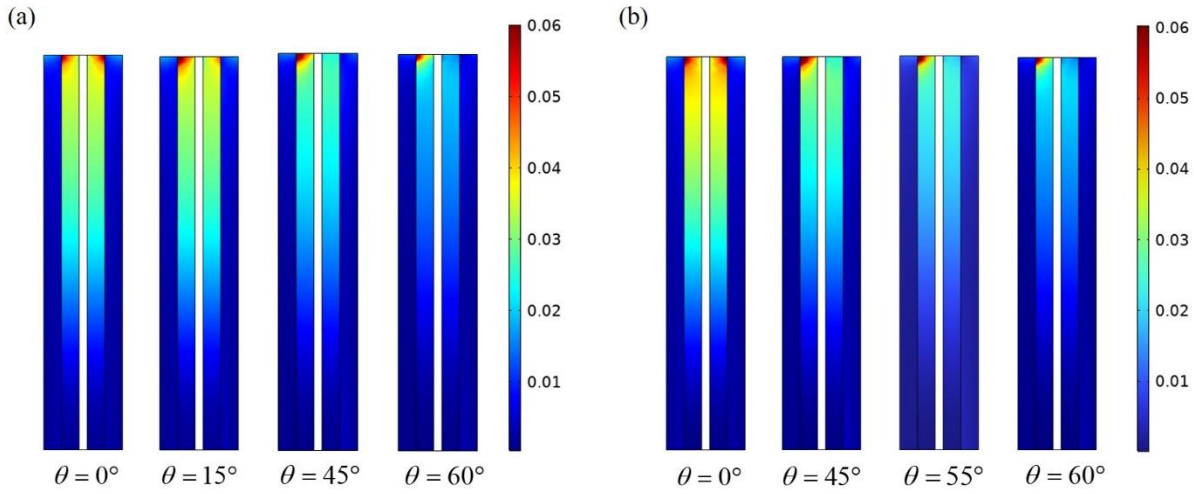

Fig. 5.18: Time-averaged dissipation power density (unit: W/m^3) for (a) Case 1 with f =680Hz and (b) Case 4 with f =690Hz.

5.2.4 High temperature effects

Table 5.2: Air-flow resistivity of the porous materials at high temperatures (unit: N · s/m^4)

Material	t =20°C	t =100°C	t =300°C	t =500°C
SMF	12057	13935	18028	21575
Rockwool	135000	156030	201860	241570

In this section, the acoustic wave absorption characteristics of the SMPM at high temperatures are investigated. It should be noted that the porous foams usually cannot withstand the high temperature and are usually flammable, so only the SMF and rockwool can be used and the material composition of Case 2 in Table 5.1 is adopted. As mentioned in Section 2.2.4, only the air-flow resistivity of the porous

material varies greatly with temperature, and the values for the SMF and rockwool are shown in Table 5.2.

The air properties at high temperatures are calculated in Section 2.2.4. Thus, the new air properties and material parameters can be applied to the JCA model and the sound absorption coefficient of the SMPM at high temperatures can be deduced with the same procedure as presented in the Section 5.1. We first consider the case with the same geometrical parameters in Section 5.2.1 and the results are shown in Fig. 5.19. It can be observed that with the increase of the temperature, the sound absorption peak will gradually move to a higher frequency and the sound absorption coefficient curve will become more fluctuated, which leads to a worse global effect. The results for the real and imaginary part of the normalized surface impedance can also explain this phenomenon as presented in Section 5.2.1.

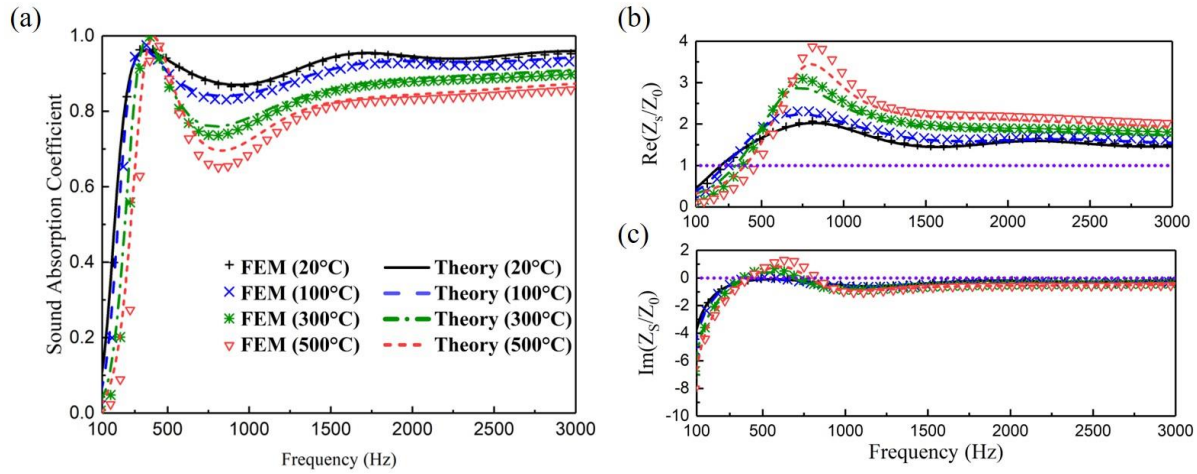

Fig. 5.19: (a) Sound absorption coefficient. (b) Real part and (c) imaginary part of the normalized surface impedance curves of the SMPM at high temperatures.

5.3 Conclusions

In this chapter, a slit-perforated multi-layered porous metamaterial (SMPM) structure is proposed and its acoustic wave absorption characteristics are studied in details. The SMPM consists of periodic porous matrix layers and periodically distributed adjacent second-type porous layers containing slits and its sound absorption performance with normal incidence is greatly improved compared with DP materials. The sound absorption mechanism is further explored through the distribution of the time-averaged power dissipation density and the energy dissipation ratio of the two constituent porous materials. To provide further details, the porous material with low air-flow resistivity contributes more at low frequencies, while the porous material with high air-flow resistivity also gets more participated at medium to high frequencies.

Then the effects of some key parameters are analysed, including the slit-width and the material composition ratio. The introduction of the slit will bring about the sound absorption peak in the considered frequency range, but if the slit width is too large, there will be more fluctuations in the sound absorption curve and the peak frequency gradually moves to a higher frequency with the increase of the slit width. The maximum sound absorption coefficient can be found at 410Hz with a value of about 0.999 when $\phi_s = 0.15$ using the sintered metallic fibrous material and the green foam as the constituent materials. As for the material composition ratio, the results reveal that a higher proportion of the porous material with higher air flow resistivity will lead to a lower peak frequency.

Besides, the sound absorption coefficients considering different incident angles of the acoustic wave are presented considering two material arrangements of the SMPM. The 3D diagrams show intuitively how the sound absorption coefficient changes at different frequencies with the variation of the incident angle. To be more specific, the sound absorption peak moves to a higher frequency gradually with the increase of the incident angle, and this peak value first increases then decreases. Besides, the increase of the incident angle will result in a smoother sound absorption curve.

In the end, the acoustic wave absorption characteristics of the SMPM at high temperatures are explored. As the temperature increases, the sound absorption peak will gradually move to a higher frequency and the sound absorption coefficient curve will become more fluctuated, which leads to a worse global effect.

6. Acoustic wave absorption characteristics of a novel multiscale porous metamaterial structure

6.1 Problem formulation

In this chapter, a novel multiscale porous metamaterial (MPM) structure is proposed and its acoustic wave absorption characteristics are investigated in details. In essence, the contents of this chapter rely on our previous works reported in references [154] and [155]. We consider the acoustic wave propagation in the novel MPM structure as shown in Fig. 6.1(a). The structure consists of three parts: a porous matrix (porous material 2), evenly distributed meso-pores in a square or hexagonal lattice pattern, and another porous layer (porous material 1) which is introduced between the meso-pores and the porous matrix. The whole novel MPM structure is backed by a rigid plate and a plane time-harmonic acoustic wave is normally incident onto the novel MPM structure.

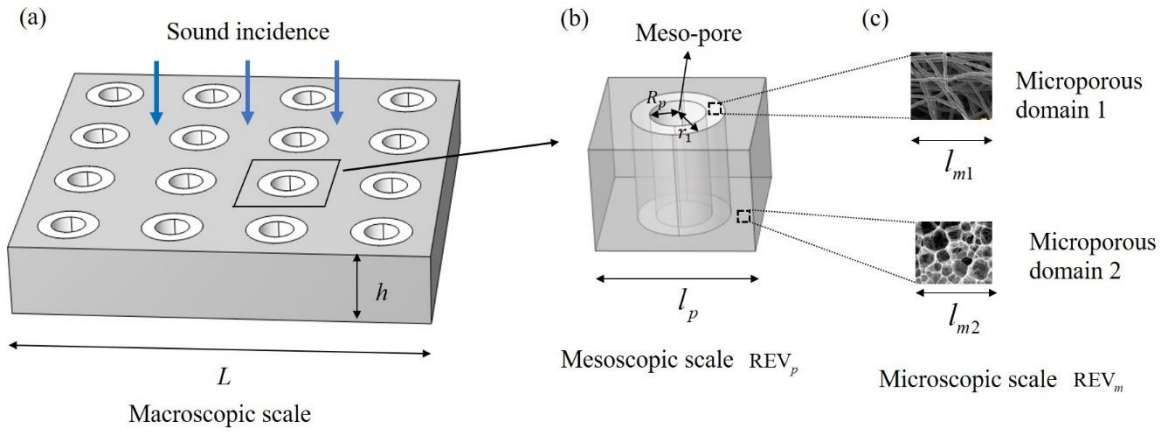

Fig. 6.1: Acoustic wave propagation in the novel MPM structure with square lattice pattern backed by a rigid wall. (a) Macroscopic scale, (b) mesoscopic scale (UC), (c) microscopic scale.

In order to analyze the acoustic wave propagation in the novel MPM structure, a homogenization method [39] is utilized. Three characteristic lengths are introduced to represent different scales of the novel MPM structure, as shown in Figs. 6.1 and 6.2. Besides, two representative volume elements $\mathrm{REV_p}$ and $\mathrm{REV_m}$ are defined for the mesoscopic and microscopic scale respectively. Here, L represents the macroscopic characteristic length and can be determined by the wavelength of the incident acoustic wave, while l_p and l_{mi} (i=1, 2) represent the mesoscopic and microscopic characteristic lengths, respectively. In order to represent the novel MPM structure as a homogenized equivalent medium, a distinction between the macroscopic, mesoscopic and microscopic scales is required by assuming $l_p/L \ll 1$ for the meso- and macro-scales, and $l_{m1}/l_p \ll 1$, $l_{m2}/l_p \ll 1$ for the micro- and meso-scales.

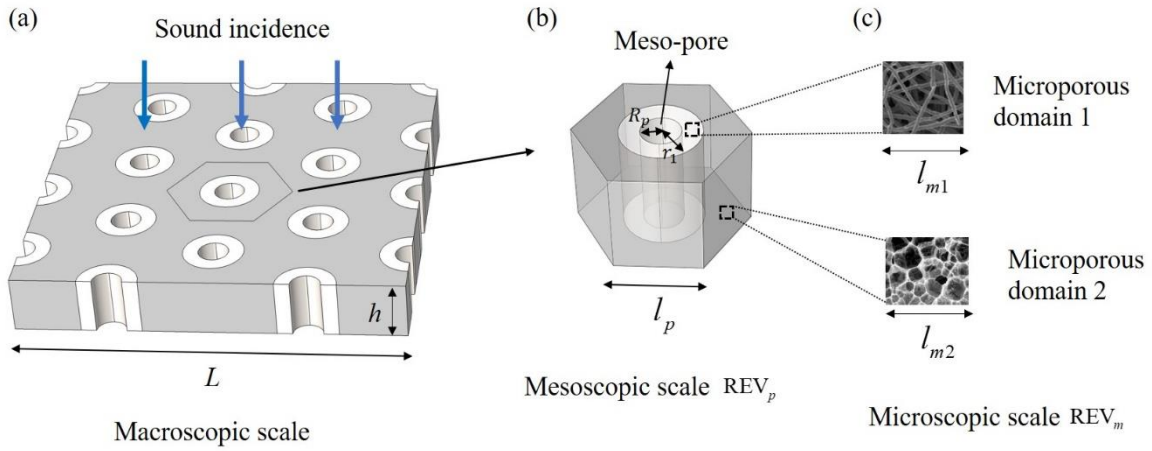

Fig. 6.2: Acoustic wave propagation in the novel MPM structure with hexagonal lattice pattern backed by a rigid wall. (a) Macroscopic scale, (b) mesoscopic scale (UC), (c) microscopic scale.

To describe the macroscopic acoustic behavior of the proposed novel MPM structure, a representative UC with thickness h is considered for simplicity, which is shown in Fig. 6.1(b). The side length (lattice constant) of the UC is a (which means l_p equals to a here), and R_p represents the radius of the mesopore of the UC. The thickness of the inserted porous layer (material 1) can be expressed as r_1-R_p. Here, $\phi_p = \pi R_p^{\,2} / a^2$ is used to represent the mesoscopic porosity of the UC. In order to simplify the analysis and derive explicit analytical expressions for the equivalent dynamic mass density and bulk modulus, an equivalent circular UC which has the same area as the square or hexagonal UC is introduced, with r_2 denoting the radius of the equivalent circular UC as shown in Fig. 6.3. Thus, we have $r_2 = \sqrt{a^2/\pi}$ for the square lattice and $r_2 = \sqrt{3\sqrt{3}a^2/2}$ for the hexagonal lattice and the porosity $\phi_{p2} = \pi r_1^2 / a^2 = r_1^2 / r_2^{\,2}$. Hence, the porosity of the whole UC ϕ can be expressed as

$$\phi = \phi_p + \phi_{p2} \cdot \phi_{m2} + \left(\phi_{p2} - \phi_p\right) \cdot \phi_{m1}, \tag{6.1}$$

where ϕ_{mi} denotes the porosity of the two porous materials 1 and 2.

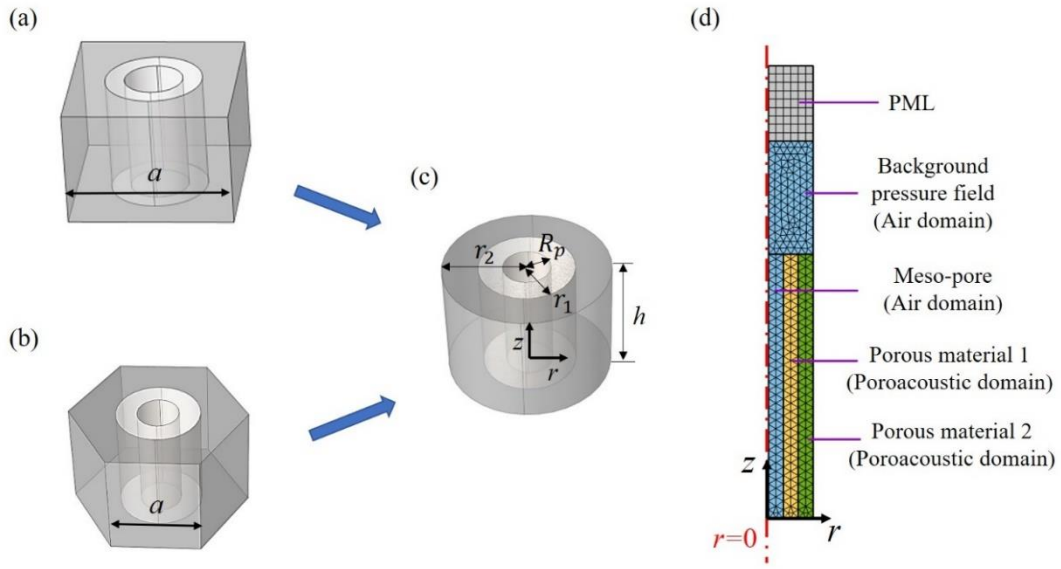

Fig. 6.3: Schematic representation of (a) the square UC, (b) the hexagonal UC, (c) the equivalent circular UC, (d) FE mesh of the equivalent UC.

Based on the homogenization methods [39] as described in Chapter 2, for acoustic wave propagation, all the porous materials 1 and 2, the meso-pore domain, as well as the DP material and the porous composite structure can be represented by their equivalent fluid media on the macroscopic scale. Therefore, they can be described by their equivalent acoustic parameters, such as dynamic mass density, bulk modulus, characteristic impedance and wave number. In what follows, the subscript m is used to distinguish the acoustic parameters related to the two porous materials, and the subscript 1 refers to the inner porous layer while the subscript 2 refers to the outer porous matrix. The parameters labelled with the subscript p represent the parameters of the meso-pore domain. The subscript dp denotes the DP material composed of the porous layer (material 1) and the meso-pore, and the quantities without any subscripts apply for the whole UC of the novel MPM structure. In order to estimate the acoustic property of the UC, the following four steps are needed:

- **Step 1: Study of the wave propagation in both microporous domains or materials.** For this purpose, motionless skeletons are assumed and the semi-phenomenological JCA model is adopted, and ρ_{mi} and K_{mi} of the two porous materials can be obtained.

- **Step 2: Investigation of the wave propagation in the meso-pore domain.** For this purpose, the analytical model for describing homogeneous medium with cylindrical pores can be applied, and ρ_p and K_p can be calculated.

- **Step 3: Analysis of the DP material**. The DP material consists of the inner porous layer (material 1) and the meso-pore, which contains two interconnected networks of pores with different

characteristic sizes. Thus, the DP theory presented in Section 2.2.5 can be applied and ρ_{dp} and K_{dp} can be deduced.

- **Step 4: Analysis of the novel MPM structure.** The DP material introduced in Step 3 is embedded now into the porous matrix (material 2), which forms a porous composite structure and the theory of porous composite structure demonstrated in Section 2.2.6 can be applied. Therefore, the equivalent dynamic density ρ and bulk modulus K of the novel MPM structure can be deducted. By utilizing the computational methods illustrated in Chapter 3, the acoustic wave absorption characteristics of the novel MPM structure can be computed.

Table 6.1: Geometrical parameters of the considered cases.

Configuration	R_p (mm)	r_1 (mm)	r_2 (mm)	h (mm)	ϕ_p	ϕ_{p1}	ϕ_{p2}
1	5	10	15	100	0.1111	0.25	0.4444
2	10	20	30				

Since both of the square and the hexagonal UC can be considered by an equivalent cylindrical UC, in the following studies, the radius of the cylindrical UC r_2 is used for the sake of simplicity, based on which the lattice constant *a* can be deduced. We first consider the case when the radius of the meso-pore and the thicknesses of the two porous materials are identical, which means $R_p = r_1 - R_p = r_2 - r_1$, and another porosity for the structure is defined with $\phi_{p1} = R_p^{\,2} / r_1^{\,2}$. The geometrical parameters of the two chosen configurations are shown in Table 6.1, and rockwool and melamine foam B are used as the constituent porous materials whose material parameters are shown in Table 3.1. The rockwool is a porous material with a rather high static flow resistivity while the melamine foam B has a rather low static flow resistivity. It should be noted that other material selections are also feasible, such as the sintered metallic fibres and the green foam which were used in the previous chapter for the study of SMPM, but in this chapter only the material arrangement with rockwool and melamine foam is studied in details.

There are two possible material arrangements for the proposed novel MPM structure. In the first arrangement the rockwool is the inner layer and the melamine foam is the outer matrix, which is represented by “r-m” in the following sections for the sake of simplicity, and for the second arrangement the melamine foam is the inner layer and the rockwool is the outer matrix, which is represented by “m-r”. In the following, both situations are studied in the frequency range of 100-2000Hz, as the noise control with a better global effect in the low and medium frequency range is of great concern and needs to be further improved. The corresponding viscous characteristic frequency of the inner porous layer

ω_{VM1} and the characteristic frequency of the pressure diffusion effect ω_{d1} as well as the determination of the permeability contrast case for these two configurations with the corresponding material arrangements are shown in Table 6.2. The selection of the porous material and the geometrical parameters can include both the LPC and HPC cases.

Table 6.2: Determination of the permeability contrast cases for the two configurations with different material arrangements.

Case	Configuration	Material arrangement	ω_{d1} (rad/s)	ω_{VM1} (rad/s)	Frequency range f (Hz)	Angular frequency range ω (rad/s)	Conditions of HPC	PC case
1	1	r-m	67467	49129	100-2000	628-12566	$\omega \ll \omega_{VM1}$	LPC
2	1	m-r	819490	8444				LPC
3	2	r-m	16867	49129			$\omega_{d1} \ll \omega_{VM1}$	HPC
4	2	m-r	204870	8444				LPC

In order to validate the proposed theoretical model and gain a better understanding on the sound absorption mechanism, a numerical model is established using the finite element (FE) software COMSOL Multiphysics. The equivalent cylindrical UC is adopted in the numerical analysis so that the 2D axisymmetric model can be applied which can significantly improve the computational efficiency while maintaining the accuracy. The equivalent UC is shown in Fig. 6.3(c) and its corresponding numerical model with the FE mesh is shown in Fig. 6.3(d). The red dash-dotted line represents the rotation axis of the 2D axisymmetric model and all the other three sides are sound-hard boundaries. The "Pressure Acoustics Module - Frequency Domain" is used and the whole UC consists of four different mesh domains: the top part is a Perfectly matched layer (PML), the incident acoustic field is a Background Pressure field, the meso-pore is an air domain, and the two porous materials 1 and 2 are defined as Poroacoustic Domains, which are described by the JCA model. Free triangular meshes are used for all the computational domains except the PML, where mapped meshes are used. In order to obtain sufficient accuracy, the size of all the meshes are defined to be smaller than one-tenth of the minimum wave length in the structure, which is calculated by the ratio of the acoustic wave velocity to the frequency.

The surface impedance is calculated by $Z_s = \langle p \rangle / \langle v \rangle$, where $\langle p \rangle$ and $\langle v \rangle$ represent the average values of the sound pressure and the normal velocity of the particles on the top surface of the structure, respectively. Thus, the sound absorption coefficient can be deduced by Eqs. (3.12) and (3.13).

6.2 Results and discussions

6.2.1 Acoustic wave absorption at room temperature

The sound absorption coefficients considering the two material arrangements for the first and the second configuration of the proposed novel MPM structure are shown in Figs. 6.4(a) and 6.4(b) respectively. In order to illustrate the sound absorption enhancement by the proposed novel MPM structure, the sound absorption coefficients of the constituent porous materials as well as the DP materials without the inner porous material layer are also plotted for comparison. For the sake of simplicity, 'DP-m' is used to represent the DP material made with melamine foam B, while 'DP-r' is used to represent the DP material made with rockwool. As can be seen in both figures, the theoretical results agree very well with the numerical ones for the proposed novel porous composite structure with two different material arrangements. Hence, the developed theoretical models for both the LPC and HPC cases of the proposed novel MPM structure are appropriate for the accurate and efficient analysis of its sound absorption performance.

Fig. 6.4(a) shows the sound absorption coefficient curves for the novel MPM structure with Configuration 1 and two material arrangements. It can be seen that for the single porosity rockwool, the sound absorption coefficient increases with the increase of frequency and the maximum value is below 0.7 which is far from satisfactory. For the single porosity melamine foam, although the maximum value is above 0.9, it is located at around 1000Hz and at very low frequency of 300Hz, the coefficient is only about 0.64. Then for the DP material made of rockwool, the maximum sound absorption coefficient occurs at a relatively low frequency about 260Hz, but the absorption coefficient has a value higher than 0.9 only in a very narrow frequency range of about 60Hz, which is not beneficial to practical applications. As for the DP material made of melamine foam, the maximum sound absorption coefficient can reach nearly 1. However, this value appears at around 880Hz which is a quite high frequency. In contrast, the proposed novel MPM structure combining these two porous materials exhibits a much better sound absorption performance in several frequency ranges. As for the novel MPM structure with the melamine foam as the inner layer and the rockwool as the outer matrix, the first sound absorption peak can reach 0.979 at around 350Hz which is only a little bit higher than that in the DP case with rockwool while it still remains at a quite low frequency. Importantly, the sound absorption coefficient is higher than 0.9 in a much wider frequency range of about 320Hz. In addition, for the first configuration with the inverse material arrangement, the sound absorption peak occurs at around 540Hz with a value of 0.972 and the coefficient is larger than 0.9 from 340Hz on. For both material arrangements, the coefficient is above 0.8 from about 280Hz on with a very broad frequency range, which is very advantageous for practical engineering applications.

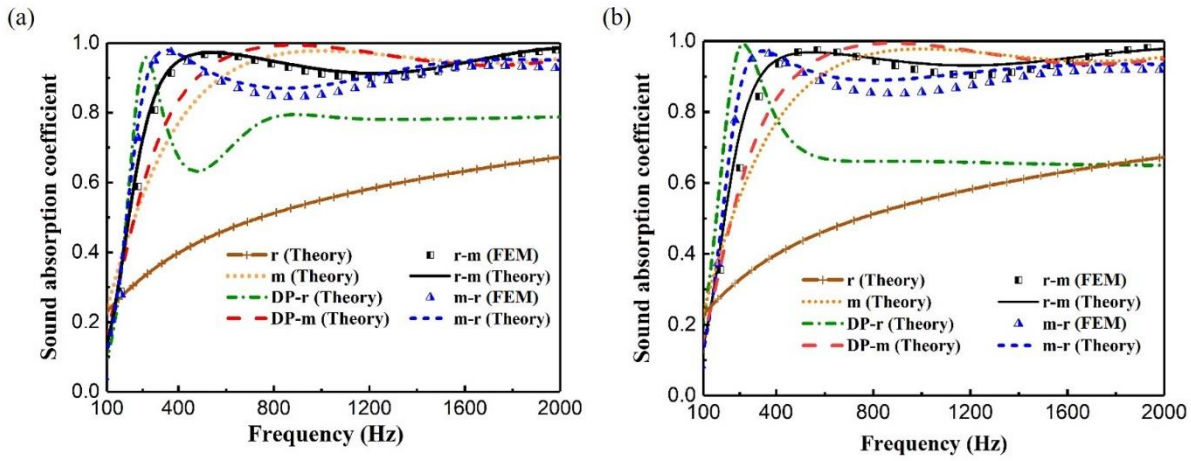

Fig. 6.4: Sound absorption coefficients for the novel MPM structure with two material arrangements. (a) Configuration 1, (b) Configuration 2.

Fig. 6.4(b) presents the sound absorption coefficient curves for the novel MPM structure with Configuration 2 and two material arrangements. The second material arrangement with rockwool as the inner layer and melamine foam as the outer matrix leads to the HPC case. However, the sound absorption peaks of the novel MPM structure with the two material arrangements don't show much difference compared with those in Fig. 6.4(a). The above analysis indicates that for the proposed novel MPM structure with a proper geometry, it is possible to obtain a high sound absorption performance at low frequencies even for the LPC case. On the contrary, for the conventional DP materials, the HPC case is usually necessary in order to have a satisfactory sound absorption coefficient. Generally speaking, through the comparison with conventional porous material and the DP material, the proposed novel MPM structure exhibits not only excellent low-frequency sound absorption performance but also a better global effect with a wider bandwidth.

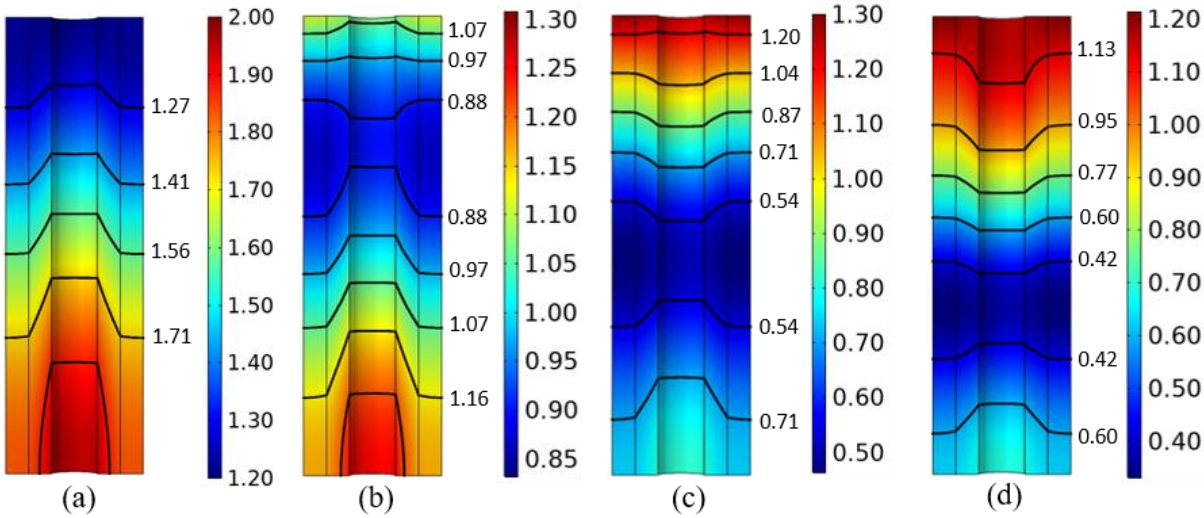

Fig. 6.5: Pressure field (Unit: Pa) in a UC with Configuration 1 and material arrangement "r-m". (a) f =300Hz, (b) f =500Hz, (c) f =1000Hz, (d) f =1500Hz.

In order to gain a deep insight into the sound absorption mechanism, the acoustic pressure field in the proposed novel MPM structure is investigated. For the sound incidence on the top surface of the structure, Figs. 6.5 and 6.6 show the pressure fields in the UC for the first geometrical configuration but with different material arrangements. The pressure distribution strongly depends on the frequency, so here four typical frequencies including 300Hz, 500Hz, 1000Hz and 1500Hz are selected to demonstrate the pressure distribution. As is shown in Fig. 6.5, at the very low frequency of 300Hz, the high sound pressure appears near the bottom part of the structure. This is because the acoustic waves at a lower frequency with a larger wavelength can easily penetrate through the structure into the bottom. A pressure gradient can be observed inside the rockwool region because its air flow resistivity is 10 times higher than that of the melamine foam, which makes it more difficult for the acoustic waves to pass through. However, at the high frequency of 1500Hz, the high-pressure field appears near the top surface region, since as the frequency increases the wavelength decreases and it gets harder for the acoustic waves to penetrate into the novel MPM structure. At intermediate frequencies of 500Hz and 1000Hz, the distributions of the pressure can be seen as combinations of that of 300Hz and 1500Hz.

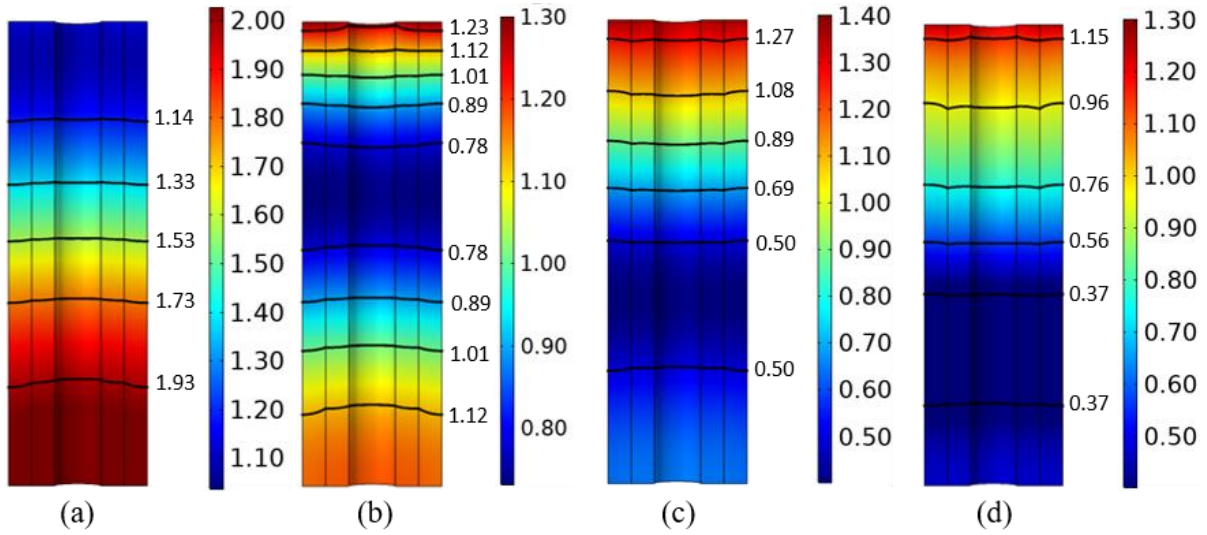

Fig. 6.6: Pressure field (Unit: Pa) in a UC with Configuration 1 and material arrangement "m-r". (a) f =300Hz, (b) f=500Hz, (c) f=1000Hz, (d) f=1500Hz.

The pressure field in the UC with the first configuration having inverse material arrangement is shown in Fig. 6.6. For this case the isobars are almost perpendicular to the thickness direction as the micro-porous material layer inside has a much lower air flow resistivity so no pressure gradient is generated. Similar to the previous case, at the low frequency of 300Hz, the high pressure locates in the bottom region of the porous composite structure. As the frequency increases, the high-pressure field moves to the top surface region of the porous composite structure due to the decrease of the wavelength.

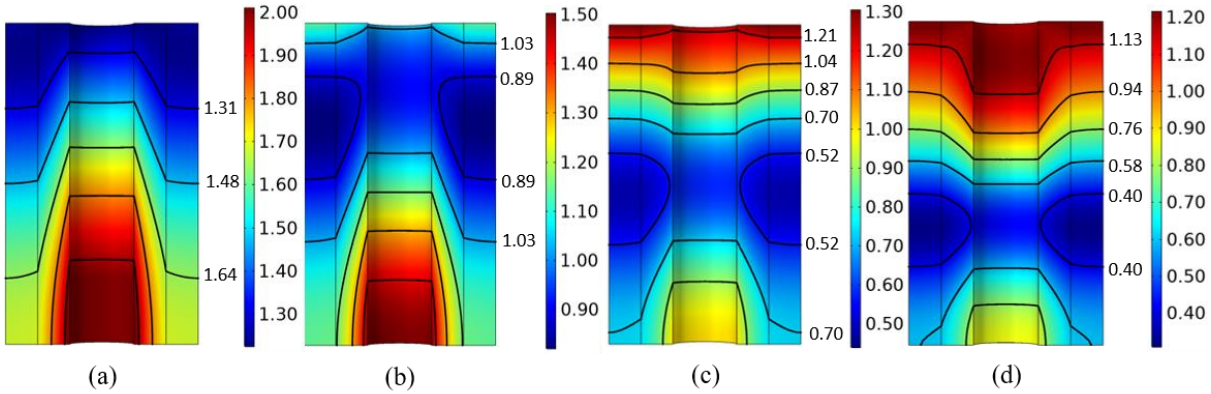

Fig. 6.7: Pressure field (Unit: Pa) in a UC with Configuration 2 and material arrangement "r-m". (a) f =300Hz, (b) f =500Hz, (c) f =1000Hz, (d) f =1500Hz.

The pressure fields in the porous composite structure of the second configuration with the two different material arrangements are shown in Figs. 6.7 and 6.8 respectively. It can be observed in Fig. 6.7 that the isobars change their directions remarkably at the interface between rockwool and the meso-pore. This is due to the fact that in the meso-pore domain the inertial force is dominant while in the inner rockwool layer the viscous force is dominant and these two different forces lead to the pressure diffusion effect. However, the pressure field in Fig. 6.8 is similar to that in Fig. 6.6 as both cases have the same material arrangement and belong to the LPC case. In general, for all the four considered cases, at low frequencies, the high-pressure field appears in the bottom part of the porous composite structure near the meso-pore domain and then it moves up to the top surface and concentrates in the upper part of the porous composite structure as the frequency increases.

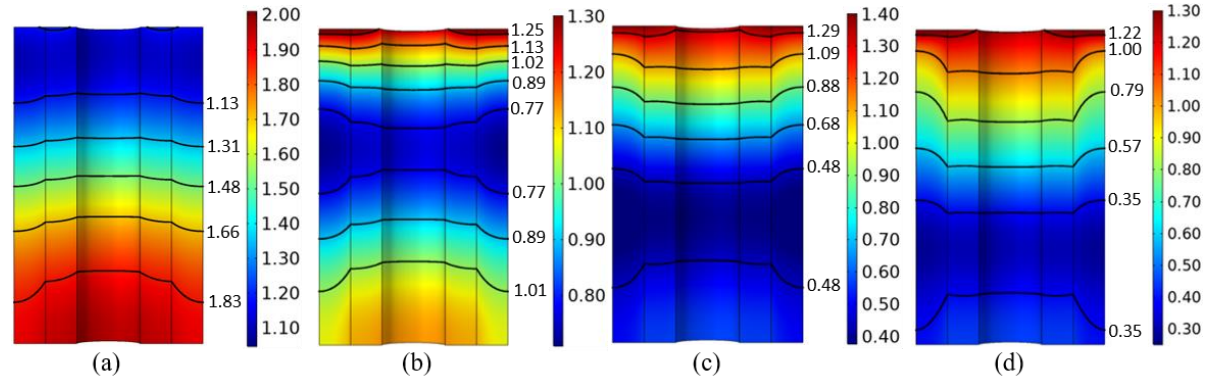

Fig. 6.8: Pressure field (Unit: Pa) in a UC with Configuration 2 and material arrangement "m-r". (a) f =300Hz, (b) f =500Hz, (c) f =1000Hz, (d) f =1500Hz.

We further explore the sound absorption mechanism from the perspective of the sound energy dissipation and the distributions of the time-averaged power dissipation density for the two geometrical

configurations with the two different material arrangements are shown in Figs. 6.9-6.12 respectively. Four typical frequencies of 300Hz, 500Hz, 1500Hz and 2000Hz are chosen. The total energy dissipated in each constituent porous material consists of two parts: the energy dissipated through the viscous effects and that through the thermal effects, and they can be determined from the wave propagation analysis in an equivalent fluid [39]. It can be observed in these four figures that the sound energy is mainly dissipated in different parts of the porous composite structure as the frequency changes, and it also varies with the material arrangement. As can be found in Figs. 6.9-6.12, for all the LPC cases, most of the energy is dissipated in the melamine foam at low frequencies and little energy is dissipated in rockwool. However, at high frequencies, the top part of the rockwool also participates in the energy dissipation. As for the HPC case, the general tendency for the energy dissipation is almost the same as LPC case, except that at very low frequency the bottom part of the rockwool also contributes much to the energy dissipation. In brief, the two porous materials play different roles for the consumption of the sound energy at different frequency ranges and the multiscale design of the porous composite structure can combine the advantage of the two materials which leads to a more efficient sound energy consumption.

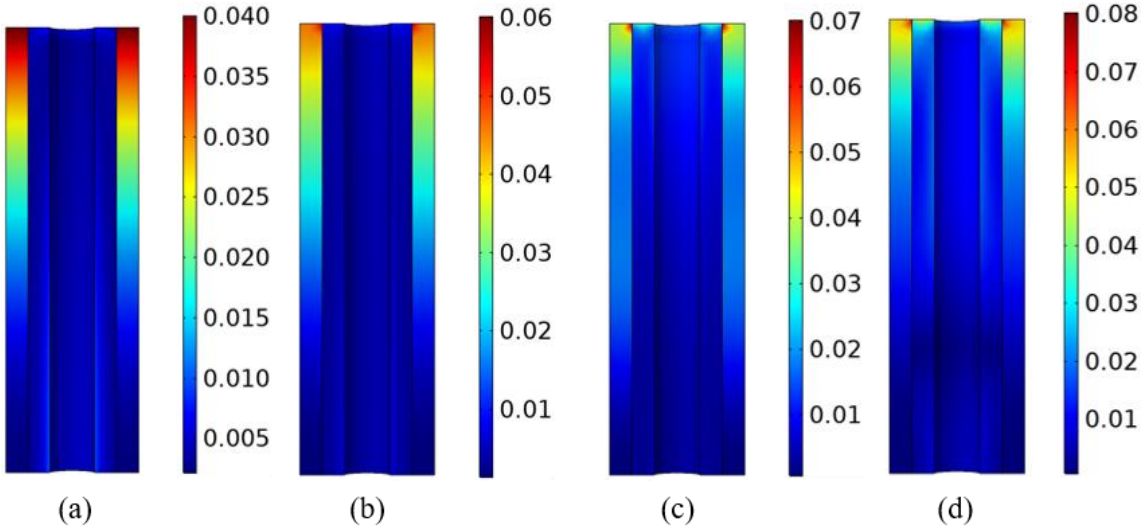

Fig. 6.9: Time-averaged power dissipation density (Unit: W/m^3) in a UC with Configuration 1 and material arrangement "r-m". (a) f=300Hz, (b) f=500Hz, (c) f=1500Hz, (d) f=2000Hz.

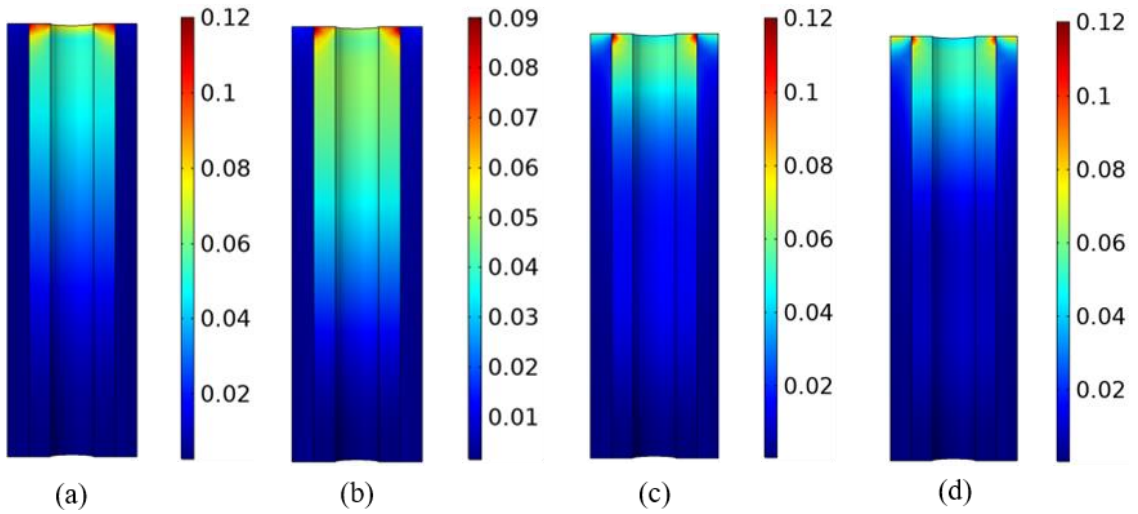

Fig. 6.10: Time-averaged power dissipation density (Unit: W/m^3) in a UC with Configuration 1 and material arrangement "m-r". (a) f=300Hz, (b) f=500Hz, (c) f=1500Hz, (d) f=2000Hz.

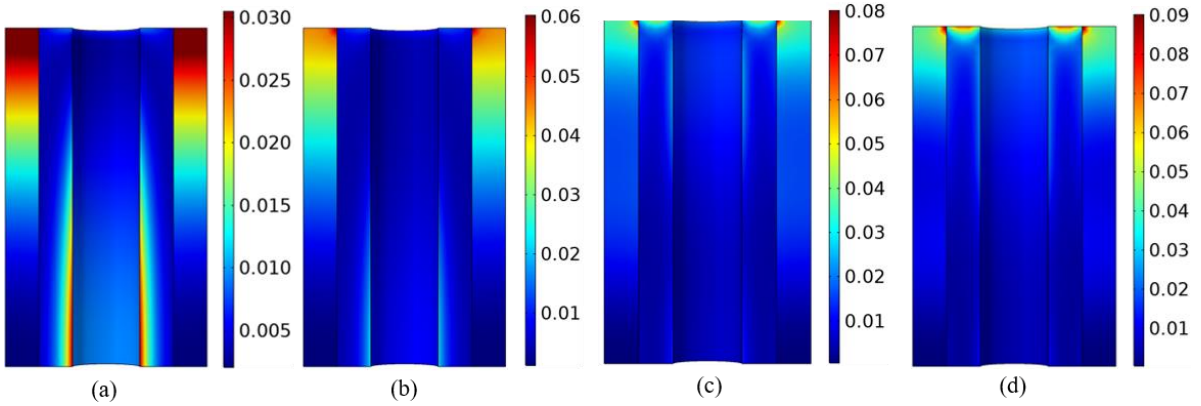

Fig. 6.11: Time-averaged power dissipation density (Unit: W/m^3) in a UC with Configuration 2 and material arrangement "r-m". (a) f=300Hz, (b) f=500Hz, (c) f=1500Hz, (d) f=2000Hz.

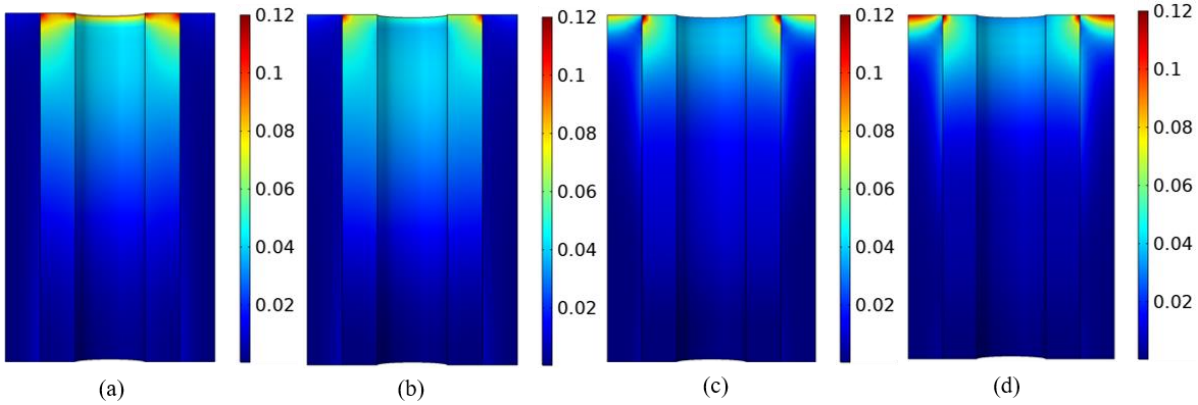

Fig. 6.12: Time-averaged power dissipation density (Unit: W/m^3) in a UC with Configuration 2 and material arrangement "m-r". (a) f=300Hz, (b) f=500Hz, (c) f=1500Hz, (d) f=2000Hz.

6.2.2 Parametrical analysis

6.2.2.1 Effects of the meso-pore size

Firstly, the effects of the meso-pore size of the novel MPM structure are investigated. In this subsection, we consider the novel MPM structure with two different porous materials having equal thickness so as to avoid the effects of the material proportion, and the same porous materials as in the previous section are used. The outer geometry of the whole UC remains unchanged with r_2 =15mm, h =100mm, while the radius of the meso-pore R_p and the outer radius of the inner material layer r_1 change correspondingly in order to satisfy the condition $r_1 - R_p = r_2 - r_1$. The geometrical parameters and the determination of the permeability contrast (PC) case with different meso-pore sizes for the two different material arrangements are presented in Tables 6.3 and 6.4 respectively.

Table 6.3: Geometrical parameters and determination of the PC case with different meso-pore sizes with material arrangement "r-m".

R_p (mm)	r_1 (mm)	r_2 (mm)	h (mm)	ω_{d1} (rad/s)	ω_{VM1} (rad/s)	Angular frequency range ω (rad/s)	Conditions of HPC	PC case
1	8.0	15	100	18262	49129	628-12566		HPC
2	8.5			27783				HPC
3	9.0			38377				HPC
4	9.5			51182			$\omega \ll \omega_{VM1}$	LPC
5	10.0			67467			$\omega_{d1} \ll \omega_{VM1}$	LPC
6	10.5			89094				LPC
7	11.0			119090				LPC
8	11.5			162750				LPC

As can be seen in Table 6.3, the considered frequencies are much lower than the viscous characteristic frequency ω_{VM1} of the micro-porous rockwool layer and when the radius of the meso-pore is sufficiently small (smaller than 3mm approximately), the characteristic frequency of the pressure diffusion effect ω_{d1} is also much lower than ω_{VM1}, which leads to an HPC case. However, for the case with an inverse material arrangement, no matter what meso-pore size we have, ω_{d1} is always much higher than the viscous characteristic frequency ω_{VM1} of the micro-porous melamine foam layer and hence all the considered cases belong to the LPC case. The corresponding results of the sound absorption coefficient are shown in Figs. 6.13(a) and 6.14(a) respectively. It can be observed in these

two figures that if the radius of the meso-pore is too small, it is unlikely to obtain a high sound absorption coefficient at low frequencies and there is no sound absorption peak. Meanwhile, as the meso-pore radius increases, the sound absorption peak value first increases and then decreases.

Table 6.4: Geometrical parameters and determination of the PC case with different meso-pore sizes with material arrangement "m-r".

R_p (mm)	r_1 (mm)	r_2 (mm)	h (mm)	ω_{d1} (rad/s)	ω_{VM1} (rad/s)	Angular frequency range ω (rad/s)	Conditions of HPC	PC case
1	8.0	15	100	221810	8444	628-12566	$\omega \ll \omega_{VM1}$	LPC
2	8.5			337460				LPC
3	9.0			466150				LPC
4	9.5			621680				LPC
5	10.0			819490			$\omega_{d1} \ll \omega_{VM1}$	LPC
6	10.5			1082200				LPC
7	11.0			1446500				LPC
8	11.5			1976800				LPC

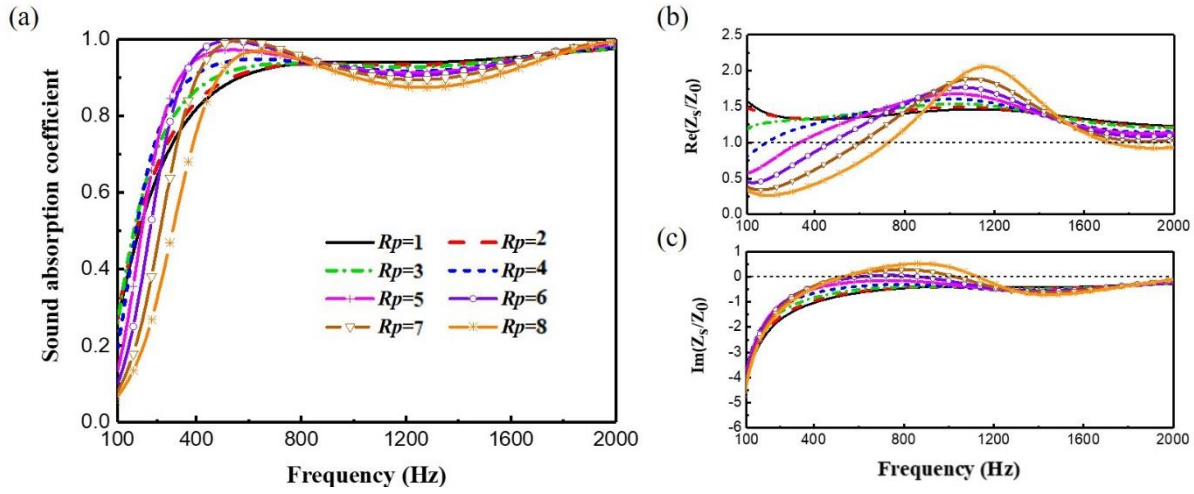

Fig. 6.13: Effects of the meso-pore size on the novel MPM structure with r_2 =15mm, h =100mm and material arrangement "r-m". (a) Sound absorption coefficient, (b) real part and (c) imaginary part of the surface impedance (Unit of R_p: mm).

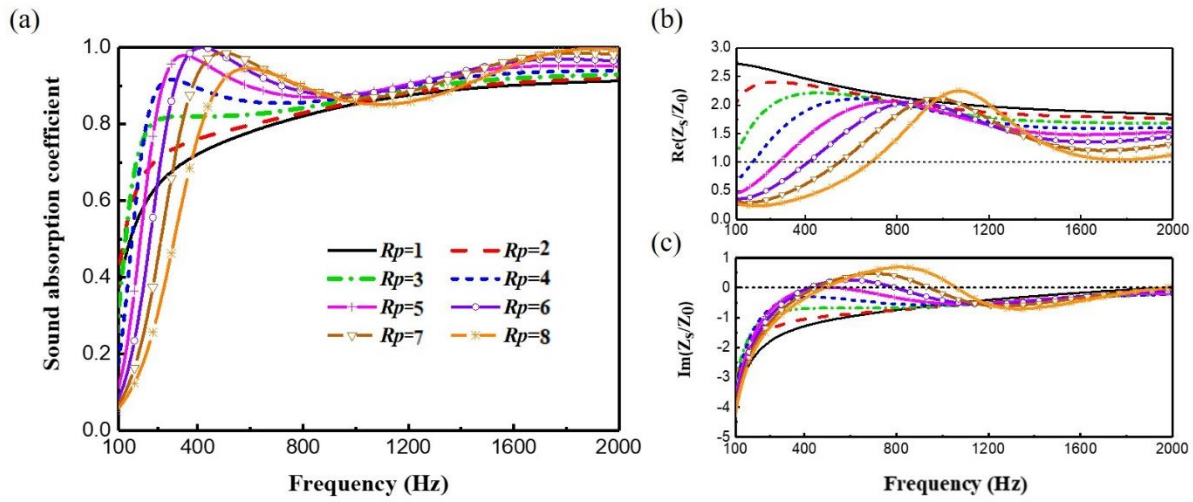

Fig. 6.14: Effects of the meso-pore size on the novel MPM structure with r_2 =15mm, h =100mm and material arrangement "m-r". (a) Sound absorption coefficient, (b) real part and (c) imaginary part of the surface impedance (Unit of R_p: mm).

6.2.2.2 Effects of the material composition ratio

Besides the above-mentioned geometrical parameter, altering the material composition ratio is also a convenient way to improve the sound absorption characteristics. In this subsection the two different material arrangements are studied while keeping the UC geometry unchanged with R_p=5mm, r_2=15mm, h =100mm and the parameter r_1 varies with the material composition ratio. For the sake of simplicity, we use "r:m" to represent the composition ratio of rockwool to melamine foam and "m:r" to denote the composition ratio of melamine foam to rockwool. Here, the composition ratio is defined by the ratio of the thicknesses of the two micro-porous material layers, which can be expressed as $\left(r_1 - R_p\right)/\left(r_2 - r_1\right)$. The results of the sound absorption coefficient for different material composition ratios are depicted in Figs. 6.15(a) and 6.16(a) respectively, and the surface impedances of the novel MPM structure are also presented in Figs. 6.15(b)-(c) and 6.16(b)-(c). It can be seen that the material composition ratio has a great influence on the sound absorption performance of the proposed MPM structure. Generally speaking, the sound absorption curve of the MPM structure can be regarded as a combination of the two curves for the corresponding DP materials, i.e., a single porous material with meso-pores. Besides, the proposed novel MPM structure with a higher rockwool fraction has a sound absorption peak at lower frequencies. In contrast, for the case with a higher fraction of melamine foam, no sound absorption peak can be found at low frequencies, while the coefficient is satisfactory at medium to high frequencies. With a proper material composition ratio, it is possible to obtain a very high sound absorption coefficient which can reach 1 at around 300Hz and the frequency range with a sound absorption coefficient higher than 0.9 can be largely broadened. Thus, the material composition ratio can be tailored to significantly

enhance the sound absorption performance.

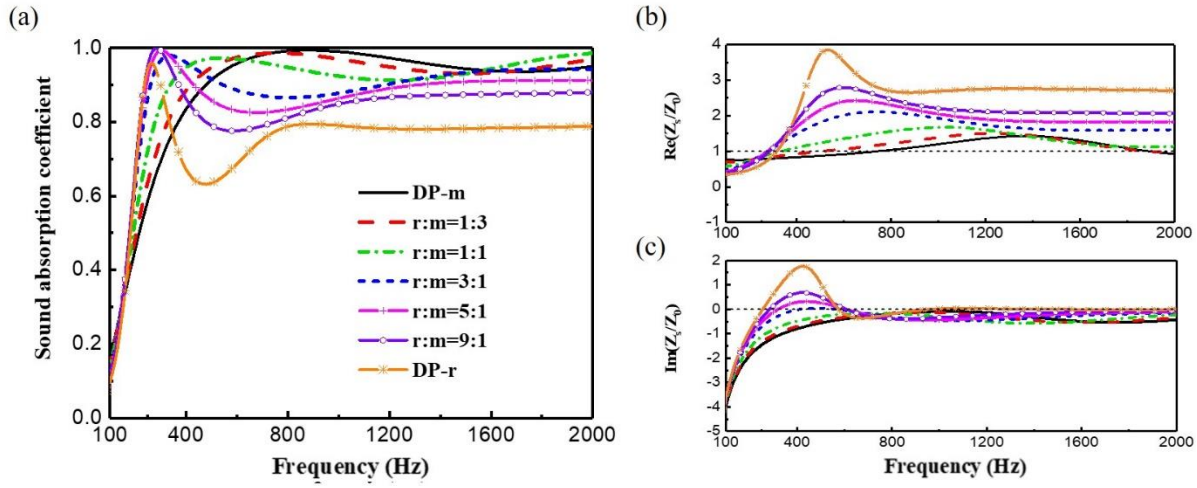

Fig. 6.15: Effects of the material composition ratio on the novel MPM structure with R_p =5mm, r_2 =15mm, h =100mm and material arrangement "r-m". (a) Sound absorption coefficient, (b) real part and (c) imaginary part of the surface impedance.

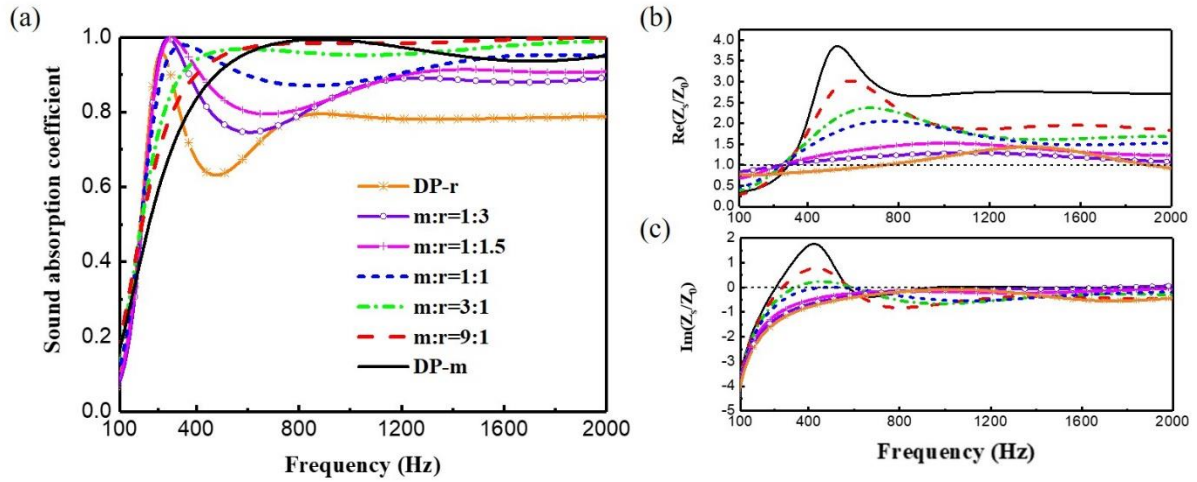

Fig. 6.16: Effects of the material composition ratio on the novel MPM structure with R_p =5mm, r_2 =15mm, h =100mm and material arrangement "m-r". (a) Sound absorption coefficient, (b) real part and (c) imaginary part of the surface impedance.

6.2.2.3 Effects of the thickness

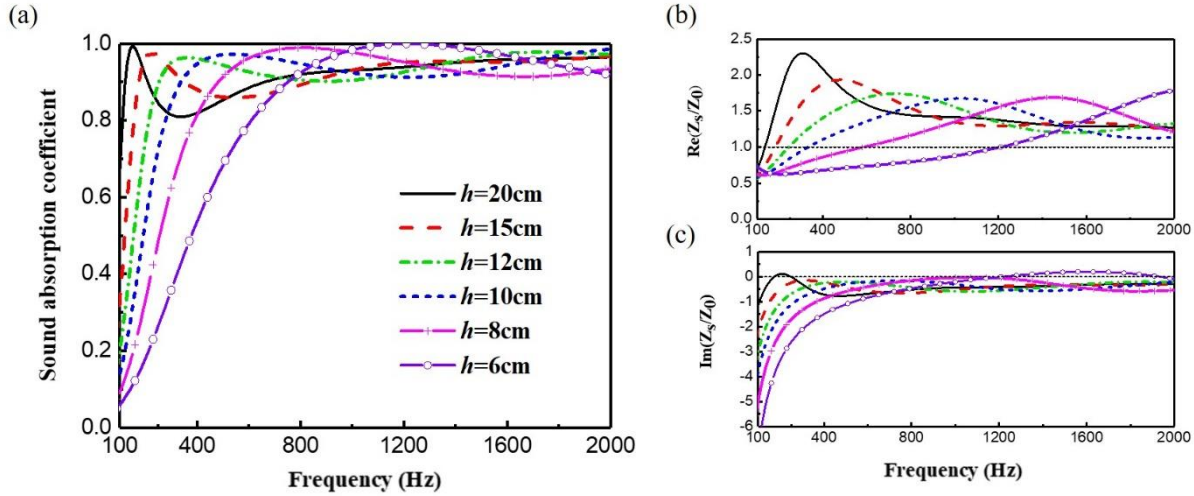

Fig. 6.17: Effects of the thickness of the novel MPM structure with R_p =5mm, r_1 =10mm, r_2 =15mm and material arrangement "r-m". (a) Sound absorption coefficient, (b) real part and (c) imaginary part of the surface impedance.

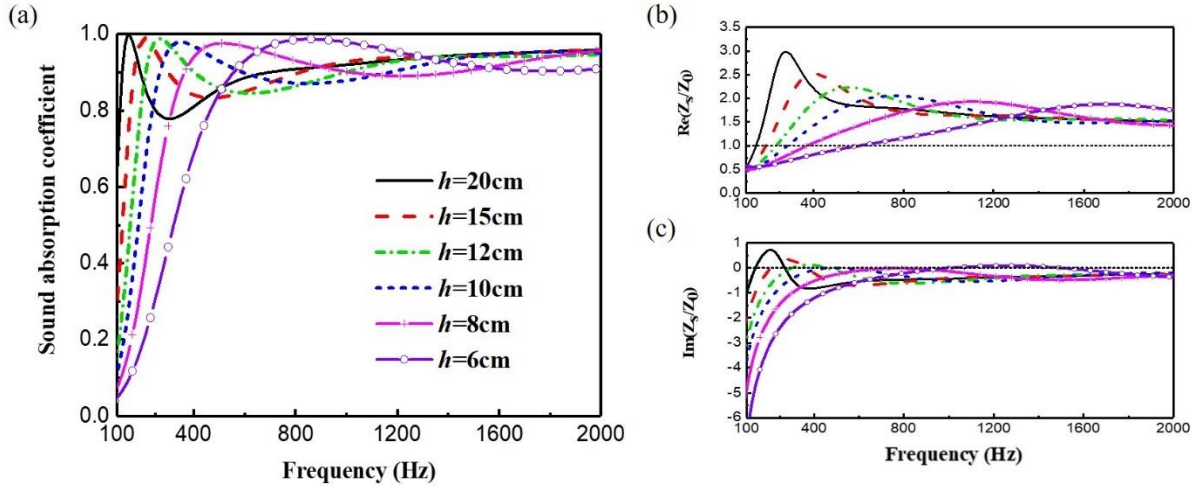

Fig. 6.18: Effects of the thickness of the novel MPM structure with R_p =5mm, r_1 =10mm, r_2 =15mm and material arrangement "m-r". (a) Sound absorption coefficient, (b) real part and (c) imaginary part of the surface impedance.

Finally, the effects of the thickness of the porous composite structure h are studied. The cross-sectional sizes of the UC are the same as Configuration 1, while the sample thickness h varies. Since h is not involved in the calculation of the characteristic frequency of the pressure diffusion effect ω_{d1} and the viscous characteristic frequency of the inner porous material layer ω_{VM1}, all the cases studied in this

part belong to the LPC case. The corresponding sound absorption coefficients and the real and imaginary parts of the surface impedance of the porous composite structure with different thicknesses and the two different material arrangements are shown in Figs. 6.17(a)-(c) and 6.18(a)-(c) respectively. It is observed that the thickness of the porous composite structure can remarkably change the sound absorption peak for both material arrangements. When the thickness of the porous composite structure increases, the position of the sound absorption peak shifts to lower frequencies but with a narrower sound absorption bandwidth, meanwhile the sound absorption curve becomes more fluctuated, which can also be explained by the aforementioned surface impedance matching theory.

6.2.3 Oblique wave incidence

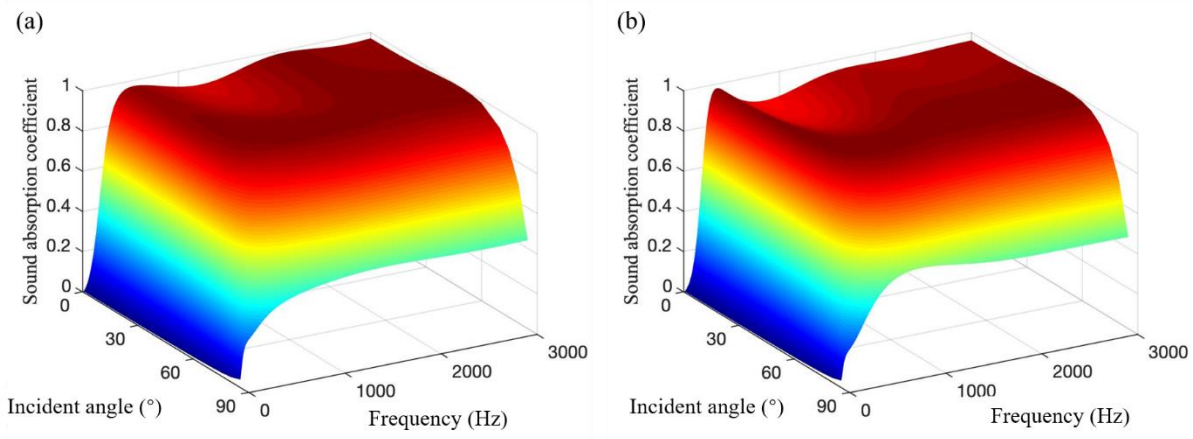

Fig. 6.19: Sound absorption coefficient with different incident angle for Configuration 1 with the material arrangement of (a) “r-m” and (b) “m-r”.

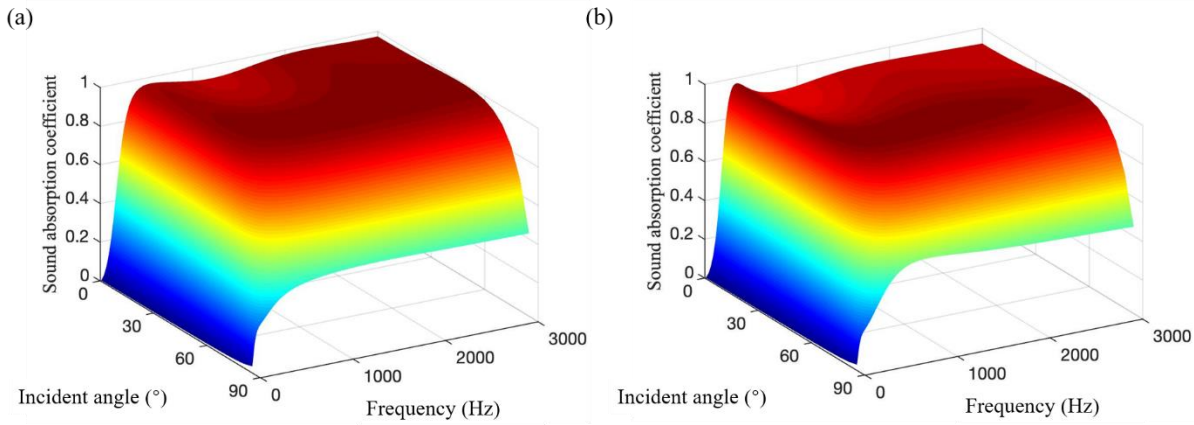

Fig. 6.20: Sound absorption coefficient with different incident angle for Configuration 2 with the material arrangement of (a) “r-m” and (b) “m-r”.

In this subsection the obliquely incident acoustic wave is considered, with $\theta = 0°$ representing the normally incident wave. For the theoretical calculation, the equivalent dynamic mass density and equivalent bulk modulus of the novel MPM remain the same as the case with normal incidence since they are independent on the incident wave, and only the calculation of the surface impedance and the sound absorption coefficient changes. The results for the sound absorption coefficient of the novel MPM structure with various incident angles considering 2 configurations and material arrangements are shown in Figs. 6.19 and 6.20. For Configuration 1 with material arrangement "r-m", the maximum sound absorption coefficient can be found at 880Hz with an incident angle of 50° and the value is 0.9982, while for inverse material arrangement it can be found at 510Hz with an incident angle of 55° and the value is 0.9998. For Configuration 2 with "r-m", it is found at 980Hz with an incident angle of 50° and the value is 0.9991, while for the inverse material arrangement, it can be found at 780Hz with an incident angle of 60° and the value is 0.9999. Generally speaking, regardless of the geometrical parameters or material arrangement, the frequency of the sound absorption coefficient peak is always the lowest at normally incident acoustic wave. With the increase of the incident angle, the sound absorption peak gradually moves to a higher frequency and this peak value first increases then decreases. Besides, the increase of the incident angle will lead to a smoother sound absorption curve.

6.2.4 High temperature effects

The acoustic energy absorption characteristics of the novel MPM structure and the underlying physical mechanism under high temperature are studied in details in this subsection. In our calculations, the cylindrical UC of the porous metamaterial structure has the following geometrical parameters: R_p=4mm, r_1=8mm, r_2=12mm and h =90mm. Two porous materials made of SMF and rockwool are used and their material parameters at different temperatures are shown in the last chapter. In the following analysis, the porous material SMF is taken as the inner porous interlayer and rockwool as the outer porous matrix.

The sound absorption coefficient and the surface impedance (normalized by the characteristic impedance of air) curves are shown in Fig. 6.21. It can be observed here that fairly good agreements between the theoretical and numerical results are achieved, which validates the theoretical model established. At room temperature, the sound absorption coefficient is above 0.8 starting from a low frequency of about 270Hz on, and the peak is located at around 390Hz with a value of about 0.986. At 100°C, the sound absorption coefficient is above 0.8 from 290Hz on, while at 300°C, the coefficient is above 0.7 from 340Hz on. As mentioned in the last chapter, for a perfect sound energy absorber [151], it requires that the real part of the surface impedance of the structure (acoustic resistance) equals to that of air (i.e., $\mathrm{Re}(Z_s/Z_0)=1$) and the imaginary part of the surface impedance (acoustic reactance) equals to zero (i.e., $\mathrm{Im}(Z_s/Z_0)=0$). As temperature rises, the peak position only slightly shifts to a higher frequency by several dozens of Hz and the peak value always remains higher than 0.985, which can be explained

by the excellent impedance match between the novel MPM structure and air. However, in the intermediate frequency range, with the increase of the temperature, the acoustic resistance deviates farther away from 1, which leads to a poor match of the surface impedance with the impedance of air. Thus, the sound absorption coefficient decreases and a trough can be observed around 1000Hz. Nevertheless, it can still be concluded that the sound energy absorption is sufficiently efficient at very low frequencies with a large bandwidth at high temperature.

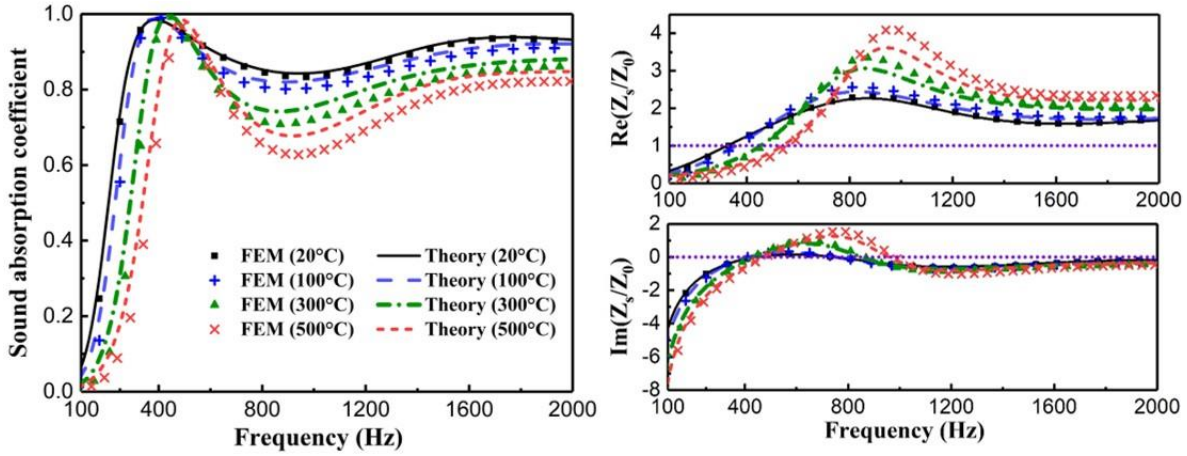

Fig. 6.21: (a) Sound absorption coefficient, (b) real part and (c) imaginary part of the normalized surface impedance curves at different temperatures.

To demonstrate the sound absorption performance of the novel MPM structure, the comparison of the sound absorption coefficients for the novel MPM structure, the DP materials (porous materials with cylindrical holes) and the single porosity materials having the same geometry is shown in Fig. 6.22. Here, SMF and r are used to represent the single porosity materials made with sintered metallic fibres and rockwool respectively, while DP-SMF and DP-r are used to represent the DP materials with cylindrical holes but without additional interlayers. It can be observed from Fig. 6.22 that for the two pristine porous materials without cylindrical holes, with the increase of temperature, the sound absorption coefficients decrease significantly and become inefficient. Among the other three cases with cylindrical holes, a peak in the sound absorption coefficient is induced in the low-frequency range. At the same temperature, the peak value of the sound absorption coefficient for DP-r is smaller than that for the novel porous metamaterial structure and the one for the DP-SMF, and it appears always at the lowest frequency. The peak value of the sound absorption coefficient for the novel porous metamaterial structure is comparable with that of DP-SMF at $20^{\circ}C$ and $500^{\circ}C$, but higher than that for DP-SMF at $100^{\circ}C$ and $300^{\circ}C$. The peak position of the sound absorption coefficient for the novel metamaterial structure only shifts slightly to a higher frequency compared with that for DP-r, and it lies between the two corresponding frequencies for DP-SMF and DP-r. As temperature increases, despite the decrease

in the sound absorption peak position for DP-SMF, it can only reach about 560 Hz at the lowest, which is still higher than that for the proposed porous metamaterial structure and the one for DP-r. Fig. 6.22 shows clearly that the proposed novel MPM structure exhibits an improved sound absorption capacity in the low-frequency range, while the single porosity SMF and the DP material DP-SMF perform better in the intermediate-frequency range, at least for the considered temperature interval.

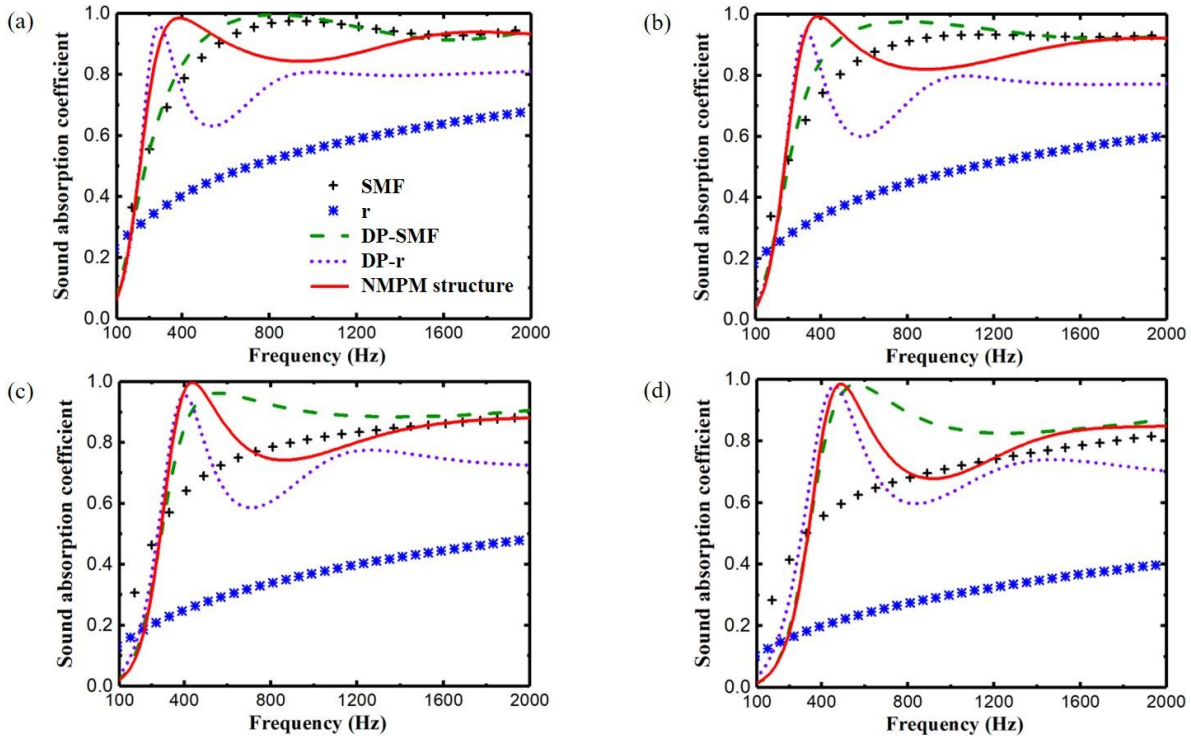

Fig. 6.22: Comparison of the sound absorption coefficients for (a) $t = 20^{\circ}\mathrm{C}$, (b) $t = 100^{\circ}\mathrm{C}$, (c) $t = 300^{\circ}\mathrm{C}$, (d) $t = 500^{\circ}\mathrm{C}$.

To unveil the underlying mechanism of acoustic wave energy absorption, the distributions of time-averaged power dissipation density inside the UC of porous metamaterial structure are shown in Fig. 6.23. Five different frequencies are chosen, among which 390Hz, 440Hz and 500Hz are the sound absorption peak frequencies of the porous metamaterial structure at 100°C, 300°C and 500°C, respectively. The calculation of the total energy dissipated in each constituent porous material is the same as mentioned previously. As shown in Fig. 6.23, most of the energy is dissipated in the upper part of the inner porous interlayer SMF with a lower airflow resistivity, independent of the considered temperature. However, the porous matrix rockwool becomes more involved in the energy dissipation as the frequency increases, and a concentration of the dissipated energy can always be observed at the interface of the two different porous materials near the top surface at 2000Hz. Besides, it can be seen that the energy dissipation is minimal at 1000Hz for all four considered temperatures, which corresponds to the trough of the sound absorption coefficient curves in Fig. 6.21 approximately.

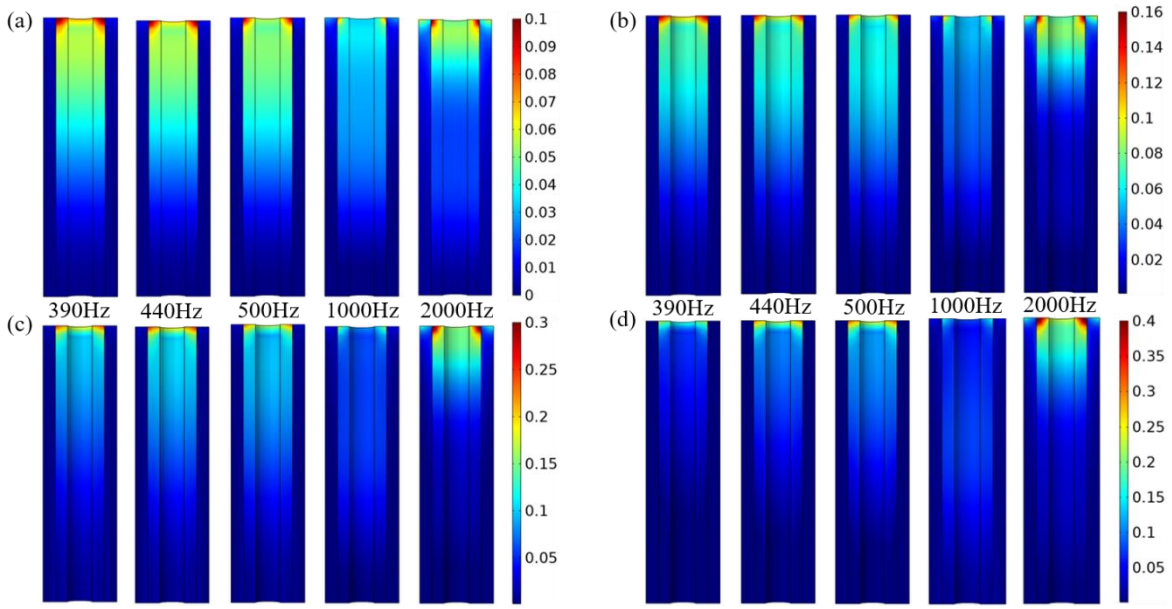

Fig. 6.23: Time-averaged power dissipation density (unit: $\mathrm{W/m^3}$) in a UC of the porous metamaterial structure for (a) $t = 20^{\circ}\mathrm{C}$, (b) $t = 100^{\circ}\mathrm{C}$, (c) $t = 300^{\circ}\mathrm{C}$, (d) $t = 500^{\circ}\mathrm{C}$.

In addition to illustrating the distribution of time-averaged power dissipation density within the UC of the porous metamaterial structure, Fig. 6.24 includes plots of the energy dissipation ratio at the four selected temperatures. This presentation aims to elucidate the contribution of each constituent porous material to the process of sound energy absorption. The curves in Fig. 6.24 represent the proportion of the energy dissipated in each constituent porous material to the total energy dissipated inside the whole UC of the porous metamaterial structure. It can be observed that regardless of the temperature, most of the energy is dissipated in the interlayer made of the SMF as the ratio is always higher than 0.5. For all four considered temperatures, the energy dissipated in the interlayer SMF first increases and the maximum ratio is around 0.8, which indicates that about 80% of the total dissipated energy is dissipated in the interlayer made of SMF. However, the energy dissipated in the interlayer made of SMF is reduced at intermediate and high frequencies, while the curves for the porous matrix rockwool shows an opposite trend. In summary, in the considered frequency range, the porous material with a lower airflow resistivity (SMF) contributes more to the energy dissipation regardless of the temperature, while the contribution of the porous material with a higher airflow resistivity (rockwool) also becomes more remarkable at intermediate to high frequencies.

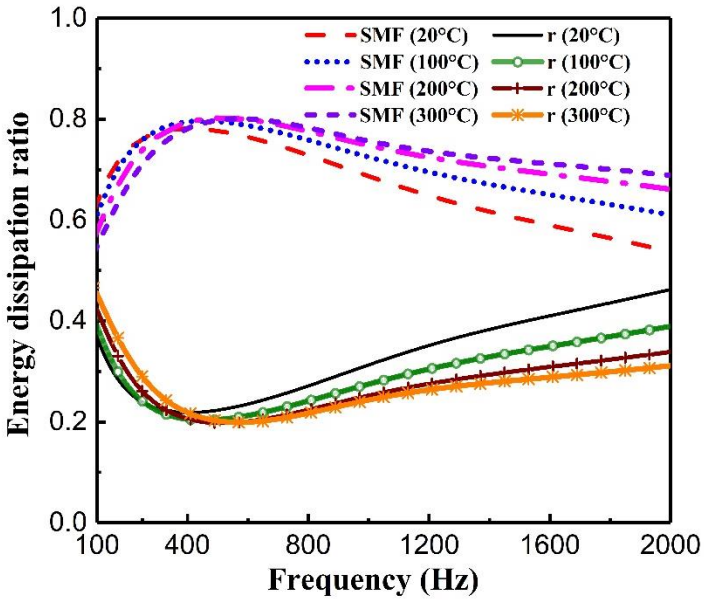

Fig. 6.24: Energy dissipation ratio of the two constituent porous materials at different temperatures.

6.3 Conclusions

In this chapter, a novel MPM is proposed and its acoustic wave absorption characteristics are studied in details. The novel MPM structure consists of a porous matrix with periodically distributed meso-pores in a square or hexagonal pattern, and another porous layer is attached to the inner walls of the meso-pores. The sound absorption coefficient of the novel MPM structure is studied considering two configurations and two possible material arrangements using rockwool and melamine foam as the two constituent porous materials. The results demonstrate the advantages of the novel MPM structure, including the enhancement of the sound absorption at low-to-medium frequencies and the broadening of the frequency range for achieving high sound absorption coefficients. The pressure distribution and the time-averaged dissipation power density are demonstrated to further explore the acoustic wave absorption mechanism of the MPM structure.

Then the effects of some important parameters are explored, including the size of the meso-pore, material composition ratio and the thickness of the structure. By adjusting these parameters, a more effective matching of the acoustic impedance can be achieved, thereby leading to a further enhancement in sound absorption.

Besides, the sound absorption coefficient at different incident angles is studied and a 3D graph shows explicitly how the sac varies as the incident angle changes. Generally speaking, regardless of the geometrical parameter or material arrangement, the frequency of the sound absorption coefficient peak is always the lowest at normal incident acoustic wave. With the increase of the incident angle, the sound

absorption peak gradually moves to a higher frequency and this peak value first increases then decreases. Besides, the increase of the incident angle will lead to a smoother sound absorption coefficient curve.

Finally, the impact of high temperatures is taken into consideration. The present results demonstrate that the proposed novel porous metamaterial structure exhibits a superior high-temperature acoustic energy absorption performance at low frequencies and in a rather wide frequency range. In-depth investigations are conducted on the distribution of the time-averaged power dissipation density in the UC as well as the energy dissipation ratio of each constituent porous material at different temperatures, which reveal that the two constituent porous materials contribute distinctively to the energy dissipation across different frequency ranges, and the majority of the energy is dissipated in the porous material with a lower airflow resistivity irrespective of the temperature.

7. Conclusions and outlook

7.1 Summary of the main research works

The main objectives of this thesis are set to investigate the acoustic wave propagation characteristics in porous metamaterials (PM) and to design novel PM structures with low-frequency broadband acoustic absorption and mitigation performance, where the high-temperature effects should be also taken into consideration. The former is achieved through the establishments of appropriate theoretical models and numerical methods as well as the study of the band structures and transmission spectra of the PM structures, while the latter is accomplished by designing and investigating two distinct PM structures, namely the slit-perforated multi-layered porous metamaterial (SMPM) structure and the novel multiscale porous metamaterial (MPM) structure.

To describe the macroscopic dynamic properties of the porous materials, theoretical models based on the homogenization schemes and the semi-phenomenological approaches are established and adopted to determine the effective equivalent dynamic material parameters, which are presented in Chapter 2. Since no analytical solutions for the acoustic wave propagation problems considered in this thesis are available, accurate and efficient numerical methods are adopted as described in Chapter 3. In particular, the transfer matrix method (TMM) and the finite element method (FEM) are applied in this thesis due to their reliability and convenience for calculating the band structures, the transmission spectra, and the acoustic wave absorption coefficient.

Based on the developed theoretical models and numerical methods, the band structures of different 1D PM structures are studied in Chapter 4. Specifically, slit-perforated porous metamaterial (SPM), porous composite metamaterial (PCM) and slit-perforated multi-layered porous metamaterial (SMPM) structures are examined in details. The band structures and the transmission spectra are computed and analyzed using the TMM and the FEM. For the SPM and PCM structures, the band structures and the transmission spectra or frequency responses are computed by the TMM considering different material compositions. The transmission spectra agree well with the band structures. The bandgaps are determined by the band structures calculated by adopting the fictitious material properties considering only the real parts of the equivalent dynamic mass density and bulk modulus, which is further verified by the pressure distribution inside the SPM and PCM structures computed by the FEM. Smooth boundaries of the bandgaps in the real part of the band structures are observed, which are induced by the imaginary parts of the effective dynamic material parameters and can be explained by the Taylor expansion of the frequency dispersion relation. The imaginary part of the band structures exhibits a notable distinction from the conventional metamaterials, where the acoustic wave attenuation is confined solely within the bandgaps. For porous metamaterials investigated in this thesis, acoustic wave

attenuation beyond the bandgaps is evident due to the viscous or damping effects, which are characterized by the imaginary parts of the effective dynamic material parameters or the imaginary part of the wave vector. This acoustic wave attenuation property outside of the bandgaps is more advantageous and beneficial for practical applications. Parametric analysis indicates that, for both SPM and PCM structures, the first frequency bandgap is widest when the two constituent porous materials have equal widths. Additionally, the aluminium foam, which exhibits a stronger impedance mismatch with air, primarily contributes to the first bandgap generation, while the SMF and glass wool contribute to the acoustic wave attenuation in the entire frequency range under consideration. The band structures of the SMPM structure are computed by using the TMM and the FEM, demonstrating consistent results that mutually validate both computational methods each other. In contrast to the SPM and PCM structures, the arrangement of the constituent porous materials becomes a significant factor for the SMPM structures. In addition, the impacts of the geometrical parameters on the band structures and the transmission spectra are explored.

In Chapter 5, the slit-perforated multi-layered porous metamaterial (SMPM) structure is proposed and its acoustic wave absorption characteristics for the acoustic waves incident perpendicular to the direction of the periodicity of the structure are studied thoroughly. The SMPM structure is composed of periodically arranged porous matrix layers and adjacent second-type porous layers with slits. Compared to the DP materials, the proposed SMPM structure exhibits a significantly enhanced sound absorption performance for normally (perpendicularly to the direction of the periodicity) incident acoustic waves. The underlying sound absorption mechanism is explored by analyzing the distribution of the time-averaged power dissipation density and the energy dissipation ratio of the constituent porous materials. The results indicate that the porous material with a low air-flow resistivity primarily contributes to the sound absorption at low frequencies, while the porous material with a high air-flow resistivity becomes more influential at medium to high frequencies. Furthermore, the effects of the two key parameters, namely the slit-width and the material composition ratio, are analysed. The introduction of slits will induce a sound absorption peak within the considered frequency range, but an excessive slit-width will lead to fluctuations in the sound absorption curve and a gradual shift of the peak frequency towards higher frequencies. The highest sound absorption coefficient of approximately 0.999 is observed at 410 Hz for sintered metallic fibrous material and green foam as constituent materials. Regarding the material composition ratio, a higher proportion of the porous material with a higher air flow resistivity result in a lower peak frequency. In addition, the sound absorption coefficients for various incidence angles considering two different material arrangements of the SMPM structure are exhibited. Three-dimensional (3D) diagrams illustrate that the peak frequency gradually increases as the incidence angle rises, while the peak value initially increases and then decreases. Moreover, an increase in the incidence angle leads to a smoother sound absorption curve. Finally, the acoustic wave absorption characteristics of the SMPM structure under high-temperature conditions are also studied.

With increasing temperature, the sound absorption peak shifts to higher frequencies, and the sound absorption curve becomes more fluctuating, resulting in a diminished overall performance.

In Chapter 6, the novel multi-scale porous metamaterial (MPM) structure is presented and its sound absorption characteristics are investigated comprehensively. The novel MPM structure comprises a porous matrix with periodically distributed meso-pores in a square or hexagonal pattern, accompanied by an additional porous layer attached to the inner walls of the meso-pores. By employing the rockwool and melamine foam as the constituent porous materials and considering two different material arrangements, the advantages of the novel MPM structure are demonstrated, namely their enhanced sound absorption performance at low-to-medium frequencies and an extended frequency range for achieving high sound absorption coefficients. In addition, the influences of several key parameters, including the meso-pore size, material composition ratio, and structure thickness are investigated. Adjusting these parameters enables a better match of the acoustic impedances, which can lead to a further improvement of the sound absorption capacity. Moreover, the sound absorption coefficient for different incidence angles is investigated, and a 3D graph illustrating the variation of the sound absorption coefficient with the incidence angles is presented. Generally, regardless of the geometry or material arrangement, the frequency of the sound absorption coefficient peak is lowest for normally (perpendicularly to the direction of the periodicity) incident acoustic waves. As the incidence angle increases, the sound absorption peak gradually shifts to higher frequencies, exhibiting an initial increase followed by a decrease. Furthermore, an increase in the incidence angle results in a smoother sound absorption curve. Lastly, the acoustic wave absorption characteristics of the novel MPM structure at high temperatures are explored. The results demonstrate that the proposed novel MPM structure exhibits a superior high-temperature acoustic wave absorption performance at low frequencies and in a wide frequency range. The detailed investigations on the distribution of the time-averaged power dissipation density within the UC and the energy dissipation ratio of each constituent porous material reveal that the two different porous materials contribute distinctly to the acoustic wave energy dissipation in different frequency ranges, where the porous material possessing a lower airflow resistivity dissipates the majority of the acoustic wave energy at low frequencies regardless of the temperature.

The research results and the knowledge achieved in this thesis may provide highly valuable guidelines for the design and optimization of novel acoustic metamaterials and structures, and thus promote their feasible realization and promising engineering applications for the efficient acoustic wave absorption, mitigation and isolation.

7.2 Outlook on the future research works

Acoustic wave absorption, mitigation and isolation have important applications in diverse engineering

disciplines. Despite the comprehensive research works conducted in this thesis on the acoustic wave absorption and mitigation characteristics in porous metamaterials and structures, additional investigations and improvements are still required. In particular, the following future research demands should be mentioned:

1) Experimental verifications of the acoustic wave absorption and mitigation characteristics of the proposed porous metamaterials and structures. In this thesis, only the theoretical modeling and the numerical simulation are conducted and no experiments are performed. Thus, in the future works, experiments should be carried out to further verify the obtained results and knowledge.

2) Modeling of porous materials with elastic frames. In this thesis, the assumption of rigid motionless skeletons for porous materials is adopted. Nonetheless, the more precised Biot theory should be applied in future for the acoustic wave propagation analysis in porous metamaterials and structures with elastic frames, which is more complicated but more accurate and realistic.

3) Design and investigation of novel three-dimensional (3D) porous metamaterials and structures. In this thesis, the TMM is empolyed exclusively for 1D porous metamaterials and structures, while the FEM is applied for 2D porous metamaterials and structures. In future research works, novel 3D porous metamaterials and structures should be designed and investigated.

4) Multiphysics field analysis considering the coupling of the acoustic waves and elastic waves. In this thesis, only the acoustic wave propagation characteristics in porous materials are assessed. However, in practice, the coupling between the acoustic waves and elastic waves is highly prevalent and merits further investigations, which can be realized by taking the fluid(air)-structure interaction into account.

5) Optimization of the porous metamaterials and structures. Although the effects of numerous geometrical and material parameters on the acoustic wave absorption and mitigation characteristics in porous metamaterials and structures are studied in this thesis, their optimization by adequate optimization (OP) algorithms or neural network (NN) and machine learning (ML) techniques is highly promising and desirable.

References

[1] Hu Z, Xu G, Shi Y, Xia R. Airfoil–vortex interaction noise control mechanism based on active flap control. Journal of Aerospace Engineering 2022 35(1):04021111.

[2] Dubbioso G, Muscari R, Ortolani F, Di Mascio A. Numerical analysis of marine propellers low frequency noise during maneuvering. Part II: Passive and active noise control strategies. Applied Ocean Research 2022 125:103201.

[3] Lee HM, Hua Y, Wang Z, Lim KM, Lee HP. A review of the application of active noise control technologies on windows: Challenges and limitations. Applied Acoustics 2021 174:107753.

[4] Hu S, Hu W, Yang S, Zhu X, Sun K, Jiang S, et al. Investigation on noise exposure level and health status of workers in transportation equipment manufacturing industry. Chinese Journal of Industrial Hygiene and Occupational Diseases 2021 39(7):498-502.

[5] Hansen CH, Hansen KL. Noise control: From Concept to Application: CRC Press, 2021.

[6] Organization WH. Burden of disease from environmental noise: Quantification of healthy life years lost in Europe: World Health Organization. Regional Office for Europe, 2011.

[7] Cao L, Fu Q, Si Y, Ding B, Yu J. Porous materials for sound absorption. Composites Communications 2018 10:25-35.

[8] Sakagami K, Morimoto M, Yairi M. Application of microperforated panel absorbers to room interior surfaces. International Journal of Acoustics and Vibration 2008 13(3): 120-124.

[9] Arenas JP, Crocker MJ. Recent trends in porous sound absorbing materials. Sound & Vibration 2010 44(7):12-18.

[10] Yang M, Sheng P. Sound absorption structures: From porous media to acoustic metamaterials. Annual Review of Materials Research 2017 47(1):83-114.

[11] Komkin A I, Mironov M A, Bykov A I. Sound absorption by a Helmholtz resonator. Acoustical Physics 2017 63:385-392.

[12] Cai C, Mak CM. Noise attenuation capacity of a Helmholtz resonator. Advances in Engineering Software 2018 116:60-66.

[13] Sagartzazu X, Hervella-Nieto L, Pagalday J. Review in sound absorbing materials. Archives of Computational Methods in Engineering 2008 15(3):311-342.

[14] Tang P K, Sirignano W A. Theory of a generalized Helmholtz resonator. Journal of Sound and Vibration 1973 26(2):247-262.

[15] Howe M S. On the Helmholtz resonator. Journal of Sound and Vibration 1976 45(3):427-440.

[16] Maa DY. Theory and design of microperforated panel sound-absorbing constructions. Sci Sin 1975 18:55-71.

[17] Maa DY. Potential of microperforated panel absorber. The Journal of the Acoustical Society of America 1998 104(5):2861-2866.

[18] Kang J, Brocklesby MW. Feasibility of applying micro-perforated absorbers in acoustic window systems. Applied Acoustics 2005 66(6):669-689.

[19] Liu J, Herrin DW. Enhancing micro-perforated panel attenuation by partitioning the adjoining cavity. Applied Acoustics 2010 71(2):120-127.

[20] Wang C, Huang L. On the acoustic properties of parallel arrangement of multiple micro-perforated panel absorbers with different cavity depths. The Journal of the Acoustical Society of America 2011 130(1):208-218.

[21] Qian YJ, Kong DY, Liu SM, Sun SM, Zhao Z. Investigation on micro-perforated panel absorber

with ultra-micro perforations. Applied Acoustics 2013 74(7):931-935.

[22] Zhao XD, Yu YJ, Wu YJ. Improving low-frequency sound absorption of micro-perforated panel absorbers by using mechanical impedance plate combined with Helmholtz resonators. Applied Acoustics 2016 114:92-98.

[23] Liu Z, Zhan J, Fard M, Davy JL. Acoustic measurement of a 3D printed micro-perforated panel combined with a porous material. Measurement 2017 104:233-236.

[24] Bucciarelli F, Malfense Fierro GP, Meo M. A multilayer microperforated panel prototype for broadband sound absorption at low frequencies. Applied Acoustics 2019 146:134-144.

[25] Jaouen L, Becot FX. Acoustical characterization of perforated facings. The Journal of the Acoustical Society of America 2011 129(3):1400-1406.

[26] Allard J, Atalla N. Propagation of Sound in Porous Media: Modelling Sound Absorbing Materials. 2nd ed. United Kingdom: John Wiley & Sons, 2009.

[27] Peisheng Liu, Guofeng Chen. Porous Materials: Processing and Applications. Oxford Elsevier 2014.

[28] Berardi U, Iannace G. Acoustic characterization of natural fibers for sound absorption applications. Building and Environment 2015 94:840-852.

[29] Yang Y, Chen Z, Chen Z, Fu R, Li Y. Sound insulation properties of sandwich structures on glass fiber felts. Fibers and Polymers 2015 16(7):1568-1577.

[30] Cucharero J, Hänninen T, Lokki T. Angle-dependent absorption of sound on porous materials. Acoustics 2020 2(4):753-765.

[31] Kosten C, Zwikker C. Sound Absorbing Materials. Elsevier New York, 1949.

[32] Delany M, Bazley E. Acoustical properties of fibrous absorbent materials. Applied Acoustics 1970 3(2):105-116.

[33] Miki Y. Acoustical properties of porous materials-Modifications of Delany-Bazley models. Journal of the Acoustical Society of Japan (E) 1990 11(1):19-24.

[34] Johnson DL, Koplik J, Dashen R. Theory of dynamic permeability and tortuosity in fluid-saturated porous media. Journal of Fluid Mechanics 1987 176:379-402.

[35] Champoux Y, Allard JF. Dynamic tortuosity and bulk modulus in air-saturated porous media. Journal of Applied Physics 1991 70(4):1975-1979.

[36] Pride SR, Morgan FD, Gangi AF. Drag forces of porous-medium acoustics. Physical Review B 1993 47(9):4964.

[37] Lafarge D, Lemarinier P, Allard JF, Tarnow V. Dynamic compressibility of air in porous structures at audible frequencies. The Journal of the Acoustical Society of America 1997 102(4):1995-2006.

[38] Xiang Hf, Wang D, Liua Hc, Zhao N, Xu J. Investigation on sound absorption properties of kapok fibers. Chinese Journal of Polymer Science 2013 31(3):521-529.

[39] Atalla N, Panneton R, Sgard FC, Olny X. Acoustic absorption of macro-perforated porous materials. Journal of Sound and Vibration 2001 243(4):659-678.

[40] Olny X, Boutin C. Acoustic wave propagation in double porosity media. The Journal of the Acoustical Society of America 2003 114(1):73-89.

[41] Sgard FC, Olny X, Atalla N, Castel F. On the use of perforations to improve the sound absorption of porous materials. Applied Acoustics 2005 66(6):625-651.

[42] Sánchez-Palencia E. Non-homogeneous Media and Vibration Theory. Berlin, West Germany: Spring-Verlag 1980 127.

[43] Boutin C., Auriault JL. Acoustic absorption of porous surfacing. International Journal of Solids

and Structures 1998 35:4709-4737.

[44] Carbajo J, Molina-Jordá JM, Maiorano LP, Fang NX. Sound absorption of macro-perforated additively manufactured media. Applied Acoustics 2021 182.

[45] Ren SW, Meng H, Xin FX, Lu TJ. Sound absorption enhancement by thin multi-slit hybrid structures. Chinese Physics Letters 2015 32(1):014302.

[46] Ren S, Meng H, Xin F, Lu T. Ultrathin multi-slit metamaterial as excellent sound absorber: Influence of micro-structure. Journal of Applied Physics 2016 119(1):014901.

[47] Feng L. Enhancement of low frequency sound absorption by placing thin plates on surface or between layers of porous materials. The Journal of the Acoustical Society of America 2019 146(2):EL141.

[48] Boutin C. Acoustics of porous media with inner resonators. The Journal of the Acoustical Society of America 2013 134(6):4717.

[49] Park SH. Acoustic properties of micro-perforated panel absorbers backed by Helmholtz resonators for the improvement of low-frequency sound absorption. Journal of Sound and Vibration 2013 332(20):4895-4911.

[50] Groby JP, Lagarrigue C, Brouard B, Dazel O, Tournat V, Nennig B. Enhancing the absorption properties of acoustic porous plates by periodically embedding Helmholtz resonators. The Journal of the Acoustical Society of America 2015 137(1):273-280.

[51] Doutres O, Atalla N, Osman H. Transfer matrix modeling and experimental validation of cellular porous material with resonant inclusions. The Journal of the Acoustical Society of America 2015 137(6):3502-3513.

[52] Lagarrigue C, Groby J-P, Tournat V, Dazel O, Umnova O. Absorption of sound by porous layers with embedded periodic arrays of resonant inclusions. The Journal of the Acoustical Society of America 2013 134(6):4670-4680.

[53] Lagarrigue C, Groby J-P, Dazel O, Tournat V. Design of metaporous supercells by genetic algorithm for absorption optimization on a wide frequency band. Applied Acoustics 2016 102:49-54.

[54] Long H, Cheng Y, Tao J, Liu X. Perfect absorption of low-frequency sound waves by critically coupled subwavelength resonant system. Applied Physics Letters 2017 110(2):023502.

[55] Yang J, Lee JS, Kim YY. Metaporous layer to overcome the thickness constraint for broadband sound absorption. Journal of Applied Physics 2015 117(17):174903.

[56] Yang J, Lee JS, Kim YY. Multiple slow waves in metaporous layers for broadband sound absorption. Journal of Physics D: Applied Physics 2016 50(1):015301.

[57] Kim B-S, Park J. Double resonant porous structure backed by air cavity for low frequency sound absorption improvement. Composite Structures 2018 183:545-549.

[58] Groby J-P, Wirgin A, De Ryck L, Lauriks W, Gilbert R, Xu Y. Acoustic response of a rigid-frame porous medium plate with a periodic set of inclusions. The Journal of the Acoustical Society of America 2009 126(2):685-693.

[59] Gourdon E, Seppi M. On the use of porous inclusions to improve the acoustical response of porous materials: Analytical model and experimental verification. Applied Acoustics 2010 71(4):283-298.

[60] Lee CY, Leamy MJ, Nadler JH. Frequency band structure and absorption predictions for multi-periodic acoustic composites. Journal of Sound and Vibration 2010 329(10):1809-1822.

[61] Groby JP, Dazel O, Duclos A, Boeckx L, Kelders L. Enhancing the absorption coefficient of a backed rigid frame porous layer by embedding circular periodic inclusions. The Journal of the Acoustical Society of America 2011 130(6):3771-3780.

[62] Groby JP, Lagarrigue C, Brouard B, Dazel O, Tournat V, Nennig B. Using simple shape three-dimensional rigid inclusions to enhance porous layer absorption. The Journal of the Acoustical Society of America 2014 136(3):1139-1148.

[63] Chevillotte F, Jaouen L, Bécot FX. On the modeling of visco-thermal dissipations in heterogeneous porous media. The Journal of the Acoustical Society of America 2015 138(6):3922-3929.

[64] Chen S, Jiang Y, Chen J, Wang D. The effects of various additive components on the sound absorption performances of polyurethane foams. Advances in Materials Science and Engineering 2015 2015:1-9.

[65] Lv L, Bi J, Wei C, Wang X, Cui Y, Liu H. Effect of micro-slit plate structure on the sound absorption properties of discarded corn cob husk fiber. Fibers and Polymers 2015 16(7):1562-1567.

[66] Baek SH, Kim JH. Polyurethane composite foams including silicone-acrylic particles for enhanced sound absorption via increased damping and frictions of sound waves. Composites Science and Technology 2020 198.

[67] Xie S, Yang S, Yang C, Wang D. Sound absorption performance of a filled honeycomb composite structure. Applied Acoustics 2020 162.

[68] Núñez G, Venegas R, Zieliński TG, Bécot F-X. Equivalent fluid approach to modeling the acoustical properties of polydisperse heterogeneous porous composites. Physics of Fluids 2021 33(6).

[69] Liu X, Yu C, Xin F. Gradually perforated porous materials backed with Helmholtz resonant cavity for broadband low-frequency sound absorption. Composite Structures 2021 263: 113647.

[70] Tong XC. Functional Metamaterials and Metadevices: Springer, 2018.

[71] Liang Z, Li J. Extreme acoustic metamaterial by coiling up space. Physical Review Letters 2012 108(11):114301.

[72] Xie Y, Popa BI, Zigoneanu L, Cummer SA. Measurement of a broadband negative index with space-coiling acoustic metamaterials. Physical Review Letters 2013 110(17):175501.

[73] Kaina N, Lemoult F, Fink M, Lerosey G. Negative refractive index and acoustic superlens from multiple scattering in single negative metamaterials. Nature 2015 525(7567):77-81.

[74] Cummer SA, Christensen J, Alù A. Controlling sound with acoustic metamaterials. Nature Reviews Materials 2016 1(3):1-13.

[75] Ma G, Yang M, Xiao S, Yang Z, Sheng P. Acoustic metasurface with hybrid resonances. Nature Materials 2014 13(9):873-878.

[76] Li J, Wang W, Xie Y, Popa B-I, Cummer SA. A sound absorbing metasurface with coupled resonators. Applied Physics Letters 2016 109(9): 091908.

[77] Assouar B, Liang B, Wu Y, Li Y, Cheng JC, Jing Y. Acoustic metasurfaces. Nature Reviews Materials 2018 3(12):460-472.

[78] Long H, Liu C, Shao C, Cheng Y, Chen K, Qiu X, et al. Subwavelength broadband sound absorber based on a composite metasurface. Scientific reports 2020 10(1):13823.

[79] Mei J, Ma G, Yang M, Yang Z, Wen W, Sheng P. Dark acoustic metamaterials as super absorbers for low-frequency sound. Nature Communications 2012 3:756.

[80] Yang M, Li Y, Meng C, Fu C, Mei J, Yang Z, et al. Sound absorption by subwavelength membrane structures: A geometric perspective. Comptes Rendus Mécanique 2015 343(12):635-644.

[81] Gao N, Wu JH, Hou H, Yu L. Excellent low-frequency sound absorption of radial membrane acoustic metamaterial. International Journal of Modern Physics B 2017 31(03):1750011.

[82] Ciaburro G, Iannace G. Membrane-type acoustic metamaterial using cork sheets and attached masses based on reused materials. Applied Acoustics 2022 189:108605.

[83] Nguyen H, Wu Q, Chen J, Yu Y, Chen H, Tracy S, et al. A broadband acoustic panel based on double-layer membrane-type metamaterials. Applied Physics Letters 2021 118(18):184101.

[84] Zhao H, Zheng Q, Wang Y, Cao J, Wang C, Wen J. Acoustic absorption of a metamaterial panel: Mechanism, boundary effect and experimental demonstration. Applied Acoustics 2021 184: 108369.

[85] Sui N, Yan X, Huang TY, Xu J, Yuan FG, Jing Y. A lightweight yet sound-proof honeycomb acoustic metamaterial. Applied Physics Letters 2015 106(17):171905.

[86] Tang Y, Ren S, Meng H, Xin F, Huang L, Chen T, et al. Hybrid acoustic metamaterial as super absorber for broadband low-frequency sound. Scientific Reports 2017 7:43340.

[87] Peng X, Ji J, Jing Y. Composite honeycomb metasurface panel for broadband sound absorption. The Journal of the Acoustical Society of America 2018 144(4):EL255.

[88] Kumar S, Lee HP. Labyrinthine acoustic metastructures enabling broadband sound absorption and ventilation. Applied Physics Letters 2020 116(13):134103.

[89] Man X, Xia B, Luo Z, Liu J, Li K, Nie Y. Engineering three-dimensional labyrinthine fractal acoustic metamaterials with low-frequency multi-band sound suppression. The Journal of the Acoustical Society of America 2021 149(1):308-319.

[90] Azbaid El Ouahabi A, Memoli G. A transfer matrix method for calculating the transmission and reflection coefficient of labyrinthine metamaterials. The Journal of the Acoustical Society of America 2022 151(2):1022.

[91] Ding CL, Zhao XP. Multi-band and broadband acoustic metamaterial with resonant structures. Journal of Physics D: Applied Physics 2011 44(21):215402.

[92] Jiang X, Liang B, Li Rq, Zou Xy, Yin Ll, Cheng Jc. Ultra-broadband absorption by acoustic metamaterials. Applied Physics Letters 2014 105(24):243505.

[93] Zigoneanu L, Popa BI, Cummer SA. Three-dimensional broadband omnidirectional acoustic ground cloak. Nature Materials 2014 13(4):352-355.

[94] Jiménez N, Huang W, Romero-García V, Pagneux V, Groby JP. Ultra-thin metamaterial for perfect and quasi-omnidirectional sound absorption. Applied Physics Letters 2016 109(12): 121902.

[95] Laly Z, Panneton R, Atalla N. Characterization and development of periodic acoustic metamaterials using a transfer matrix approach. Applied Acoustics 2022 185:108381.

[96] Laly Z, Mechefske C, Ghinet S, Kone CT, Atalla N. Modelling of acoustic metamaterial sound insulator using a transfer matrix method for aircraft cabin applications. INTER-NOISE and NOISE-CON Congress and Conference Proceedings: Institute of Noise Control Engineering 2023 265(7):366-378.

[97] Wen G, Zhang S, Wang H, Wang Z-P, He J, Chen Z, et al. Origami-based acoustic metamaterial for tunable and broadband sound attenuation. International Journal of Mechanical Sciences 2023 239:107872.

[98] Kushwaha MS, Halevi P. Giant acoustic stop bands in two‐dimensional periodic arrays of liquid cylinders. Applied Physics Letters 1996 69(1):31-33.

[99] Kushwaha MS, Djafari-Rouhani B. Giant sonic stop bands in two-dimensional periodic system of fluids. Journal of Applied Physics 1998 84(9):4677-4683.

[100] M.S. Kushwahaa BD-R, L. Dobrzynski, and J.O. Vasseur. Sonic stop-bands for cubic arrays of rigid inclusions in air. The European Physical Journal B 1998 3:155-161.

[101] Huang GL, Sun CT. Band gaps in a multiresonator acoustic metamaterial. Journal of Vibration

and Acoustics 2010 132(3):031003.

[102] Al Ba'ba'a H, Nouh M, Singh T. Formation of local resonance band gaps in finite acoustic metamaterials: A closed-form transfer function model. Journal of Sound and Vibration 2017 410:429-446.

[103] Zhou X, Wang L, Qin L, Peng F. Improving sound insulation in low frequencies by multiple band-gaps in plate-type acoustic metamaterials. Journal of Physics and Chemistry of Solids 2020 146:109606.

[104] Liu Y, Su Jy, Gao L. The influence of the micro-topology on the phononic band gaps in 2D porous phononic crystals. Physics Letters A 2008 372(45):6784-6789.

[105] Liu Y, Su JY, Xu YL, Zhang XC. The influence of pore shapes on the band structures in phononic crystals with periodic distributed void pores. Ultrasonics 2009 49(2):276-280.

[106] Wang YF, Wang YS, Su X-X. Large bandgaps of two-dimensional phononic crystals with cross-like holes. Journal of Applied Physics 2011 110(11):113520.

[107] Wang K, Liu Y, Yang QS. Tuning of band structures in porous phononic crystals by grading design of cells. Ultrasonics 2015 61:25-32.

[108] Sprik R, Wegdam GH. Acoustic band gaps in composites of solids and viscous liquids. Solid State Communications 1998 106(2):77-81.

[109] Psarobas IE. Viscoelastic response of sonic band-gap materials. Physical Review B 2001 64(1): 012303.

[110] Wang YF, Wang YS, Laude V. Wave propagation in two-dimensional viscoelastic metamaterials. Physical Review B 2015 92(10):104110.

[111] Frazier MJ, Hussein MI. Generalized Bloch's theorem for viscous metamaterials: Dispersion and effective properties based on frequencies and wavenumbers that are simultaneously complex. Comptes Rendus Physique 2016 17(5):565-577.

[112] Li FL, Zhang C, Wang YS. Analysis of the effects of viscosity on the SH-wave band-gaps of 2D viscoelastic phononic crystals by Dirichlet-to-Neumann map method. International Journal of Mechanical Sciences 2021 195:106225.

[113] Hussein MI, Frazier MJ. Band structure of phononic crystals with general damping. Journal of Applied Physics 2010 108(9):093506.

[114] Hussein MI, Frazier MJ. Metadamping: An emergent phenomenon in dissipative metamaterials. Journal of Sound and Vibration 2013 332(20):4767-4774.

[115] Ao X, Chan CT. Complex band structures and effective medium descriptions of periodic acoustic composite systems. Physical Review B 2009 80(23):235118.

[116] Oudich M, Badreddine Assouar M. Complex band structures and evanescent Bloch waves in two-dimensional finite phononic plate. Journal of Applied Physics 2012 112(10):104509.

[117] Laude V, Achaoui Y, Benchabane S, Khelif A. Evanescent Bloch waves and the complex band structure of phononic crystals. Physical Review B 2009 80(9):092301.

[118] Romero-García V, Garcia-Raffi LM, Sánchez-Pérez JV. Evanescent waves and deaf bands in sonic crystals. AIP Advances 2011 1(4):041601.

[119] Wang YF, Liang JW, Chen AL, Wang YS, Laude V. Evanescent waves in two-dimensional fluid-saturated porous metamaterials with a transversely isotropic matrix. Physical Review B 2020 101(18):184301.

[120] Giese F, Ries HC, Eigenbrod C. On the performance of porous sound absorbent material in high temperature applications. Journal of Engineering for Gas Turbines and Power 2010 132(12): 121301.

[121] Christie DRA. Measurement of the acoustic properties of a sound absorbing material at high temperatures. Journal of Sound and Vibration 1976 46(3): 347-355.

[122] Sun F, Chen H, Wu J, Feng K. Sound absorbing characteristics of fibrous metal materials at high temperatures. Applied Acoustics 2010 71(3):221-235.

[123] Williams PT, Kirby R, Malecki C, Hill J. Measurement of the bulk acoustic properties of fibrous materials at high temperatures. Applied Acoustics 2014 77:29-36.

[124] Ren S, Xin F, Lu TJ, Zhang C. A semi-analytical model for the influence of temperature on sound propagation in sintered metal fiber materials. Materials & Design 2017 134:513-522.

[125] Liu X, Xin F, Zhang C. High-temperature effect on the sound absorption of cylindrically perforated porous materials. Journal of Applied Physics 2021 130(10):105101.

[126] Xie Y, Wang L, Peng Y, Ma D, Zhu L, Zhang G, et al. High temperature and high strength Y2Zr2O7 flexible fibrous membrane for efficient heat insulation and acoustic absorption. Chemical Engineering Journal 2021 416:128994.

[127] Zhang W, Liu X, Xin F. Normal incidence sound absorption of an acoustic labyrinthine metal-fibers-based porous metamaterial at high temperature. International Journal of Mechanical Sciences 2023 237:107821.

[128] Zhang W, Liu X, Xin F. Sound absorption performance of helically perforated porous metamaterials at high temperature. Materials & Design 2023 225:111437.

[129] Stinson MR, Champoux Y. Propagation of sound and the assignment of shape factors in model porous materials having simple pore geometries. The Journal of the Acoustical Society of America 1992 91(2):685-695.

[130] Johnson DL, Plona TJ, Scala C, Pasierb F, Kojima H. Tortuosity and acoustic slow waves. Physical Review Letters 1982 49(25):1840-1844.

[131] Leonard RW. Simplified porosity measurements. The Journal of the Acoustical Society of America 1948 20(1):39-41.

[132] Champoux Y, Stinson MR, Daigle GA. Air-based system for the measurement of porosity. The Journal of the Acoustical Society of America 1991 89(2):910-916.

[133] International Organization for Standardization Acoustics - Materials for Acoustical Applications - Part 1: Static Airflow Method, 2018,

[134] Stinson MR, Daigle GA. Electronic system for the measurement of flow resistance. The Journal of the Acoustical Society of America 1988 83(6):2422-2428.

[135] Tang X, Yan X. Airflow resistance of acoustical fibrous materials: Measurements, calculations and applications. Journal of Industrial Textiles 2018 49(8):981-1010.

[136] Leclaire P, Kelders L, Lauriks W, Melon M, Brown N, Castagnède B. Determination of the viscous and thermal characteristic lengths of plastic foams by ultrasonic measurements in helium and air. Journal of Applied Physics 1996 80(4):2009-2012.

[137] Panneton R, Olny X. Acoustical determination of the parameters governing viscous dissipation in porous media. The Journal of the Acoustical Society of America 2006 119(4):2027-2040.

[138] Ren S, Ao Q, Meng H, Xin F, Huang L, Zhang C, et al. A semi-analytical model for sound propagation in sintered fiber metals. Composites Part B: Engineering 2017 126:17-26.

[139] Tarnow V. Airflow resistivity of models of fibrous acoustic materials. The Journal of the Acoustical Society of America 1996 100(6):3706-3713.

[140] Adler EL. Matrix methods applied to acoustic waves in multilayers. IEEE Transactions on Ultrasonics, Ferroelectrics, and Frequency Control 1990 37(6):485-490.

[141] Verdiere K, Panneton R, Elkoun S, Dupont T, Leclaire P. Transfer matrix method applied to the

parallel assembly of sound absorbing materials. The Journal of the Acoustical Society of America 2013 134(6):4648.

[142] Song BH, Bolton JS. A transfer-matrix approach for estimating the characteristic impedance and wave numbers of limp and rigid porous materials. The Journal of the Acoustical Society of America 2000 107(3):1131-1152.

[143] Zhenguo Zhang, Xiaowen Geng. Inversion study of structural parameters of one-dimensional two-component phononic crystal using transfer matrix method. Noise and Vibration Control 2017 37(4):185-187.

[144] Sacristan CJ, Dupont T, Sicot O, Leclaire P, Verdiere K, Panneton R, et al. A mixture approach to the acoustic properties of a macroscopically inhomogeneous porous aluminum in the equivalent fluid approximation. The Journal of the Acoustical Society of America 2016 140(4):2847.

[145] Laude V, Escalante JM, Martínez A. Effect of loss on the dispersion relation of photonic and phononic crystals. Physical Review B 2013 88(22):224302.

[146] Meade RDV, Johnson SG, Winn JN. Photonic Crystals: Molding the Flow of Light. Princeton University Press 2008.

[147] Wang Y. Band gap characteristics and design of phononic crystals containing resonance units. Beijing Jiaotong University Doctoral Dissertation, 2015.

[148] Felsen LB. Evanescent waves. Journal of the Optical Society of America 1976 66(8):751-760.

[149] Zhou XZ, Wang YS, Zhang C. Effects of material parameters on elastic band gaps of two-dimensional solid phononic crystals. Journal of Applied Physics 2009 106(1):014903.

[150] Xin F, Ma X, Liu X, Zhang C. A multiscale theoretical approach for the sound absorption of slit-perforated double porosity materials. Composite Structures 2019 223:110919..

[151] Liu Q, Zhang C. Broadband and low-frequency sound absorption by a slit-perforated multi-layered porous metamaterial. Engineering Structures 2023 281:115743.

[152] Liu Q, Zhang C. Broadband sound absorption by a novel porous metamaterial structure. Proceedings of the International Congress on Sound and Vibration. Singapore 2022.

[153] Jia X, Yan M, Hong M. Sound energy enhancement via impedance-matched anisotropic metamaterial. Materials & Design 2021 197:109254.

[154] Liu Q, Liu X, Zhang C, Xin F. A novel multiscale porous composite structure for sound absorption enhancement. Composite Structures 2021 276:114456.

[155] Liu Q, Liu X, Zhang C, Xin F. High-temperature and low-frequency acoustic energy absorption by a novel porous metamaterial structure. Acta Mechanica Solida Sinica 2021 34:872-883.